FUNCTIONAL THIN FILMS BY SPATIAL ATOMIC LAYER

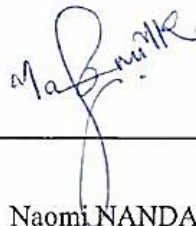# DEPOSITION FOR PHOTOVOLTAIC APPLICATIONS

NAOMI NANDAKUMAR

(M.Sc. Applied Physics, National University of Singapore, Singapore)

THESIS SUBMITTED FOR THE DEGREE OF

DOCTOR OF PHILOSOPHY

DEPARTMENT OF ELECTRICAL AND COMPUTER
ENGINEERING

NATIONAL UNIVERSITY OF SINGAPORE

2017

DECLARATION

I hereby declare that this is my original work and it has been written by me in its entirety. I have duly acknowledged all the sources of information which have been used in this thesis.

This thesis has also not been submitted for any degree in any university previously.

Naomi NANDAKUMAR

20th January 2017

To my parents – Nandakumar and Jasmine

"True delight is in the finding out rather than in the knowing."

Isaac Asimov

ACKNOWLEDGEMENTS

TABLE OF CONTENTS

ABSTRACT

This thesis focuses on the development and analysis of functional thin films deposited by spatial atomic layer deposition (spatial ALD) for application in the photovoltaic (PV) industry. Two key aims of the scientific PV community are the pursuit of higher solar cell conversion efficiencies and the reduction in solar cell manufacturing costs in order to boost the large-scale implementation of renewable solar energy. This work explores the application of functional thin films fabricated with low-cost technology in high-efficiency silicon wafer solar cells.

One of the most important functions of thin films in crystalline silicon (c-Si) solar cells is the passivation of the front and rear silicon surfaces. The exceptional surface passivation properties of aluminium oxide (Al_2O_3) films on p-type c-Si surfaces were only recently recognized by the PV community in 2006, and this material has since been established as an important dielectric in c-Si solar cells, particularly in p-type aluminium local back surface field (Al-LBSF) solar cells.

Thin films also serve as transparent conductive oxides (TCOs) in thin-film solar cells and silicon wafer heterojunction (HET) solar cells. Indium tin oxide (ITO) is presently the predominantly used TCO in the PV community due to its very good electrical and optical properties. However, the scarcity of indium makes it comparatively expensive for PV applications. Zinc oxide (ZnO) is a promising low-cost alternative material for application as a TCO in solar cells.

Common thin film deposition techniques in the PV industry include plasma-enhanced chemical vapour deposition (PECVD), thermal oxidation, and magnetron sputtering. On the other hand, ALD is very well suited to achieve conformal and uniform monolayer-by-monolayer film growth at low temperatures and with precise thickness

control. Furthermore, the absence of a harsh plasma and high-energy species in ALD prevents any surface damage to the substrate. Until recently, however, the widespread adoption of a conventional *temporal* ALD in PV manufacturing was limited by its low throughput. The development of the *spatial* ALD technique overcomes this limitation by separating the ALD precursors in space rather than in time, achieving a much higher throughput (100 – 600 wafers per hour per reactor, SoLayTec ALD) while retaining all the advantages of temporal ALD.

In this thesis, spatial ALD is used to synthesise and develop Al_2O_3 and ZnO thin films. In the first part, a low-cost 'solar-grade' precursor is evaluated for the growth of Al_2O_3 films and the surface passivation properties of these films are compared to films grown using the established and more expensive 'semiconductor-grade' precursor. It is shown via detailed investigations that the solar-grade Al_2O_3 films perform as well as the semiconductor-grade Al_2O_3 films. In the second part, undoped and doped ZnO films grown by spatial ALD are developed and optimised, followed by a detailed study of their electrical, optical and material characteristics. It is observed that the undoped ZnO films demonstrate unusually high electrical resistivity, which is attributed to the especially short precursor exposure and purge durations of spatial ALD. On the other hand, optimised Ga-doped ZnO (GZO) films demonstrate resistivities as low as 2×10^{-3} Ωcm^2 with high optical transparency of > 90 % for visible wavelengths, paving the way for their application as TCOs in solar cells.

The Al_2O_3 films synthesised by spatial ALD using low-cost precursors are then used as the passivating dielectric in *p*-type Al-LBSF solar cells, giving solar cell efficiencies of up to 20.1 % and in *n*-type bifacial solar cells with efficiencies of up to 19.8%. Similarly, the GZO films developed in this work are tested as TCOs in HET solar cells and it is shown that the GZO films are a promising low-cost alternative for the rear TCO of HET cells, as proven by solar cell efficiencies of up to 18.9%.

LIST OF FIGURES

LIST OF TABLES

LIST OF SYMBOLS

Symbol	Description	Unit
α	absorption co-efficient	cm^{-1}
B	material constant for radiative recombination	$cm^3\,s^{-1}$
C	calibration constant of luminescence imaging	-
C_n	Auger co-efficient for electrons	$cm^6\,s^{-1}$
C_p	Auger co-efficient for holes	$cm^6\,s^{-1}$
d_1	film thickness	nm
d_{avg}	average film thickness	nm
d_{max}	maximum film thickness	nm
d_{min}	minimum film thickness	nm
D_{it}	density of interface trap states	$eV^{-1}\,cm^{-2}$
$D_{it.midgap}$	density of interface trap states in the middle of the bandgap	$eV^{-1}\,cm^{-2}$
Δn	excess electron concentration / electron injection level	cm^{-3}
Δp	excess hole concentration / hole injection level	cm^{-3}
ΔV_{avg}	difference in average open-circuit voltage	mV
ΔJ_{avg}	difference in average short-circuit current density	$mA\,cm^{-2}$
η	energy conversion efficiency	%
E_c	energy level of conduction band edge	eV
E_t	energy level of defect traps	eV
E_v	energy level of valence band edge	eV
FF	fill factor	%
iV_{oc}	implied open-circuit voltage	mV
I	current	A
I_{01}	diode dark saturation current	mA
I_L	light-generated current	A
I_{mpp}	maximum-power-point current	A
I_{sc}	short-circuit current	mA
J_{0e}	emitter saturation current density	$fA\,cm^{-2}$
$J_{01,}J_{02}$	saturation current densities in the two-diode model	$fA\,cm^{-2}$
J_L	light-induced current density	$mA\,cm^{-2}$

J_{ph}	photo-generated current density	mA cm^{-2}
J_{sc}	short-circuit current density	mA cm^{-2}
k	extinction coefficient	-
k_B	Boltzmann's constant	m^2 kg s^{-2} K^{-1}
χ_s	semiconductor electron affinity	eV
λ	Wavelength	nm
μ_c	carrier mobility	cm^2 V^{-1} s^{-1}
μ_n	electron mobility	cm^2 V^{-1} s^{-1}
μ_p	hole mobility	cm^2 V^{-1} s^{-1}
m_c^{*}	effective carrier mass	g
v_{th}	thermal velocity	cm s^{-1}
n	density of free electrons	cm^{-3}
n_i	intrinsic carrier concentration	cm^{-3}
n_s	surface electron density	cm^{-2}
n	refractive index	-
n_0	electron density at thermal equilibrium	cm^{-3}
N_A	acceptor dopant density	cm^{-3}
N_c	free carrier concentration	cm^{-3}
N_{dop}	bulk doping concentration	cm^{-3}
N_t	density of recombination defects	cm^{-3}
N_{st}	density of surface recombination defects	cm^{-2}
p	density of free holes	cm^{-3}
p_0	hole density at thermal equilibrium	cm^{-3}
p_s	surface hole density	cm^{-2}
P_{mpp}	maximum-power-point power	W
ϕ	photon flux of luminescence imaging	-
ϕ_m	metal work function	eV
ϕ_{ms}	metal-semiconductor work function difference	eV
ϕ_s	semiconductor work function	eV
q	elementary electronic charge	-
Q_c	corona charge density	q cm^{-2}
Q_f	fixed charge density	q cm^{-2}
Q_{tot}	total charge density in a dielectric	q cm^{-2}

ρ	resistivity	Ω cm
σ	conductance	S cm^{-1}
σ_L	excess photoconductance	S cm^{-1}
σ_n	electron capture cross-section	cm^2
σ_p	hole capture cross-section	cm^2
R_s	series resistance (area weighted)	Ω cm^2
R_{sh}	shunt resistance (area weighted)	Ω cm^2
R_{sheet}	sheet resistance	$\Omega/\square$
S	surface recombination velocity	cm s^{-1}
S_{eff}	effective surface recombination velocity	cm s^{-1}
$S_{eff,max}$	upper limit of surface recombination velocity	cm s^{-1}
τ	carrier recombination lifetime	s
τ_{Auger}	Auger carrier lifetime	s
τ_{bulk}	bulk carrier lifetime	s
τ_{defect}	defect-dependent carrier lifetime	s
τ_{eff}	effective minority carrier lifetime	s
$\tau_{radiative}$	radiative carrier lifetime	s
τ_{SRH}	SRH carrier lifetime	s
$\tau_{surface}$	surface carrier lifetime	s
U_s	surface recombination rate	cm^{-2} s^{-1}
U_{SRH}	SRH recombination rate	cm^{-3} s^{-1}
V	voltage	V
V_{CPD}	contact potential difference voltage	V
V_D	dielectric voltage	V
V_{mpp}	maximum-power-point voltage	mV
V_{oc}	open-circuit voltage	mV
V_{SB}	surface barrier voltage	V
V_T	thermal voltage	V
W	wafer thickness	cm

LIST OF ABBREVIATIONS

Abbreviation	Description
2D	two-dimensional
3D	three-dimensional
4PP	4 point probe
a-Si	amorphous silicon
a-Si:H	hydrogenated amorphous silicon
a-SiN$_x$:H	hydrogenated amorphous silicon nitride
ALD	atomic layer deposition
Al-BSF	aluminium back surface field
Al-LBSF	aluminium local back surface field
Al$_2$O$_3$	aluminium oxide
AlO$_x$	non-stoichiometric aluminium oxide
AM 1.5G	air mass 1.5 global spectrum
APCVD	atmospheric pressure chemical vapour deposition
ARC	anti-reflection coating
AZO	aluminium-doped zinc oxide
BOS	balance of system
B-M shift	Burstein-Moss shift
BSE	back scattered electron
BSF	back surface field
CdS	cadmium sulphide
CH$_4$	methane
CIGS	copper indium gallium selenide
CMP	chemical mechanical polishing
CO$_2$	carbon dioxide
CPD	contact potential difference
c-Si	crystalline Silicon
C-V	corona-voltage
CVD	chemical vapour deposition
Cz Si	Czochralski-grown silicon
DEZ	diethylzinc

DI	deionised
EL	electroluminescence
EQE	external quantum efficiency
FZ-Si	float-zone silicon
GaO$_x$	gallium oxide
Ga$_2$O$_3$	gallium oxide
GPC	growth per cycle
GZO	gallium-doped zinc oxide
HET	hydrogenated amorphous silicon/crystalline silicon heterojunction cell
H$_2$SO$_4$	sulphuric acid
HF	hydrofluoric acid
In$_2$O$_3$	indium oxide
In$_2$O$_3$:Sn	indium tin oxide
IPA	isopropyl alcohol
IPCC	Intergovernmental Panel on Climate Change
IQE	internal quantum efficiency
ITO	indium tin oxide
I-V	current-voltage
i-ZnO	intrinsic zinc oxide
KOH	potassium hydroxide
LCOE	levelised cost of energy
LR	learning rate
MoOx	molybdenum oxide
mono-Si	monocrystalline silicon
mpp	maximum power point of a solar cell
nFAB	n-type front and back contacted solar cell
NIR	near-infrared wavelength range
PCD	photoconductance decay
PECVD	plasma-enhanced chemical vapour depositions
PERC	passivated emitter and rear cell
PERL	passivated emitter rear locally-doped
PL	photoluminescence
PSG	phosphosilicate glass

PV	photovoltaics
P-V	power-voltage
QE	quantum efficiency
QSSPC	quasi-steady-state photoconductance
RCA	Radio Corporation of America
SDE	saw damage etch
SE	spectroscopic ellipsometry
SEM	scanning electron microscope
SIMS	secondary ion mass spectrometry
SiN_x	silicon nitride
SiO_2	silicon oxide
SR	spectral response
SRH	Shockley-Read-Hall recombination
STC	standard test conditions
TCO	transparent conductive oxide
TMA	trimethylaluminium
TMGa	trimethylgallium
ToF-SIMS	time-of-flight secondary ion mass spectrometry
TOPCon	tunnel-oxide passivated contact
UV	ultra-violet wavelength range
XPS	x-ray photoelectron spectroscopy
XRD	x-ray diffraction
ZnO	zinc oxide

Chapter 1: Introduction

1.1   Motivation

The year 2015 was the hottest year in recorded history [1]. Tackling the issues of climate change and global warming that plague our planet is one of the biggest challenges of humankind. The use of fossil fuels as a conventional energy source is of grave concern due to its effects on the environment via the emission of "greenhouse gases", particularly carbon dioxide (CO_2) and methane (CH_4) [2]. Energy from the sun is absorbed by the earth and radiated back into space. Greenhouse gases trap this energy, warming earth's atmosphere and causing an increase in the average terrestrial temperature as shown in Figure 1.1. The ten warmest years in the 134 years since modern record keeping began in 1880, have all, except 1998, occurred since 2000 [3].
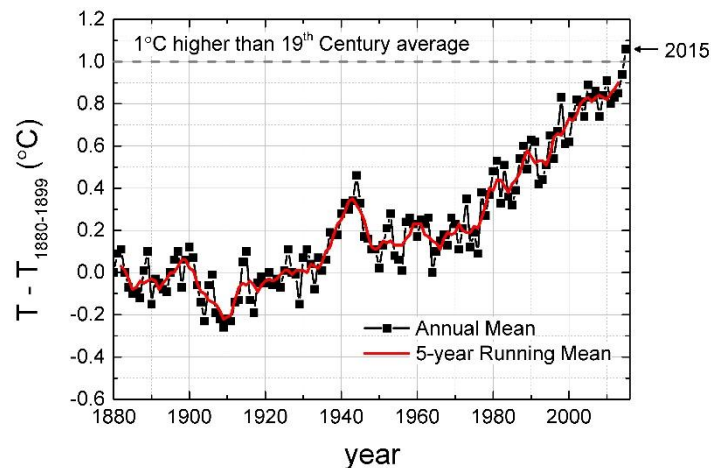
Figure 1.1 Change in global mean temperature (T) relative to 1880-1899 average temperatures ($T_{1880-1899}$). The black dotted line is the annual mean, and the solid red line is the five-year mean. Raw data obtained from [3].

This increase in global temperature correlates with an increase in CO_2 emissions worldwide released due to the burning of fossil fuels [4]. Figure 1.2 shows the atmospheric CO_2 levels in recent years, with the average seasonal cycles excluded. The

trend of CO_2 levels over the last three glacial cycles, as reconstructed from ice cores over a period of 400,000 years before today, shows that the highest historical CO_2 level of 300 ppm was exceeded in 1950 and has been increasing ever since [4]. Global warming, a result of these increasing CO_2 levels, has triggered several other aspects of climate change: shrinking glaciers, a loss of sea ice, an accelerated rise in sea levels (presented in Figure 1.3), intense heat waves, longer droughts in some regions, more frequent wildfires and an increase in the number, duration and intensity of tropical storms.
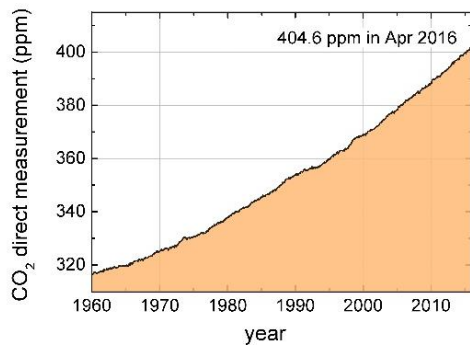
Figure 1.2 Atmospheric CO_2 levels over the period from 1958 to 2016, excluding average seasonal cycles. Raw data obtained from [4].
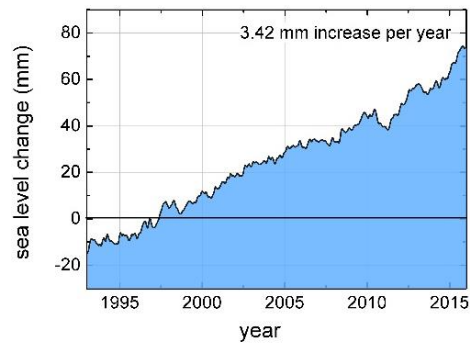
Figure 1.3 Change in sea level since 1993 as recorded by satellite sea level observations. Raw data obtained from [5].

In its 5th Assessment Report, the Intergovernmental Panel on Climate Change (IPCC), an international group of 1,300 independent scientific experts commissioned by the United Nations, concluded that 'human influence on the climate system is clear, and recent anthropogenic emissions of greenhouse gases are the highest in history' [6]. The report highlights that the unprecedented CO_2 emissions arise largely from the burning of fossil fuels. On the other hand, the fact that fossil fuels are limited could lead to a dramatic rise of energy cost, which will have an unforeseeable impact on world poverty and social stability. Hence, there exists an urgent need to find renewable fuel sources which reduce CO_2 emissions and provide sufficient energy at acceptable cost levels.

Nuclear reactors provide low-cost energy with low CO_2 emissions. However, nuclear power plants come with serious risks to humans and the environment, as unfortunately witnessed in recent nuclear disasters such as Chernobyl and Fukushima. In addition, current nuclear technology is based on nuclear fission, which is not renewable and generates large amounts of radioactive waste.
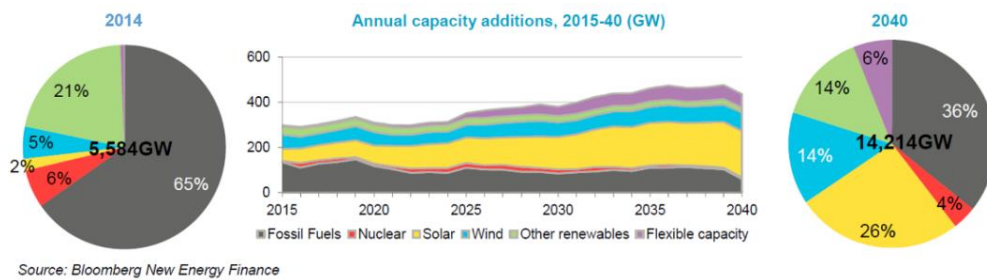
Figure 1.4 Global installed capacity in 2014 and projected capacity additions until 2040 for various renewable energy technologies [7].

The most common renewable energy sources today include wind, solar, hydropower, biofuel, oceanic and geothermal energy. However, the potential use of most renewable energy technologies is limited. Wind and hydroelectric generation are effective only in certain locations. Biomass – organic matter used as fuel – is limited by the availability of water and arable land, while geothermal energy is limited by the high drilling and transport costs. Oceanic energy is a relatively new technology and is probably the least mature renewable energy alternative. On the other hand, solar energy relies on the sun which is a practically inexhaustible energy resource that is abundant and easily available almost all over the globe. Further, it has the highest energy generation potential, with more energy supplied as sunlight to the earth in 90 minutes than mankind uses in a year [8]. It is predicted that by 2040, zero-emission energy sources will make up 60 % of global power capacity with the largest chunk of this being attributed to solar energy [7, 9].

1.2 Photovoltaic (PV) electricity

Photovoltaic (PV) energy conversion is the process of converting sunlight directly into electricity by photon absorption, separation and collection of charge carriers in an electronic material – a process that is almost entirely maintenance-free. Commercial PV modules are durable and easy to transport; an ideal solution for regions with no access to conventional grid-connected electricity. The photovoltaic process produces no pollutants, no waste products and normal use does not liberate toxic chemicals into the environment. Though still a relative newcomer compared to some other electricity generating technologies, it is a rapidly growing and increasingly important renewable energy alternative to conventional electricity generation using fossil fuels [10].

However, the ultimate force that dictates global energy supply is economics. The global cost of PV energy must reach levels comparable to that of fossil fuels, which is not very easy due to the complex fabrication of solar cells and their initial material costs. Hence, one of the goals of applied PV research is cost reduction, with the main focus being a cost per kWh that is on par with that of fossil fuels today. Political incentives and policies such as feed-in tariffs or investment subsidies provided by governments have gradually helped scale up the installed PV capacity. However, these policies are subject to frequent change and serve primarily for kick starting the usage of PV. The levelised cost of energy (LCOE) generated via PV conversion is its total life cycle cost (including equipment, capital, operation and maintenance costs) divided by the total lifetime energy production. Grid parity occurs when the LCOE of PV energy is equal to the price of power purchased from the electricity grid. For example, Singapore achieved grid parity in 2012 for large PV systems [11]. In March 2016, the LCOE for a 1 MW_p[1] rooftop PV installation in Singapore was 0.14 SGD/kWh [12] and

---

[1] W_p stands for peak watt. This is the power output of a solar cell under standard test conditions (i.e. sunlight intensity of 100 mW/cm^2 and cell temperature of 25ºC).

the cost of household electricity obtained from the grid was 0.18 SGD/kWh [13]. Since PV systems do not use any fuel and are largely maintenance-free, a large part of the LCOE is due to the price of the PV panels in a system. Figure 1.5 shows the average module sales price (in US$/$W_p$ as of 2015) as a function of cumulative module shipments from 1976 to December 2015 (in MW_p) [14]. The PV learning rate (LR) which represents the rate of change in average cost (in US$) of a resource with increasing output is also shown. The drop in average sales price is nearly linear, with a LR of about 21.5% for every doubling of cumulative module shipments. This trend follows closely the prediction by Richard Swanson, popularly known as 'Swanson's Law', which states that the price of solar photovoltaic modules will drop 20% each time the shipped volumes double [15]. The major deviations around 2004-2008 and 2012-2014 are attributed to a shortage of silicon feedstock and module overcapacity, respectively [14]. At present rates, module prices halve about every 10 years falling from US$ 76.7/W_p in 1977 to US$ 0.58/W_p in 2015. This rate of reduction is the highest among all the renewable energy technologies. For comparison, the learning rate is 1.4% for hydro-electric power, 11% for biomass power, and 12% for wind power [16].
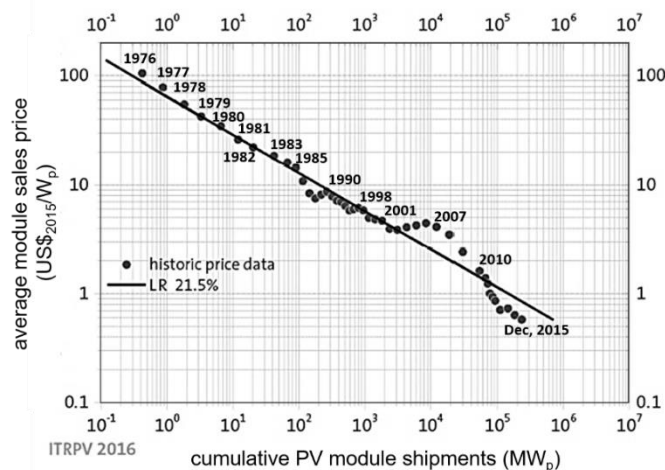
Figure 1.5 Average PV module sales price as a function of cumulative PV module shipments from 1976 to December 2015. The linear PV learning rate (LR) fits the data well until 2003, deviating significantly around 2003-2015 due to tremendous market fluctuations [14].

1.3   Importance of thin films in PV

The primary focus for the long-term development of PV continues to be the cost reduction of electricity generated by PV. The main ways for achieving a cost reduction in cell fabrication are to increase the solar cell's efficiency, for example with superior yet more cost-effective manufacturing processes, and to reduce material and production costs.

A PV system consists of PV modules along with several additional components, commonly referred to as the balance of system (BOS). This includes the wiring, switches, inverters, a fuse-box, an isolator etc. A PV module in turn comprises a number of solar cells which are interconnected. The costs associated with BOS are dominating the total system costs and depend largely on the installation area. In PV conversion, solar cells absorb incident photons with energy larger than their electronic bandgap, resulting in the generation of electron-hole pairs which are then separated by a *p-n* junction and collected by conducting terminals to deliver electric power to the load. The most common type of solar cell is the semiconducting crystalline silicon (c-Si) solar cell. The bandgap of c-Si is well suited for PV application since it enables the absorption of most photons of the solar spectrum (the cut-off wavelength is about 1130 nm at 300 K). Furthermore, c-Si is a relatively inexpensive material due to the abundance of SiO_2 (or sand) on earth's surface and is already a well-established standard in the semiconductor industry. Consequently, it is the dominant material used in PV technologies.

One of the key factors for achieving higher conversion efficiencies in c-Si solar cells is the passivation of the front and rear silicon surfaces [17]. The surface recombination losses significantly reduce the voltage of c-Si solar cells and hence mitigating these losses is vital. Thin films of aluminium oxide (Al_2O_3) possess some remarkable properties that make it well-suited for passivating silicon surfaces in photovoltaic

devices. In particular, the use of atomic layer deposited Al_2O_3 films for the rear passivation of homojunction *p*-type c-Si solar cells has resulted in spectacular improvements in cell efficiencies [14, 18]. On the other hand, an important component of heterojunction (HET) c-Si solar cell structures are thin films of transparent conductive oxides (TCOs) e.g. zinc oxide (ZnO). The TCOs serve to improve lateral transport of the charge carriers in the HET solar cell [19, 20]. As a result, the electrical properties of the TCOs dictate the resistive losses in the solar cell and hence, the solar cell efficiency. In addition to being conductive, the TCO must also be optically transparent to allow sufficient light to pass through to the c-Si underneath. This is critical to the generation of a high photocurrent in the solar cell. The challenge lies in achieving the antagonistic properties of high conductivity and high transparency in TCO materials, in order to boost conversion efficiencies.

This thesis investigates a surface passivating thin film i.e. Al_2O_3 and a transparent conductive oxide i.e. ZnO for application in c-Si solar cell technologies. These films can have a significant impact on both cell efficiencies and manufacturing costs. In particular, this research focuses on the recently developed industrial-scale spatial atomic layer deposition (spatial ALD) technique, a cost-effective and high-throughput deposition technology, for the fabrication and application of these films in homojunction and heterojunction solar cells fabricated from c-Si wafers.

1.4   Thesis outline

This thesis comprises nine chapters.

Chapter 2 introduces the basic operation of c-Si solar cells and highlights the primary loss mechanisms that impact cell performance, i.e. optical losses, electrical losses and resistive losses. The importance of functional thin films in combating these losses is

discussed and a brief description of popular thin-film materials currently used in PV is provided. The common deposition techniques used to synthesise thin films in PV are briefly reviewed and the spatial ALD technique is introduced as the focus of this thesis. Finally, the application of this technique for the deposition of thin films in PV, as reported in the literature, is reviewed.

In **Chapter 3,** the surface passivation properties of aluminium oxide (Al_2O_3) films synthesised using a low-cost 'solar-grade' precursor are evaluated in detail and compared to the conventional more expensive 'semiconductor grade' precursor. This study aims at further reducing the cost of production of spatial atomic layer deposited Al_2O_3 films for its wider adoption in the PV industry.

Chapter 4 explores the fabrication of undoped ZnO films by spatial ALD. The electrical, optical and structural properties of these films are investigated and an explanation for the observation of unusually high resistivity is provided. **Chapter 5** discusses the development and optimisation of gallium-doped ZnO films deposited by spatial ALD for application as a transparent conductive oxide. The influence of the Ga dopant on the growth of the ZnO films is studied and the changes in electrical, optical and material properties of the Ga-doped ZnO (ZnO:Ga) films for varying dopant concentrations are presented. Low resistivity and high transmittance are obtained, making ZnO:Ga a good candidate for potential application as a transparent conductive oxide.

The application of Al_2O_3 films deposited by spatial ALD in homojunction *p*-type aluminium local back surface field (Al-LBSF) solar cells and in *n*-type bifacial front and back contact (nFAB) solar cells are explored in **Chapter 6** and **Chapter 7**, respectively**.** The application of ZnO:Ga as a transparent conductive oxide in heterojunction silicon wafer (HET) solar cells is presented in **Chapter 8.** A loss analysis of these cells is provided and the influence of the spatial ALD thin-films on

the solar cell conversion efficiencies is highlighted. Finally, **Chapter 9** concludes this thesis, summarises the author's original contributions, and proposes future work motivated by this research.

Chapter 2: Background information

2.1 Basic operation of c-Si solar cells

A solar cell or a photovoltaic cell is an optoelectronic device that produces a current and voltage when exposed to light. The operation of a solar cell requires three basic steps: the absorption of photons for the generation of electric charge carriers, the separation of charge carriers of opposite polarity, and the separate extraction of these carriers into an external circuit. As briefly mentioned in Chapter 1, c-Si is an abundant semiconductor with an almost ideal bandgap for the solar spectrum, is the most commonly used material for fabricating solar cells. In c-Si solar cells, incident photons (with energy greater than the c-Si bandgap) can generate electron-hole pairs by the excitation of electrons from their atomic orbitals to higher energy levels. In most cases the c-Si is doped (typically with boron and phosphorus) to form a *p-n* junction, which separates the photogenerated electron-hole pairs so they can be collected at seperate contacts as illustrated in Figure 2.1.
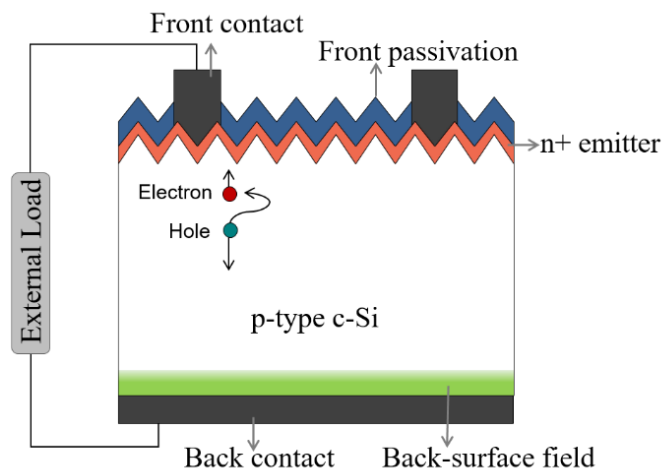
Figure 2.1 A schematic of a standard aluminium back-surface field (Al-BSF) silicon wafer solar cell.

This transport of photogenerated electron-hole pairs generates a current and/or voltage across the solar cell, which can then be dissipated as power in an external load. However, the electron-hole pairs are meta-stable and will only exist for a finite length of time before they recombine. This duration is known as the charge carrier lifetime. On recombination, the light-generated electron-hole pair is lost and no current or power is generated. The selective transport of electrons and holes to the two terminals (positive and negative) of a solar cell is often attributed to the electric field of the *p-n* junction. The light-generated charge carriers (typically the minority charge) diffuse towards the *p-n* junction and are thought to be selectively driven across the junction by the electric field of the space charge region (after which they become the majority charge). However, Würfel *et al.* recently showed that selectivity (in any solar cell structure) is instead achieved by differences in the carrier conductivities of the electrons and holes in two distinct regions of the device, which effects charge carrier separation regardless of the existence of an electric field [21]. In the case of a *p*-type (*n*-type) c-Si base with a diffused n^+-type (p^+-type) emitter, electrons (holes) are collected at the front side while holes (electrons) are selectively transported to be collected at the rear side.

The conversion efficiency of a solar cell quantifies the fraction of solar energy that is converted into electrical energy. The maximum possible conversion efficiency of a single-junction solar cell for a given illumination spectrum is determined by the upper limit of its minority carrier lifetime (influenced by radiative recombination) and is known as the Shockley-Queisser limit [22]. When a solar cell's efficiency is less than this fundamental limit – as is generally the case – it is necessary to identify the detrimental mechanisms responsible and how their influence can be alleviated in a commercially feasible way. The solar cell efficiency is obtained from current-voltage (*I-V)* measurements, that is by the measurement and analysis of the solar cell's *I-V*

curve under standard test conditions (STC)[2] as represented in Figure 2.2 along with the corresponding power-voltage (*P-V*) curve of the cell. In the absence of any illumination, a solar cell has the rectifying *I-V* characteristics of a single diode. When the solar cell is illuminated, its *I-V* curve is displaced along the negative *Y*-axis, indicating that the photo-generated current flows in the opposite direction to the forward current of the diode. In the PV community, the current axis of the *I-V* curve is often inverted, as shown in Figure 2.2.
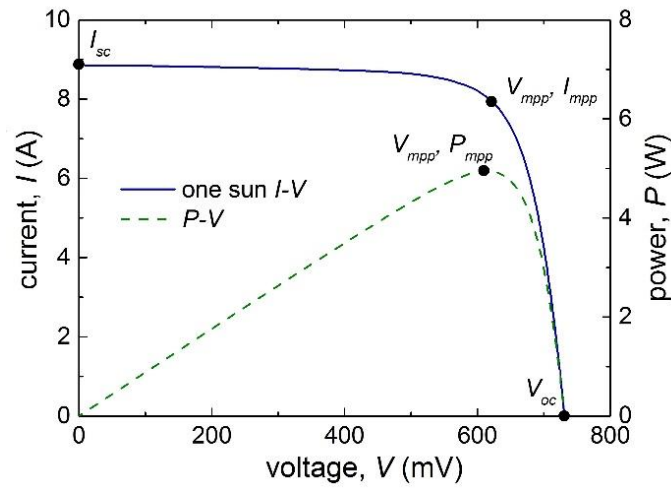
Figure 2.2 I-V and P-V curves of a high-efficiency c-Si solar cell under STC. The cell area is typically about 240 cm².

Figure 2.2 demonstrates that there is a point where *P* is maximum (*P_{mpp}*). The efficiency *η* of the solar cell is defined by the maximum-power-point current *I_{mpp}* and the maximum-power-point voltage *V_{mpp}*:

$$\eta = \frac{P_{mpp}}{P_{in}} = \frac{I_{mpp}V_{mpp}}{P_{in}} \tag{2.1}$$

where *P_{in}* is the incident solar power. By convention, "maximum" is implied, and *η* is simply called the "efficiency" of a solar cell. Under STC, considering an illumination

---

[2] An intensity of 1000 W/m² (or 1 Sun), a AM1.5G spectrum, and a cell temperature of 25 ℃.

of one-Sun i.e. 1000 W/m^2 for an Air Mass 1.5 Global spectrum (AM 1.5G) at a cell temperature of 25ºC, η is defined as

$$\eta = \frac{I_{mpp}V_{mpp}}{1000 \; Wm^{-2} \times cell \; area \; (m^2)} \tag{2.2}$$

The efficiency is the primary parameter of a solar cell, since it quantifies the maximum electrical energy that can be generated under a given illumination. It is helpful, however, to describe the I-V curve in more detail by using three other parameters: the open-circuit voltage (V_{oc}), the short-circuit current (I_{sc}), and the fill factor (*FF*). The V_{oc} is the *x*-axis intercept of the *I-V* curve and this is the voltage of the solar cell under open-circuit conditions. I_{sc} is the *y*-axis intercept of the *I-V* curve and is the current that flows when the solar cell is short-circuited. *FF* is a positive number < 1 that describes the "squareness" of the *I-V* curve, and is defined as:

$$FF = \frac{I_{mpp}V_{mpp}}{I_{sc}V_{oc}} \tag{2.3}$$

The efficiency can be related to I_{sc}, V_{oc} and *FF*, by combining Equations 2.2 and 2.3:

$$\eta = \frac{I_{sc}V_{oc}FF}{1000 \; Wm^{-2} \times cell \; area \; (m^2)} \tag{2.4}$$

Further, it is common to normalise the current to the area of the solar cell and the short-circuit current density J_{sc} ($=I_{sc}/area$) is used to compare differently sized solar cells. For the same reason, J_{sc} will be considered throughout this thesis whenever experimental solar cell results are discussed.

In addition to quantifying the limits of a solar cell, the magnitudes of V_{oc}, J_{sc} and *FF* also related directly to the internal mechanisms of the solar cell. The dependence of these factors on the primary phenomena of carrier generation, carrier recombination and carrier collection, are detailed in the following section.

2.2 Primary loss mechanisms in c-Si solar cells

To maximise the conversion efficiency of c-Si solar cells, the maximum absorption of incident light is required to generate as many electron-hole pairs as possible within the c-Si bulk. These carriers must then be effectively separated and collected at the external electrodes of the solar cell. Carrier generation is mostly concerned with the 'optical quality' of the solar cell, while recombination and collection are concerned with its electrical quality. In c-Si solar cells, functional thin films play an important role in increasing the absorption of light for carrier generation (e.g. SiN_x), minimizing carrier recombination by the passivation of front and rear surfaces (e.g. SiO_2, SiN_x and AlO_x) and inefficient carrier transport when using transparent conductive oxides (e.g. In_2O_3:Sn and ZnO:Al). The physical background of these improvements will be briefly discussed in this section, along with their influence on the electrical solar cell parameters.

2.2.1 Maximising carrier generation through improved optical quality

Due to their direct impact on carrier generation, a poor optical quality primarily affects the power generated from a solar cell by lowering the I_{sc}. Poor optical quality and optical losses are due to light being reflected from the front surface or not being absorbed in the solar cell. Each lost photon could generate a potential electron-hole pair in the solar cell. Photons of wavelength < 1100 nm have sufficient energy to create electron-hole carriers in c-Si (as determined by the c-Si bandgap) and hence c-Si cells have the potential to absorb most photons of the solar spectrum.

The reflectance of the surface of bare silicon in air is $\geq 30\%$ due to c-Si's high refractive index (e.g. ~3.8 at 632 nm). The absorption of light in c-Si solar cells can be maximized by reducing the reflection of incident light on the front side and increasing internal reflection at the rear side for improved light trapping. This is achieved on the front side

by the use of surface texturing techniques that form upright random pyramids as illustrated in Figure 2.3. The texture reduces reflection because photons that are reflected in their first encounter with the solar cell surface are steered *downwards* and therefore have a second chance of entering the solar cell ("double-bounce effect").
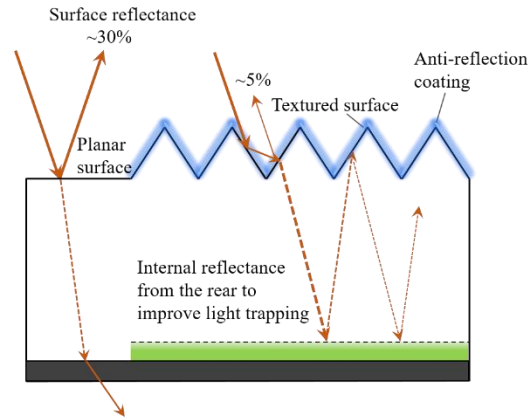
Figure 2.3 Schematic illustration of the optical losses at the front and rear surfaces of a c-Si wafer solar cell. A textured surface with an anti-reflective coating and a rear reflector significantly reduce these losses.

In addition to texturing, an anti-reflection coating (ARC) reduces reflection losses further. Anti-reflection coatings consist of dielectric thin films whereby the layer thickness is chosen to ensure destructive interference of the wave reflected from the top surface of the ARC and the wave reflected from the surface of the c-Si. In this way, light is transmitted into the bulk instead of being reflected. The thickness d_1 of the thin film depends on the refractive index n_1 of the ARC and the wavelength of the incident light in air λ_0. It is calculated by:

$$d_1 = \frac{\lambda_0}{4n_1}.$$
(2.5)

The ideal refractive index for the ARC is the geometric mean of the refractive index of the incident medium n_0 and the refractive index of the c-Si bulk n_2:

$$n_1 = \sqrt{n_0 n_2}.$$
(2.6)

For a c-Si solar cell in air, the optimal ARC refractive index for minimum reflection is 1.9. On the other hand, for a solar cell under glass a refractive index of 2.3 is optimal.[3]

On the rear side, internal reflection can be improved by the application of a thin dielectric film between the c-Si and the rear metal contact. These considerations enable the use of an optimal percentage of incident solar radiation for current generation in solar cells.
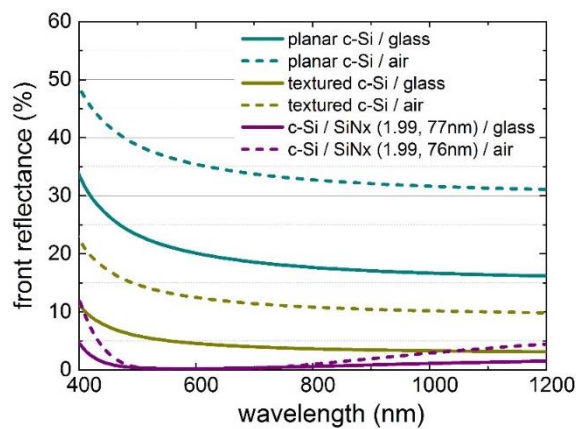
Figure 2.4 Simulated reflectance for a c-Si wafer with a planar surface, a textured surface and a thin film of SiN$_x$ as an anti-reflection coating under glass and in air.

Under illumination, charge carriers are generated in the semiconductor material of a solar cell, giving the light-generated current I_L. Using Shockley's ideal diode equation [23], the current I that flows across the *p-n* junction can be related to I_L and an applied voltage V and thermal voltage V_T by

$$I = I_L - I_{01} \left[\exp\left(\frac{V}{V_T}\right) - 1 \right] \tag{2.7}$$

where I_{01} is the diode's dark saturation current (i.e., the diode current that flows under reverse-bias conditions as a result of electron-hole generation in the bulk and at the

---

[3] The refractive index for glass is considered to be $n_0 = 1.5$ and for simplicity a constant refractive index of $n_2 = 3.5$ is assumed for c-Si though in reality both the refractive indices of c-Si and the ARC are a function of wavelength.

surfaces of the semiconductor). I_{01} depends on temperature, the material properties of the semiconductor layers (doping concentration, carrier diffusivity, carrier diffusion length), and the surface recombination velocities. Three assumptions are made when deriving the ideal diode equation. First, it is assumed that the recombination current arises from Shockley-Read-Hall (SRH) recombination (explained in more detail in the following sections) [24]. Second, it is assumed that the semiconductor is in low injection (i.e., the concentration of minority carriers is much lower than the concentration of majority carriers). Lastly, it is assumed that the current flows in one dimension which is frequently valid for solar cells because they are thin and have a large area with uniformly distributed features. Equation 2.7 can be considered as the *I-V* equation of an ideal solar cell. In low injection, any possible variation from this equation reduces the efficiency of the cell. Combining this equation with the definitions of I_{sc} and V_{oc} given in Section 2.1 yields $I_{sc} = I_L$ and $V_{oc} = V_T\,ln(I_L/I_{01} + 1)$, which shows that, ideally, both I_L and I_{01} can be calculated from measured values of I_{sc} and V_{oc} [25].

2.2.2 Minimising carrier recombination through passivation schemes

The maximum absorption of incident light ensures a high photogeneration of electron-hole pairs in the c-Si. These charge carriers must now be prevented from recombining before they are selectively transported to the front and rear of the solar cell. Recombination leads to a loss of light-generated charge carriers and hence to a reduction of the solar cell efficiency. Recombination losses affect both the short-circuit current J_{sc} as well as the open-circuit voltage V_{oc}. A reduction in recombination losses is enabled by high lifetimes (and thus high diffusion lengths) of the charge carriers.

Simply put, a recombination process is a process in which electron and hole carriers annihilate each other i.e. with the occupation of an empty energy state (or hole) by an electron. This process results in the release of the energy difference between the initial

17

and final state of the electron. Recombination processes are classified in by the way the excess energy is released. The energy can be released as a photon (*radiative recombination*), it can be transferred to another hole or electron (*Auger recombination)*, or it can be released as heat through phonon emission (*non-radiative emission* or *defect-assisted recombination*) as schematically illustrated in Figure 2.5.
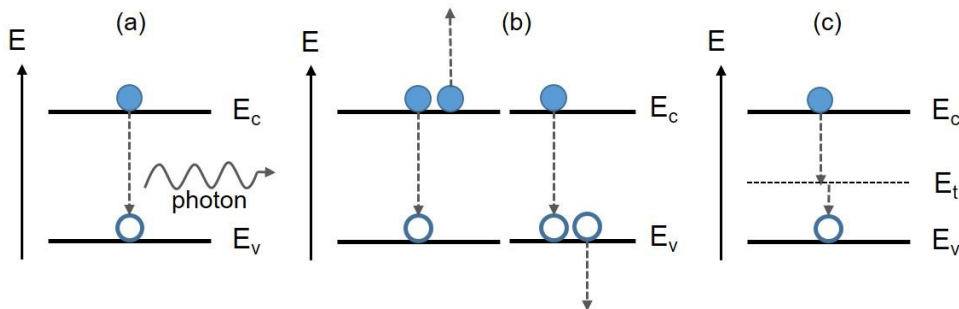
Figure 2.5 Schematic representation of (a) radiative recombination (b) Auger recombination where energy is transferred to an electron or hole and (c) non-radiative recombination via a deep-level defect at a fixed energy E_t.

Each region of a solar cell device is affected by one or more of these recombination processes. When analysing a solar cell, it is easier to characterise the recombination processes based on where they occur in the cell. At the surface of c-Si, a large number of dangling bonds create a high density of defects throughout the silicon bandgap, giving rise to *surface recombination*. Both the front and the rear surface of a silicon wafer solar cell contribute to surface recombination losses. The emitter in a solar cell is a heavily doped region which results in a high density of defects, which gives rise to *emitter recombination*. Finally, recombination in the silicon bulk constitutes *bulk recombination.* A brief description of each of these is presented below.

(i)   Bulk recombination

We consider the case of a homogeneously doped and infinitely thick wafer with a negligible electric field. This implies that the excess concentrations of electrons and holes upon illumination are equal (i.e., every photon generates an equal number of

excess electrons and holes, or $\Delta n = \Delta p$) provided charge carrier trapping is absent. In this case, for *n*-type as well as *p*-type c-Si material, a *carrier recombination lifetime τ* can be defined for each recombination process [26]:

$$\tau \,(\Delta n, n_{0,}p_0) = \frac{\Delta n}{U \,(\Delta n, n_{0,}p_0)} \tag{2.8}$$

where *U* is the *net* recombination rate, $\Delta n \equiv n - n_0$ and $\Delta n \equiv p - p_0$ are the excess carrier concentrations, *n* and *p* the electron and hole concentration, and n_0 and p_0 the thermal equilibrium concentrations of electrons and holes, respectively. The total net recombination rate *U* in c-Si is the sum of radiative, Auger and defect-assisted recombination. Since these recombination processes are independent of each other, the resulting total *bulk* carrier lifetime τ_{bulk} can be evaluated using the individual carrier lifetimes [26]:

$$\frac{1}{\tau_{bulk}} = \frac{1}{\tau_{radiative}} + \frac{1}{\tau_{Auger}} + \frac{1}{\tau_{defect}} \,. \tag{2.9}$$

From this equation, it is seen that the recombination process with the smallest carrier lifetime (and hence highest net recombination rate) influences τ_{bulk} the most.

Each recombination process can be fundamentally distinguished as *intrinsic* (unavoidable) and *extrinsic* (avoidable) recombination. Radiative and Auger recombination processes in the c-Si bulk are intrinsic and are strongly determined by the base doping level and charge carrier density of the bulk material [27, 28]. Radiative recombination constitutes the reverse process of photon absorption and is simply a spontaneous emission process. In this case, an electron in the conduction band loses energy and falls into a vacant valence band state releasing the energy difference between the two states in the form of a photon. The energy of this emitted photon typically corresponds to the energy of the bandgap. In c-Si, radiative recombination

has a relatively low probability due to the indirect nature of the c-Si bandgap. The carrier lifetime for radiative recombination is [26]:

$$\tau_{radiative} = \frac{1}{B\,(n_0 + p_0 + \Delta n)} \qquad (2.10)$$

where B is a material constant and has a value of 1.0×10^{-14} cm^3/s in c-Si at 300 K. The relatively low value of B is due to the indirect bandgap of c-Si and corresponds to a low probability of radiative recombination.

Auger recombination is a three-particle recombination process. It involves an interaction between two similar charge carriers, resulting in the excitation of one carrier to a higher energy level, and the recombination of the other with a carrier of the opposite polarity. As a consequence, the probability of Auger recombination strongly depends on the carrier concentration. This is the reason why Auger recombination is the dominant mechanism in the heavily-doped regions of the solar cell, such as the emitter. The Auger recombination lifetimes are given by

$$\tau_{Auger} = \frac{1}{C_n n^2 + C_p n \Delta n} \quad \text{(for } n\text{-type c-Si)} \qquad (2.11a)$$

$$\tau_{Auger} = \frac{1}{C_p p^2 + C_n p \Delta n} \quad \text{(for } p\text{-type c-Si)} \qquad (2.11b)$$

where C_n and C_p are Auger coefficients and $\Delta n = \Delta p$ is assumed. It can be seen that the Auger lifetime decreases with increasing doping or injection level.

Extrinsic *non-radiative recombination* processes occur via defect states, such as when an electron falls into an energy level within the forbidden bandgap (or a defect state) where it has easier access to a hole in the valence band as displayed in Figure 2.5 (c). The defect states can be formed by the presence of foreign atoms (e.g. metallic impurities) within the Si or by dangling bonds due to dislocations in the crystalline lattice or at grain boundaries (e.g. in multicrystalline Si). This defect-related

recombination process is of paramount importance for indirect bandgap semiconductors such as c-Si. The model for this recombination process was developed by Shockley, Read [24] and Hall [29] in 1952 and the process is thus commonly referred to as *Shockley-Read-Hall* (SRH) recombination. Their model describes the two-step transition of an electron from the conduction band into a defect level at a fixed energy level E_t and from there into the valence band where it recombines with a hole. The excess energy in this transition is released as phonons (i.e., lattice vibrations). The SRH theory predicts the recombination rate U_{SRH} (in cm^{-3}s^{-1}) for a single-level defect located at the fixed energy E_t. This defect may capture carriers with capture cross-sections σ_p and σ_n specific to that defect for holes and electrons, respectively. The U_{SRH} is then calculated as:

$$U_{SRH} = \frac{v_{th}N_t(np-n_i^2)}{\frac{n+n_1}{\sigma_p}+\frac{p+p_1}{\sigma_n}} = \frac{np-n_i^2}{\tau_{n0}(p+p_1)+ \tau_{p0}(n+n_1)} \tag{2.12}$$

where v_{th} is the thermal velocity of the charge carriers (~ 10^7 cm/s in c-Si at 300 K) and N_t is the density of recombination defects (in cm^{-3}). n_1 and p_1 are carrier densities in the conduction and valence band and are given by [26]:

$$n_1 \equiv n_i \exp(\frac{E_t-E_i}{kT}), \qquad p_1 \equiv n_i \exp(\frac{E_C-E_G-E_t}{kT}), \qquad n_1 p_1 = n_i{}^2 \tag{2.13}$$

The capture time constant of electrons and holes τ_{n0} and τ_{p0} are given by

$$\tau_{p0} \equiv \frac{1}{\sigma_p\, v_{th}N_t} \qquad \text{and} \qquad \tau_{n0} \equiv \frac{1}{\sigma_n\, v_{th}N_t} \tag{2.14}$$

The recombination rate is proportional to the thermal velocity, defect concentration and is dependent on the defect energy level. The driving force for SRH recombination is the term $np-n_i^2$, which describes the deviation of the carrier concentrations from their thermal equilibrium values [26]. From Equation 2.12 the injection-level

dependent SRH carrier lifetime can be calculated using $\Delta n = \Delta p$ and the definition $U \equiv \Delta n/\tau_{SRH}$:

$$\tau_{SRH} = \tau_{p0} \frac{n_0+n_1+\Delta n}{n_0+p_0+\Delta n} + \tau_{n0} \frac{p_0+p_1+\Delta n}{n_0+p_0+\Delta n} \tag{2.15}$$
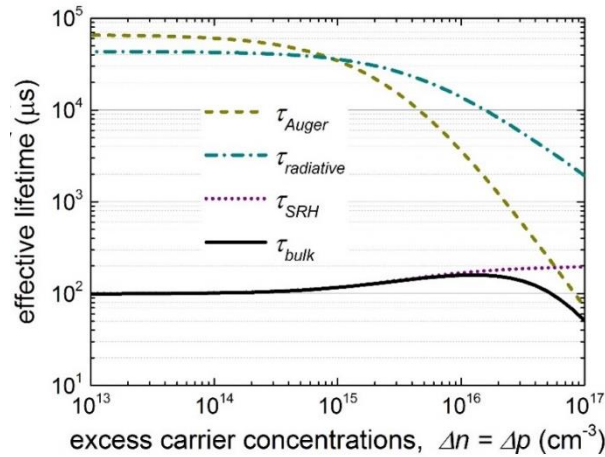
Figure 2.6 Simulated radiative, Auger, SRH and effective bulk carrier lifetime for a 3.0 Ωcm p-type c-Si wafer at 300 K as a function of excess carrier concentration. The SRH behaviour is shown for the case of a deep defect ($E_t = E_i$) and $\tau_{n0} = \tau_{p0} = 1$ ms is assumed.

Figure 2.6 shows the modelled effective radiative, Auger, SRH and bulk carrier lifetimes for a 3.0 Ωcm *p*-type c-Si wafer at 300 K. The radiative carrier lifetime was approximated using the parameterization of Trupke *et alia* [30]. The Auger lifetime was taken from Richter *et al.* [31] and the SRH lifetime from equation 2.15 where $\Delta n = \Delta p$ for the case of a deep-level defect ($E_t = E_i$) and assuming $\tau_{n0} = \tau_{p0} = 1$ ms [26]. It can be seen that the SRH recombination is the lifetime-limiting process for lower carrier injection levels ($< 10^{16}$ cm^{-3}) while Auger recombination dominates for higher carrier injection levels ($> 6 \times 10^{16}$ cm^{-3}). Further, the radiative recombination is seen to have negligible influence, as mentioned earlier.

(ii)   Surface recombination

The symmetry of a semiconductor crystal lattice is interrupted in the most severe way at the surface. The surface represents incomplete or 'dangling' bonds which gives rise

to a high density of defect states within the c-Si bandgap. As a consequence, recombination at a c-Si surface is of paramount importance in silicon wafer solar cells. Further, the exposure of the surface to various environments during the processing of solar cell devices also gives rise to surface contamination and damage which results in metal impurities and dislocations that contribute additional defect states at the surface.

Recombination at a c-Si surface via these defects is also described by the SRH theory. Based on Equation 2.12, the recombination rate U_s (in cm^{-2}s^{-1}) at the surface for a single-level defect state located at an energy E_t within the bandgap is given by [26]:

$$U_s = \frac{v_{th}N_{st}(n_sp_s-n_i^2)}{\frac{n_s+n_1}{\sigma_p}+\frac{p_s+p_1}{\sigma_n}} = \frac{n_sp_s-n_i^2}{\frac{n_s+n_1}{S_{p0}}+\frac{p_s+p_1}{S_{n0}}} \tag{2.16}$$

where $\qquad S_{n0} \equiv \sigma_n v_{th} N_{st} \qquad$ and $\qquad S_{p0} \equiv \sigma_p v_{th} N_{st}$

S_{n0} and S_{p0} are the *surface recombination velocity parameters* (in cm/s) of electrons and holes, n_s and p_s are the electron and hole concentrations at the surface, σ_n and σ_p are the capture cross-sections for electrons and holes, and N_{st} is the number of surface states per unit area. The remainder of the parameters retain their same meaning. In reality, defects are distributed across the Si bandgap and as a result, the surface defect parameters ($\sigma_{n/p}$, $n_{1/2}$ and N_{st}) are not constant. They depend on each defect's energy level within the bandgap. Hence it is more accurate to consider U_s as a function of energy replacing N_{st} with the density of interface trap states D_{it} (E) (in eV^{-1}cm^{-2}) [32, 33]. In general, the defect states near the middle of the bandgap (0.55 eV for c-Si) tend to dominate the total surface recombination rate. Further, as a result of electrical charges at the semiconductor surface, the energy bands of the c-Si are generally bent towards the surface (i.e. the flat-band condition $\Delta n_s = \Delta p_s$ rarely exists). This significantly complicates the calculation of the electron and hole surface concentrations n_s and p_s. In this case it is useful to define an *effective surface recombination velocity (S_{eff})* [26, 34, 35], in analogy to Equation 2.8,

$$S_{eff} = \frac{U_s}{\Delta n_s(x=d)} \tag{2.17}$$

at a virtual surface within the wafer positioned at the edge of the surface space charge region (denoted as x=d) where the excess carrier concentration at this virtual surface is denoted by $\Delta n(x=d)$.

Usually, a direct measurement of S_{eff} is not possible. However, it is easy to measure the so-called *effective minority carrier lifetime* or τ_{eff} which accounts for all recombination mechanisms within the bulk and at both surfaces of the c-Si wafer. This can, for example, be measured with the photoconductance decay (PCD) method which is widely used in the PV community [36-38]. The PCD methods measures τ_{eff} as a function of the excess carrier concentration in a c-Si wafer generated upon illumination. τ_{eff} depends on the c-Si bulk carrier lifetime τ_{bulk} as well as on the carrier lifetimes at the front and rear surface $\tau_{surface}$ (assuming both surfaces have the same recombination velocities) and can be represented as:

$$\frac{1}{\tau_{eff}} = \frac{1}{\tau_{bulk}} + \frac{2}{\tau_{surface}} \tag{2.18}$$

From equation (2.9) we then have

$$\frac{1}{\tau_{eff}} = \left(\frac{1}{\tau_{radiative}} + \frac{1}{\tau_{Auger}} + \frac{1}{\tau_{SRH}}\right)_{bulk} + 2\left(\frac{1}{\tau_{SRH}}\right)_{surface} \tag{2.19}$$

If both surfaces of the c-Si wafer are identical, then the effective surface recombination velocity S_{eff} at each surface is given by

$$S_{eff} = \frac{W}{2}\left(\frac{1}{\tau_{eff}} - \frac{1}{\tau_{bulk}}\right) \tag{2.20}$$

where W (in cm) is the thickness of the wafer. Hence, if the bulk lifetime τ_{bulk} is known, for example by using the method in [39], then the S_{eff} can be determined from the measured value of τ_{eff} using Equation (2.20). In general, the bulk lifetime determined

for a given silicon wafer is within certain error limits, which leads to a certain systematic error in S_{eff}. For this reason, the surface properties are preferentially evaluated on high-quality bulk materials, for example float-zone (FZ) silicon wafers. In this case, the total recombination losses can be assumed to be dominated by the recombination at the wafer surfaces and τ_{bulk} can be assumed to be limited by intrinsic recombination (i.e. $\tau_{bulk} \rightarrow \infty$). This corresponds to the upper limit for the surface recombination velocity, which can be denoted as

$$S_{eff,max} = \frac{W}{2\tau_{eff}} \tag{2.21}$$
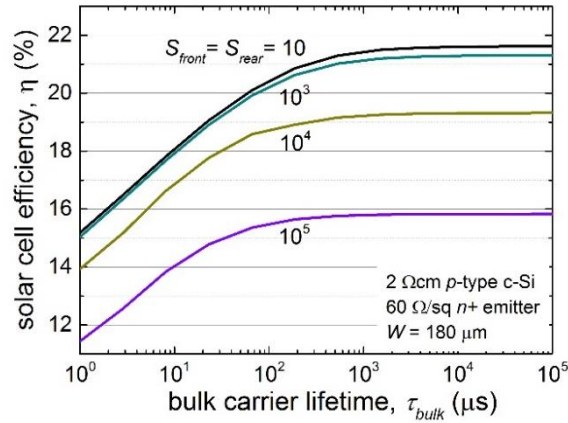
Figure 2.7 Simulated one-Sun efficiency of a p-type c-Si wafer solar cell with a diffused n^+ emitter as a function of the bulk lifetime of the c-Si for various surface recombination velocities ($S_{front} = S_{rear}$). Simulated using PC1D (AM 1.5G, 300 K, 180 μm thick wafer, 2% front reflection, 0.5 μm thick 60 Ω/sq n^+ emitter).

To obtain high (> 20%) silicon wafer solar cell efficiencies, it is vital to reduce recombination in the bulk and at both surfaces of the solar cell as shown in Figure 2.7. For τ_{bulk} < 1000 μs, the poor bulk quality dominates the solar cell performance. However, for higher τ_{bulk} the solar cell conversion efficiencies saturate and are now dominated by the surface recombination. Hence, the c-Si bulk material needs to be of good electronic quality (high τ_{bulk}) and the recombination losses at the front and rear surfaces should be minimised (low S_{eff}). This is achieved by so-called *surface passivation* of both solar cell surfaces. The enormous significance of the surface is

because the diffusion (or drift) lengths of the minority charge carriers in the emitter and base of high-efficiency Si solar cells exceed the thicknesses of these layers exposing the charge carriers to numerous defects states at the surface (surface states).

There are two fundamentally different strategies to reduce surface recombination losses: (i) Reduction of the density of surface states, and (ii) reduction of the concentration of free electrons or holes at the surface. Most high-efficiency solar cells exploit both fundamental principles of surface passivation.

(a)   Chemical passivation – reduction of density of surface states

As described above, the surface recombination is essentially governed by the SRH recombination rate which is proportional to the density of defect states or interface trap states, D_{it} (from $N_{st} = \int D_{it}\,dE$). A reduction in D_{it} can be achieved by the passivation of these defect states typically using a functional thin film grown or deposited on the silicon surface. Some proven candidates for the passivation of c-Si are silicon dioxide (SiO_2), silicon nitride (SiN_x), aluminium oxide (AlO_x) and amorphous silicon (a-Si) [17, 40-42]. For example, the mid-gap D_{it} of undiffused c-Si can be as low as 1×10^9 $eV^{-1}cm^{-2}$ after growing a high-quality thermal SiO_2 film followed by an anneal in a H_2 containing gas environment (e.g. forming gas [43]). Alternatively, polar liquids (e.g. acids such as HF and H_2SO_4) have also yielded very low surface recombination velocities (< 1 cm/s) [44]. In this case, the hydrogen atoms from the acids passivate the dangling bonds at the surface thereby reducing the D_{it}. This type of passivation is known as defect passivation or chemical passivation. However, immersing silicon wafers in polar liquids for long periods of time is not practical, and the H-passivation effect is not stable once the c-Si surface is exposed to air for long durations of time. Hence, the use of functional thin films for the surface passivation of c-Si is of paramount importance. Optimised film deposition conditions and post-deposition annealing treatments can help achieve very low surface recombination velocities. This

thesis will focus on the surface passivation properties of aluminium oxide thin films deposited by spatial ALD on c-Si (Chapters 3, 6 and 7).

(b)   Field-effect passivation – reduction of electrons and hole concentration

Both a hole and an electron are necessary for each recombination process. Hence, the highest recombination rates are obtained for the case when the concentration of electrons and holes are approximately equal. In contrast, if the concentration of either electrons (n_s) or holes (p_s) is significantly lower than the other, then the recombination rate is strongly reduced [26]. Since electrons and holes are charged, such a desired reduction in the surface charge concentration of one type of carrier is most easily realised by heavily doping the semiconductor near the surface. One way this can be achieved is by the formation of a doped profile near the surface. Or alternatively, by field-effect passivation whereby fixed external electrostatic charges on top of the c-Si surface result in an electric field near the surface. Technologically, this is implemented by the deposition of a large variety of functional thin dielectric films that have intrinsic fixed charges near the interface with c-Si. The higher this fixed charge density Q_f (in elementary charges per cm^2) within the overlying dielectric film, the lower is the recombination rate and hence S_{eff} at the c-Si surface. In the PV community, silicon oxides and silicon nitrides are widely used as positively charged dielectrics ($Q_f > 0$) while aluminium oxide is a popular negatively charged dielectric ($Q_f < 0$). In addition to the magnitude, the polarity of the fixed charges has a large impact on the surface passivation of moderately and heavily doped silicon since they determine whether the band bending at the c-Si surface creates accumulation, depletion or inversion conditions. This thesis focuses on the introduction of negative fixed charges by a thin aluminium oxide layer deposited on the c-Si surface which can reach Q_f values up to 10^{13} cm^{-2}. This high value of Q_f reduces S_{eff} by over four orders of magnitude compared to neutral dielectrics.

(iii)   Emitter recombination

The carrier recombination in the emitter of c-Si solar cells is usually characterised by a quantity known as emitter saturation current density J_{0e} which represents the combined effects of Auger, SRH and surface recombination in the highly-doped region. The emitter recombination can be regarded as a simplified case of surface recombination. The emitter is much thinner than the bulk of the c-Si wafer with considerably lower light-generated excess carrier concentrations. In addition, because the carrier lifetime in the heavily doped emitter is much lower than in the bulk of the wafer, the recombination current into the emitter during the excess carrier decay after a light pulse excitation can accurately be described using a 'quasi-static emitter approximation' which takes into account the effect of the carriers in the emitter on the open-circuit voltage decay [45]. Following this approximation and the Kane-Swanson methodology [46], the effective surface recombination velocity for, say, an n^+-diffused emitter on a lowly injected p-type wafer can be given by

$$S_{eff} = \frac{N_A J_{0e}}{q n_i^2}$$

(2.22)

where N_A is the acceptor dopant density and n_i is the intrinsic carrier concentration. As mentioned above, recombination losses affect both J_{sc} and V_{oc} of a solar cell. Localised recombination sites at the front and rear surfaces result in selective absorption of short and long wavelengths, respectively, which affects the collection probability of light at these wavelengths and hence the total current generated. Recombination processes at both the surface of the c-Si bulk and the heavily doped emitter can be significantly reduced using functional thin films that provide chemical and field-effect passivation. These films are commonly referred to as surface passivation layers. Together with providing surface passivation, these thin films also serve as anti-reflective coatings, reducing optical losses. A detailed description of popular surface passivation layers will be provided in Section 2.3.1.

2.2.3 Minimising resistive losses for optimum carrier collection

In addition to maximising the absorption of photons and minimising recombination, the final condition necessary when designing high-efficiency solar cells is to minimise parasitic resistive losses for optimal collection of all photo-generated carriers at the front and rear contacts. The most common parasitic resistances are series resistance (R_s) and shunt resistance (R_{sh}), as illustrated in Figure 2.8.
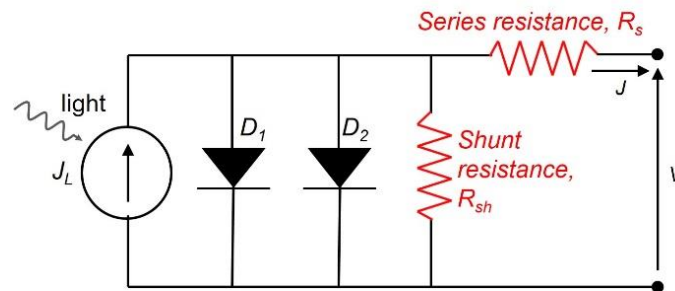
Figure 2.8 Schematic of an equivalent solar cell circuit (two-diode model) demonstrating the parasitic series and shunt resistances of the solar cell.

For typical values of series and shunt resistance, the key impact of the parasitic resistance is that they reduce the fill factor *FF*. Since the value of resistance naturally depends on the area of the solar cell, it is common to normalise the unit for resistance by the cell area in Ωcm^2. This makes it easy to directly compare solar cells of different areas.

The series resistance of a solar cell can be attributed to (a) the movement of current through the emitter and base of the solar cell, (b) the contact resistance between the metal contact and the silicon, and (c) the resistance of front and rear contacts. R_s mainly impacts the solar cell's *FF*, although extremely high values may also reduce the J_{sc}. Series resistance does not affect the solar cell open-circuit voltage (since no current flows through the cell under open-circuit conditions). However, the slope of the *I-V* curve near the *x*-axis intercept is strongly influenced by R_s. Consequently, the slope at the V_{oc} point can be used to determine the R_s value. Alternatively, R_s can also be

determined by comparing the dark *I-V* curve with the one-sun *I-V* curve [47]. Typical R_s values of c-Si solar cells range from 0.5 to 1.5 Ωcm^2.

Power losses caused by the presence of a shunt or parallel resistance R_{sh} provide an alternate current path for the photo-generated current. As a result of this diversion the amount of current flowing through the cell is reduced and so is the V_{oc}. The effect of R_{sh} is particularly severe at lower light intensities, due to the higher impact of a shunt on the lesser amount of light-generated current. A low shunt resistance is typically due to processing and manufacturing defects. Most commonly a low R_{sh} is due to leakage currents along the edges of a solar cell. Sometimes they are also due to spiking of the *p-n* junction by metal contacts. Typical values of R_{sh} are $\geq$10,000 Ωcm^2 for c-Si solar cells.
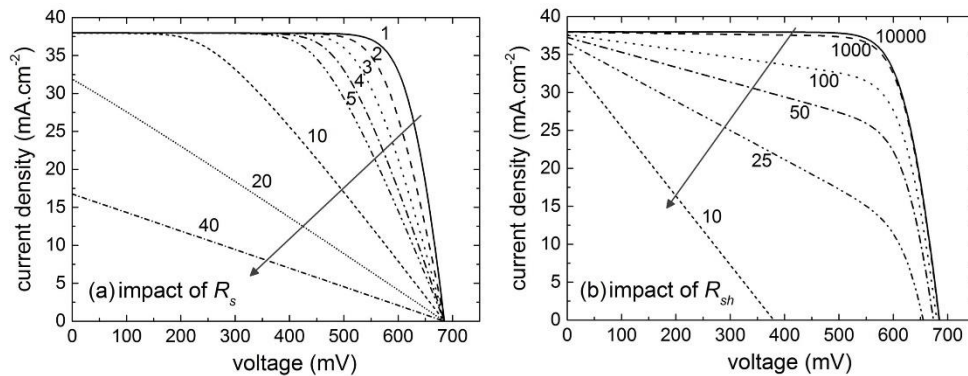
Figure 2.9 The influence of parasitic resistances on the I-V curve of a solar cell for increasing (a) series resistance, R$_s$, and (b) shunt resistance, R$_{sh}$ simulated using the online calculator on PV Lighthouse [48].

The influence of R_s and R_{sh} on a solar cell *I-V* curve is shown in Figure 2.9, simulated using the equivalent circuit calculator from PV Lighthouse [48]. As seen, the *FF* of the solar cell is severely affected by increasing R_s and decreasing R_{sh}. However, V_{oc} and J_{sc} are only affected for extreme values of R_s and R_{sh}. For an efficient solar cell, R_s should be as small as possible, and R_{sh} should be as large as possible [49].

In some c-Si solar cell structures such as the heterojunction silicon wafer (HET) solar cell, thin films of transparent conductive oxides serve as the electron and hole collectors between the silicon and the metal contact grid. [4] These films play an important role in maintaining low R_s and high R_{sh} in the solar cells. This thesis will focus on the functionality of doped ZnO as TCOs in HET solar cells and their influence on reducing parasitic resistive losses.

2.3   Functional thin films in PV

In this section, a brief overview of functional thin films employed in c-Si solar cells will be presented. A variety of thin film materials are used in the design of c-Si solar cells to overcome the optical and electrical losses highlighted in Section 2.2. Two specific applications of thin films are the focus of this thesis: films for surface passivation and transparent conductive oxides. In this section, a review of the most relevant functional thin films in these two categories will be provided to put the films studied in this thesis into a broader perspective.

2.3.1   Films for c-Si surface passivation

In the silicon PV industry, the most popular thin film used to provide surface and bulk passivation of c-Si solar cells is hydrogenated amorphous silicon nitride (a-SiN$_x$:H) since it also simultaneously acts as an anti-reflection coating (ARC). However, building on the knowledge of the semiconductor industry, thermally grown SiO$_2$ is also a state-of-the-art surface passivation layer often used in certain solar cell structures. More recently, Al$_2$O$_3$ films have demonstrated excellent surface passivation properties

---

[4] The front side electrical contacts of most c-Si solar cells generally consist of a grid of fingers and bus-bars printed using an Ag-containing paste. Depending on whether the solar cell is monofacial or bifacial, respectively, the rear side may consist of a full-area back contact or may also consist of a contacting grid.

and have been rapidly integrated into the PV industry over a short period of time. In this section, a few established surface passivation layers will be described. Though as new solar cell designs emerge and the optical and electrical requirements increase, more and more functional thin films (e.g. GaO_x, MoO_x) find use in the field, not just for surface passivation but also as passivating and carrier-selective contacts.

(i)   Silicon dioxide (SiO$_2$)

Silicon dioxide (SiO_2) films have been an integral part of field-effect devices (VLSI circuits, MOS and MOSFETs structures) since the 1970s. As a result, the Si-SiO$_2$ interface has been the most intensively investigated semiconductor-insulator system over the last decades. A thermally grown SiO$_2$ is obtained by the oxidation of c-Si wafers in a quartz tube which is maintained at 800-1200 ℃ and filled with an oxidising gas environment (ultrapure O$_2$ or H$_2$O). The thermally grown Si-SiO$_2$ interface can exhibit extremely low interface defect densities of $\sim 10^9$ eV^{-1}cm^{-2} [32, 43, 50]. The high interface quality is assured by the fact that the thermal SiO$_2$ grows into the wafer by consuming the underlying silicon. Hence the final interface is almost unaffected by the initial c-Si surface condition. However, these outstanding D_{it} values are typically obtained after additional *hydrogen passivation* of the dangling bonds using, for example, the *'alneal'* technique. [5] The energy levels associated with hydrogen-terminated silicon dangling bond defects (i.e. the Si-H bonds) lie outside the silicon bandgap and thus do not contribute to the surface recombination losses. Thermally-grown SiO$_2$ films also contain some amount of *positive* fixed oxide charges Q_f located very close ($\leq$ 2 nm) to the Si-SiO$_2$ interface. Depending on the processing conditions, the Q_f at the Si-SiO$_2$ interface typically lies in the $5 \times 10^{10} - 10^{11}$ cm^{-2} range [26, 50]. As

---

[5] The *'alneal'* technique is a post-metallisation anneal where aluminium is first evaporated onto the SiO$_2$ followed by annealing in N$_2$ or in forming gas at $\sim$ 400℃.

a result thermally grown SiO_2 has demonstrated S_{eff} values as low as 2 cm/s on 1.5 Ωcm *n*-type c-Si and 12 cm/s on 1 Ωcm *p*-type c-Si [51, 52].

Although thermally grown SiO_2 films show very good surface passivation, they feature two main drawbacks with regard to solar cell fabrication. Firstly, the high processing temperatures required during thermal oxidation may severely degrade the bulk lifetime of some c-Si wafers (e.g. Czochralski or Cz-Si). Secondly, the refractive index of SiO_2 is ~1.46, which is too small for efficient reduction of reflection losses particularly after encapsulation. Hence, the SiO_2 films cannot be used as single-layer anti-reflective coating. An alternative approach is to deposit silicon oxide (in this case SiO_x since the film is not stoichiometric) by low-temperature fabrication processes such as plasma-enhanced chemical vapour deposition (PECVD) which will be described in detail in Section 2.4. The optical properties of SiO_2 can be improved by the deposition of an a-SiN_x:H film on the SiO_2. In addition to reducing reflection losses, this H-containing film also supplies H atoms to passivate dangling bonds at the SiO_2-Si interface. Such stacks for thermally grown SiO_2 and SiO_x deposited by PECVD have demonstrated S_{eff} < 10 cm/s [53, 54].

(ii)   Hydrogenated amorphous silicon nitride (a-SiN_x:H)

The most widely applied functional thin film in the field of c-Si solar cells today is a-SiN_x:H since this film can act simultaneously as an anti-reflection coating (due to a suitable refractive index tunable between 1.9-2.5), bulk passivation (due to its hydrogen content which can diffuse into the bulk), and surface passivation layer (due to its high Q_f and low D_{it}).

The most common synthesis method for a-SiN_x:H in PV is from the gas phase using chemical vapor deposition (CVD). In general, this method results in non-stoichiometric silicon nitride films due to the presence of up to 40 atomic % hydrogen. The three basic

CVD processes are the reaction of silane and ammonia at atmospheric pressure and at 700 – 1000 ºC temperature (APCVD), the reaction of dichlorosilane and ammonia at reduced pressure (0.01 – 1 Torr) and temperature (700 - 800ºC) (LPCVD) and plasma-enhanced reaction of silane and an ammonia + nitrogen mixture at reduced pressure (0.01 – 1 Torr) and low temperature of < 500ºC (PECVD) [26]. The PECVD method is the most popular and of greatest interest due to its low-temperature advantage.

The electrical and optical properties of a-SiN$_x$:H films strongly depend on the processing parameters. The fixed charge density Q_f in a-SiN$_x$:H is positive and can reach values as high as 8×10^{12} cm^{-2} [55]. Such high values of positive Q_f provides highly effective field-effect passivation on n-type and n^+-type surfaces. In addition, due to its hydrogen-rich nature, a-SiN$_x$:H films also demonstrate very low D_{it} values in the range 5-9 $\times 10^{11}$ eV^{-1}cm^{-2} [55, 56]. Corresponding S_{eff} values on Cz-Si wafers (resistivity between 1 to 5 Ωcm) can be as low as 2 cm/s (on n-type c-S), 15 cm/s (on n^+-type c-Si), and 5 cm/s (on p-type c-Si) [55, 56]. Furthermore, it is shown that a-SiN$_x$:H is in general firing stable, which means it can withstand the high temperatures (~800 ºC) necessary for the firing of metal contacts in the fabrication of c-Si solar cells. As a result of these excellent optical properties, surface passivation properties and firing stability, a-SiN$_x$:H is widely used today as the front (monofacial) and rear (bifacial) passivation and ARC layer in silicon wafer solar cells.

(iii) *Hydrogenated amorphous silicon (a-Si:H)*

The current world record efficiency for a c-Si solar cell is held by Panasonic Cooperation for a HET solar cell with an efficiency of 25.6% [57, 58]. This achievement can partly be attributed to the excellent level of c-Si surface passivation demonstrated by intrinsic hydrogenated amorphous silicon (a-Si:H) used in this solar cell structure. S_{eff} values as low as ~1.5 cm/s are achieved, corresponding to outstanding

V_{oc} values of 750 mV [58]. Consequently, the passivation of c-Si by a-Si:H is a very active research area.

a-Si:H samples, typically deposited by the PECVD process, have demonstrated excellent passivation properties on *p-* and *n*-type c-Si with S_{eff} values as low as 0.75 cm/s and 7 cm/s, respectively [42, 59]. The main challenge in the application of a-Si:H in solar cells is their relatively low thermal stability. It is demonstrated that the S_{eff} improves during the first minute of annealing at ~400 ℃ (most likely due to the diffusion of hydrogen to the interface where it saturates dangling bond states) [42]. However, for longer annealing times, the passivation quality starts to degrade rapidly, dropping down by more than two orders of magnitude after annealing for 30 mins [42, 52]. Another disadvantage of a-Si:H is its high absorption in the UV part of the solar spectrum. Hence, the a-Si:H film thickness at the front of the solar cell should be kept as low as possible.

(iv) Titanium dioxide (TiO$_2$)

TiO$_2$ demonstrates ideal optical properties when used as an anti-reflection coating (ARC) due to its refractive index of ~2.4 and low absorption in the visible range. In fact, it was traditionally used as an ARC in silicon solar cells well before SiN$_x$ but was gradually replaced by SiN$_x$ due to its poor passivation quality. However, Liao *et al.* recently demonstrated excellent surface passivation with TiO$_2$ deposited by thermal ALD at 100°C using TiCl$_4$ and H$_2$O as precursors, on low-resistivity boron-doped c-Si [60, 61]. They achieved low effective surface recombination velocities down to 2.8 cm/s and 8.3 cm/s on *n*-type and *p*-type FZ c-Si wafers, respectively. Good passivation quality with TiO$_2$ could be achieved after a PDA in combination with a subsequent light-soaking step.

Interestingly, ultrathin (1-4 nm) films of TiO_2 are also potentially suitable as a part of an electron-selective contact [60, 62]. The selectivity of this film is achieved through band alignment. Yang *et al.* demonstrated that 4.5 nm of TiO_2 prepared by ALD (using $Ti(O^iPr)_4$ and H_2O at 230°C) can yield a relatively low contact resistivity and can successfully passivate the Si surface with a saturation current density of 25 fA/cm^2 [63]. Combining this ALD TiO_2 with a 1.5 nm SiO_2 interlayer, they demonstrated a 20.5% champion conversion efficiency. In more recent work with further optimisation, they implemented a full-area TiO_2-based contacts with stable surface passivation and low contact resistivity, after a forming gas anneal, yielding a champion efficiency of 21.6% on *n*-type silicon solar cell [64].

(v)   *Aluminium oxide (Al_2O_3)*

Al_2O_3 was first applied for c-Si surface passivation in metal-insulator-semiconductor (MIS) solar cells by Hezel and Jaeger in the 1980s [65]. They demonstrated a reasonable level of surface passivation on 2 Ωcm *p*-type c-Si with a reported S_{eff} of ~200 cm/s. The D_{it} value was also found to be unaffected by UV radiation, in contrast to the strong increase in the interface defect density for a-SiN_x:H and thermal SiO_2 on c-Si [66]. The key result from this early study was that Al_2O_3 had a relatively low mid-gap D_{it} of ~$1x10^{11}$ $eV^{-1}cm^{-2}$ and, more importantly, that Al_2O_3 contains a *negative* fixed charge density Q_f of about $3x10^{12}$ cm^{-2}. With this property, Al_2O_3 stands out from the other dielectric thin films SiO_2 and a-SiN_x:H which both contain positive fixed charges. Despite these early reports, Al_2O_3 for the surface passivation of c-Si only picked up considerable interest over the last decade when Agostinelli *et al.* and Hoex *et al.* reported ultra-low surface recombination velocities for Al_2O_3 deposited by thermal and plasma-assisted ALD, respectively [66, 67]. Hoex *et al.* demonstrated record $S_{eff,max}$ values as low as 13 cm/s on 2.0 Ωcm *p*-type FZ silicon and 2 cm/s on 1.9 Ωcm *n*-type FZ-Si. The Al_2O_3 films in these studies were subjected to a post-deposition anneal at

425 ºC for 30 minutes in an N_2 environment to achieve these levels of passivation. Further, it was shown that ultra-thin films of 7 nm thickness still yielded $S_{eff} < 5$ cm/s on 1.9 Ωcm *n*-type FZ-Si.

As the interest in Al_2O_3 steadily grew, it was demonstrated that Al_2O_3 demonstrated particularly excellent passivation of boron-doped p^+-type c-Si surfaces due to its high negative Q_f. A negative fixed charge density is preferred for heavily doped p^+ surfaces since it leads to a layer of deep accumulation at the Al_2O_3–Si interface. Deep accumulation implies that $p_s >> n_s$ at the interface which is highly beneficial to reduce surface recombination as discussed in Section 2.2.2. By contrast, a positive fixed charge density (as in SiO_2 and a-SiN_x:H films) would result in depletion ($n_s \approx p_s$) or inversion ($n_s >> p_s$) at the interface of a p^+-type c-Si surface depending on the magnitude of Q_f. Accumulation and inversion both give low S_{eff} values but depletion is detrimental to surface recombination and highly undesirable. The magnitude of positive Q_f required to avoid depletion depend strongly on the doping concentration of the p^+-type surface. On the other hand, a negative Q_f leads to accumulation irrespective of the degree of p^+ doping. Due to this reason, Al_2O_3 is preferred over positively charged dielectrics for the surface passivation of p^+-type c-Si [18, 68-70]. A large magnitude of positive Q_f can induce a highly inverted layer at the p^+-type c-Si surface, however, studies on solar cell devices have demonstrated that the coupling of this inversion layer to the base contact leads to a significant loss in the short-circuit current density [71].

Al_2O_3 films can be manufactured by various deposition techniques e.g. rf sputtering, ALD and PECVD. ALD offers the advantage of precise thickness control along with unique conformity and uniformity on textured surfaces which is difficult to achieve with PECVD. Furthermore, ALD Al_2O_3 films typically yield the best passivation performance although PECVD comes very close [72-74]. On the other hand, PECVD

and sputtering generally provide higher throughput and are well established in solar cell manufacturing. It should be noted, however, that the limitations of the conventional ALD method in terms of growth rate and throughput are not fundamental and can be overcome with the use of batch processes and new developments as will be highlighted in Section 2.4.

Due to their excellent surface passivation properties, Al_2O_3 films are now widely used in *p*-type aluminium local back surface field (Al-LBSF) or passivated emitter and rear contact (PERC) solar cells in a stack with a capping SiN_x layer as well as in *n*-type bifacial and monofacial solar cell structures as the passivating layer for the p^+ emitter. Efficiencies of 21.7% for *p*-type PERC (or Al-LBSF) solar cells [75] and 25% for *n*-type tunnel-oxide passivated contact (TOPCon) solar cells with Al_2O_3 passivating layers have been achieved to date [76, 77]. In Figure 2.10, a schematic overview of interface properties of various passivation layers is presented.
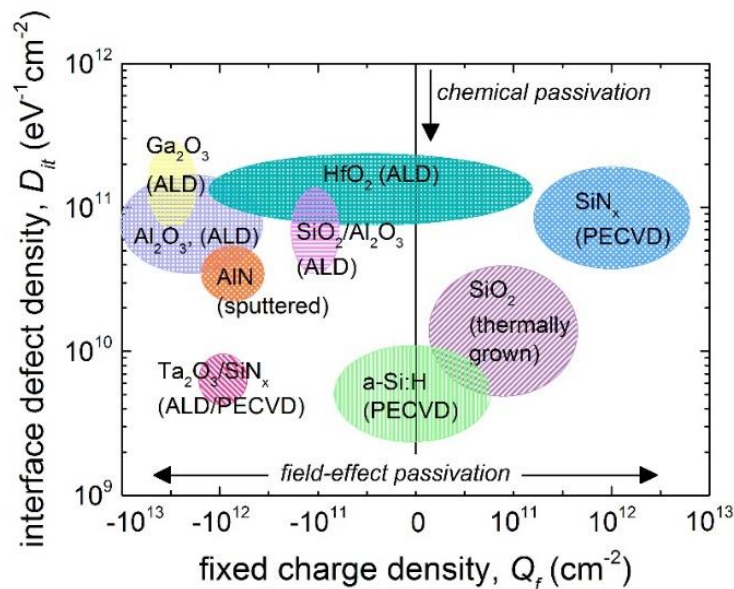
Figure 2.10 Schematic overview of typical interface defect densities and fixed charge densities of passivation scheme. Note that the actual interface properties depend strongly on the fabrication conditions. Adapted from Ref. [78] and [79].

2.3.2 Transparent conductive oxides

Transparent conducting oxides (TCOs) are an important component of thin film and amorphous silicon heterojunction solar cells where they act as electrode elements, templates for the growth of additional layers and diffusion barriers. The desirable characteristics of TCO materials are common to all PV technologies and include a high optical transparency across a broad spectral range and a low electrical resistivity. Furthermore, the TCO materials must be low-cost to be viable in the PV industry. The antagonistic properties of conductivity and transparency are quite challenging to achieve due to the free carrier absorption that accompanies high carrier concentration. As a trade-off, TCO materials are required to have a moderate carrier concentration and high carrier mobility, a combination which provides good conductivity and ensures low carrier absorption. Another challenge is to obtain conductive TCO films at a relatively low substrate temperature e.g. due to the thermal stability of doped and undoped a-Si:H. The electronic properties of most TCO materials improve when deposited at temperatures above 250 °C [80, 81].

The resistivity ρ (in Ωcm) of TCOs is determined by both the free carrier concentration N_c (in cm^{-3}) and the electron or hole mobility μ_c (in $cm^2V^{-1}s^{-1}$). The conductance is given by

$$\sigma = qN_c\mu_c = qN_c\left(\frac{q\tau}{m_c^*}\right) = q^2N_c\frac{\tau}{m_c^*} \tag{2.23}$$

where q is the elementary charge, m_c^* is the effective carrier (electron or hole) mass and τ is the carrier lifetime. The mobility scales proportionally with τ which signifies the time between carrier collisions. Since most TCOs are *n*-type with electron free carriers, we refer to only electron concentration and mobility hereon. The electron mobility in TCOs can vary between 0 to 100 $cm^2V^{-1}s^{-1}$[82]. The dominant mechanisms

that limit the carrier mobility are ionised impurity scattering and grain boundary scattering.

For silicon wafer solar cells it is important that the TCO material has a high transparency in the 300-1200 nm range. As a result, materials with large bandgaps (> 3.5 eV) are preferred. A brief overview of some commonly used TCOs is provided below with a focus on indium tin oxide (ITO) and zinc oxide (ZnO) [83].

(i)   Indium tin oxide (In$_2$O$_3$:Sn) or ITO

The most widely used TCOs across the electronic and photovoltaic industry is ITO, a doped semiconductor with a bandgap E_g = 3.7 eV. Two types of ITO are commonly used: crystalline ITO (*c*-ITO) and amorphous ITO (*a*-ITO). Currently, *c*-ITO deposited onto substrates heated to 250-350 ℃ provide the lowest resistivity (~1×10^{-4} Ωcm) [83]. A room temperature (25 ℃) alternative to *c*-ITO is *a*-ITO, although its electrical properties are slightly inferior compared to the former.

The standard process for fabrication of ITO is magnetron sputtering. In general, ITO is deposited from sintered ceramic In$_2$O$_3$ targets containing between 3 wt% and 10 wt% SnO$_2$ in a low-pressure inert gas (e.g. Ar) environment. ITO is an *n*-type semiconductor, and the resistivity of sputtered ITO can be tuned by varying the oxygen partial pressure during deposition. This is because the free electrons that contribute to the conductivity of ITO largely arises from double-charged oxygen vacancies in addition to the dopant substitution of Sn in the In$_2$O$_3$ crystal. ITO can show carrier mobilities up to ~50 cm^{2}V^{-1}s^{-1} while its carrier concentration can vary in the range of (1-8)×10^{20} cm^{-3} [83, 84]. At the same time, ITO films show excellent optical transparency with transmittance of > 90%. As is usually the case with TCOs, ITO shows a degradation of electrical properties on annealing at temperatures > 200 ℃.

This is attributed to the additional scattering centres formed along with new crystallised regions which significantly deteriorate the electron mobility [84].

Despite the excellent optoelectronic properties of ITO, the increasing price and scarcity of indium has steered attention in the PV sector towards more cost-effective TCO materials, the most popular one presently being ZnO.

(ii)　　*Zinc oxide (ZnO)*

Zinc oxide is used extensively in a large spectrum of applications. It is mixed into paints to give them a 'china white' colour, is an additive in rubber and plastics, is used in the pharmaceutical and cosmetics industries in talc and sun creams, and also in coatings for paper [85]. It has also been systematically investigated as a compound semiconductor in the electronics industry since the beginning of the semiconductor age [86, 87]. However, there has been a recent renewed interest in ZnO as an optoelectronic material because of its prospective use as a wide bandgap (3.3 eV) semiconductor for light-emitting devices and for transparent and conductive electronics [88].

ZnO can be prepared by a variety of techniques: magnetron sputtering, chemical vapour deposition, pulsed-laser deposition, atomic layer deposition, and spray pyrolysis [89]. Of these, sputtering and chemical vapour deposition are large-area (> 1 m^2) techniques established in the industry.

In the intrinsic (undoped) form, the conductivity of ZnO can vary in a wide range, depending on the material fabrication techniques and processing conditions. In general, intrinsic ZnO is an *n*-type semiconductor. The presence of intrinsic defects such as V_{Zn} and V_O vacancies, Zn_i and O_i interstitials and Zn_O and O_{Zn} substitutional defects act as dopants in the ZnO lattice making it conductive. Since the level and type of intrinsic defects can only be controlled in a narrow range depending on the material synthesis technique, dopants are used to increase the conductivity of ZnO for application as a

TCO. High carrier concentrations (N_c) up to 1.5×10^{21} cm^{-3} with resistivities as low as 2×10^{-4} Ωcm are achieved by the addition of dopants such as boron and aluminium [85]. The highest mobilities for doped ZnO are in the range of $50 - 60$ cm^{2}V^{-1}s^{-1} [90]. The mobility of homogenously-doped degenerate ZnO (similar to ITO and other TCO materials) is limited by ionised impurity scattering. For amorphous silicon cells, the degenerately *n*-doped ZnO forms an electrical contact to a highly *p-* or *n*-type a-Si layer. In thin-film Cu(In,Ga)Se$_2$ cells, doped ZnO forms part of the *p-n* junction and to obtain higher efficiencies, a bilayer structure of a thin (~50 nm) intrinsic ZnO and a highly *n*-doped layer is typically used.

The main advantage of ZnO over ITO is that it is much cheaper, a pre-requisite for large-area PV technologies. In addition, it is abundant in the earth's crust (in the form of the mineral zincite), is non-toxic, and can be fabricated at low temperatures. Hence, there is a keen interest in ZnO as a replacement for ITO, which is expensive, toxic and scarce. A summary of the electrical properties of common TCOs in PV is presented in Table 2.1.

Table 2.1 Resistivity (ρ), carrier concentration (N_c), and carrier mobility (μ_c) of transparent conductive oxides common to optoelectronic applications

No.	TCO	Resistivity, ρ (Ωcm)	Carrier concentration, N_c (cm^{-3})	Carrier mobility, μ (cm^{2}V^{-1}s^{-1})	Ref.
1	In$_2$O$_3$:Sn (ITO)	$(1-3)\times10^{-4}$	$(1-10)\times10^{20}$	50	[83]
2	SnO$_2$:*X*	$(3-5)\times10^{-4}$	-	-	[91]
3	In$_2$O$_3$	$3-4\times10^{-4}$	2×10^{20}	140	[92]
4	ZnO	1×10^{-2}	7×10^{19}	30	[93]
5	ZnO:Al	1×10^{-3}	5×10^{20}	6	[94]
6	ZnO:B	1.5×10^{-3}	3×10^{20}	8-10	[95]
7	ZnO:Ga	$(1-3)\times10^{-4}$	4×10^{21}	11	[96]
8	ZnO:In	3×10^{-3}	6×10^{20}	3-5	[97]

2.4 Deposition techniques for functional thin films in PV

In this section, a brief description of the common techniques used for the fabrication of functional thin films is provided. These include thermal oxidation (used for SiO_2), PECVD (used for a-Si:H, SiO_x, a-SiN$_x$:H and AlO_x), magnetron sputtering (used for ITO and ZnO) and ALD (used for Al_2O_3 and ZnO).

2.4.1 Thermal oxidation

The thermal oxidation of silicon wafers occurs in a clean quartz tube which is held at $800 - 1200$ ºC using external resistive heaters. Ultra-pure oxygen (or water vapour) enters the quartz tube via one end, passes through the tube, and leaves it through the other open end, causing the dry oxidation (or wet oxidation) of silicon samples within the tube [26].

$$\text{Si (solid)} + O_2 \quad\rightarrow\quad SiO_2 \text{ (solid)} \qquad\qquad (dry\ oxidation) \quad (2.24a)$$

$$\text{Si (solid)} + 2H_2O \quad\rightarrow\quad SiO_2 \text{ (solid)} + 2H_2 \qquad (wet\ oxidation) \quad (2.24b)$$
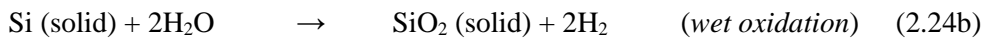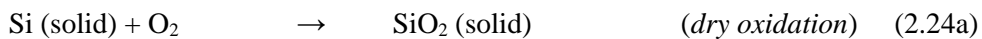
This is the method that enables oxide growth *into* a silicon wafer by consuming the underlying c-Si. As the SiO_2 layer grows, O atoms from the tube must diffuse through the existing and growing SiO_2 layer in order to reach more Si atoms to oxidise. As a result, the growth rate reduces with increasing oxidation time. As the oxide grows into the wafer, the oxidation process generates a new interface within the wafer. This displacement of the interface to cleaner regions within the silicon wafer is one of the main reasons for the excellent quality of thermally grown Si-SiO_2 interfaces.

2.4.2 Plasma-enhanced chemical vapour deposition (PECVD)

PECVD is used extensively in the PV industry for the deposition of a large number of passivation films, including a-Si:H, a-SiN$_x$:H, AlO_x and SiO_x. Industrial PECVD reactors are of two main types: direct plasma and remote plasma reactors. The direct

plasma reactors are parallel-plate reactors where the processing gases are excited using an electromagnetic field and where the wafers are located within the plasma. This makes the plasma frequency a crucial parameter, which can, in turn, be divided into low-frequency (10 - 500 kHz) and high frequency (> 4 MHz). Direct plasma reactors are in general static deposition systems with a stationary stage for substrates.
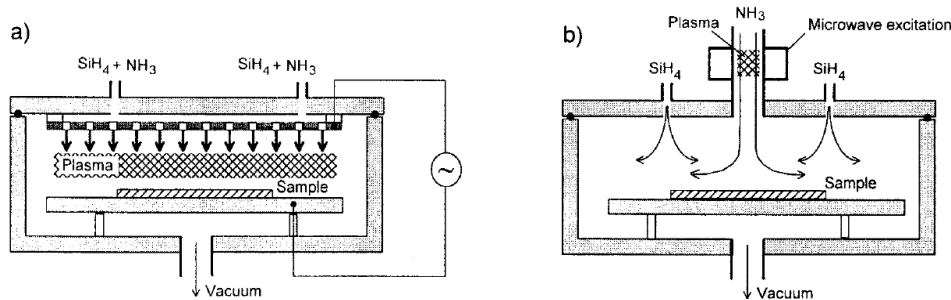
Figure 2.11 Schematic of a laboratory-type (a) direct-plasma PECVD reactor where wafers are located within the plasma and all processing gases are excited by the electromagnetic field, and (b) a remote-plasma PECVD reactor where ammonia is excited by microwaves and the wafer is located outside the plasma excitation zone. The case for SiN_x is presented. Illustration from Ref. [98].

On the other hand, in remote-plasma reactors, the substrates are placed outside the plasma zone, and the plasma is excited using, for example, microwaves. This decoupling of the plasma source and the stage for the substrates allows samples of arbitrary shape and size to be used. Furthermore, the lower ion energies in this process minimise surface damage and thus this reactor is considered better suited for the deposition of surface passivation layers in solar cells. The remote plasma technique can be further categorised into static and dynamic deposition. In static deposition, as the name suggests, the substrates are stationary during deposition whereas in dynamic deposition the substrate is moving within the reactor during deposition. Remote plasma PECVD has a very high throughput (> 2,000 wafers/hr) and is commonly used in the PV industry for large-scale manufacturing.

2.4.3   Magnetron sputtering

Magnetron sputtering is an industrially proven high-rate and high-precision coating technology based on straightforward and robust components [99]. Developed in the early 1970s, this technique is essential to the industrial manufacturing of thin-film solar cells for the deposition of TCOs. It is a high-vacuum deposition process where atoms are sputtered from a metallic or compound target plate. This plate is the cathode of a glow discharge process while the anode is the chamber of the vacuum system. The sputtered atoms are transported to the substrate through a low pressure (typically ~10 Pa) plasma environment. Film growth occurs by the condensation of neutral atoms and at the same time the bombardment of species from the plasma which together promote the formation of the desired compound on the substrate. The so-called 'magnetron' process increases the sputter current by magnetic confinement of the plasma in front of the target as shown in Figure 2.12. This allows high-rate deposition at lower pressures which is essential for the cost-effective growth of high-quality films. Since the coating material is passed into the vapour phase via momentum exchange caused by energetic particle impact (rather than by a chemical or thermal process), any material is a candidate for coating. Alloys and compounds (e.g. ZnO:Al) can be sputtered either reactively from a metallic allow target, where reactive gas is introduced into the process chamber, or from ceramic compound targets in a pure Ar atmosphere.
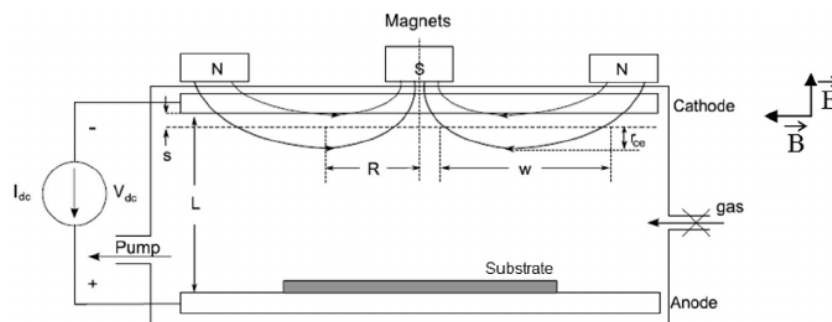
Figure 2.12 Schematic of a conventional dc magnetron sputtering discharge. Illustration from Ref. [100].

2.4.4   Atomic layer deposition (ALD)

With the advance of the silicon-based microelectronics industry in the late 1990s to the early 2000s, atomic layer epitaxy, a technique first developed in the 1970s, began to gain considerable interest and the term 'atomic layer deposition' was coined to better suit the application of this technique. As the name suggests, thin films are built up layer-by-layer in cycles during ALD in which a sample substrate is exposed to alternating doses of various vapour- or gas-phase species. In each cycle, a sub-monolayer of material is deposited[6] [101]. A typical ALD cycle consists of four stages, as illustrated in Figure 2.13.
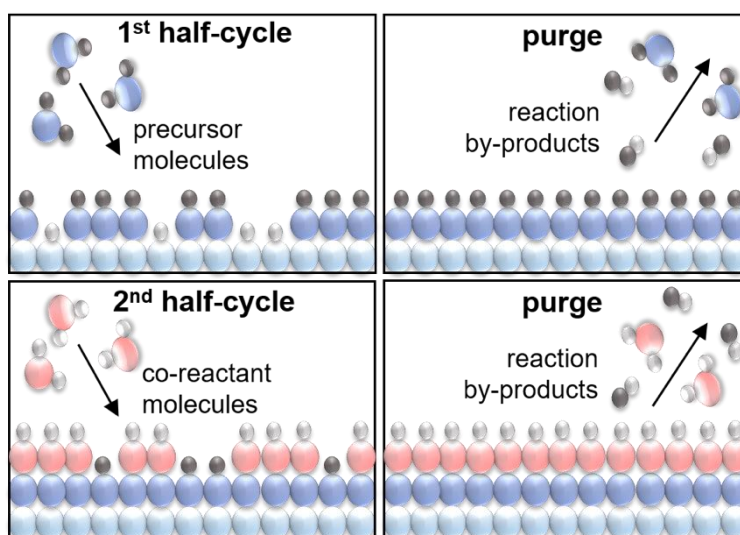
Figure 2.13 Schematic representation of the main steps in one ALD cycle which consist of the first half-cycle (precursor) and second half-cycle (co-reactant) which are self-limiting surface reactions. The two half-cycles are separated by purge steps.

In the first step, the sample is exposed to a *precursor* (in general an inorganic compound consisting of a metal surrounded by functional groups or *ligands*). In the second step, a purge is conducted to clear the reactor of any remnant precursor. In the next step, the sample is exposed to a *co-reactant* (typically a smaller molecule e.g.

---

[6] As a result of steric hindrance and limited density of reactive groups on the surface, the growth per cycle is typically less than a monolayer. Note that this does not affect the ability to grow a closed, dense film.

H₂O). This is followed by the final fourth step; a purge is conducted again to clear the reactor. In the first and third steps, the precursor and co-reactant contribute atoms to the sample surface that lead to film growth via two *half-cycles*. In many cases, the precursors deposits its metallic centre in the 1ˢᵗ half-cycle while the co-reactant deposits a non-metal such as O, N, S, etc. in the 2ⁿᵈ half-cycle. The key to an ALD process is that the precursor and co-reactants undergo *self-limiting* reactions with the sample surface. This means that the surface reactions are limited by the presence of chemical groups and/or surface sites that are accessible. All surface reactions stop once the available sites and groups are saturated. The precursor molecules and co-reactants do not react with the surface groups that they have created and also never react between themselves. This is ensured by the pump and/or purge steps which remove any excess precursor or co-reactant molecules from the reactor (to avoid any direct gas-phase reactions), as well as the by-products from the surface reactions. The saturation of both half-cycles leads to a characteristic amount of *growth per cycle* or *GPC*. To reach a certain target film thickness, the two half-cycles are repeated in an ABAB fashion. Due to its self-limiting surface reactions, ALD results in the growth of highly conformal and uniform films with precise thickness control which is necessary for a variety of micro-scale and nano-scale applications. Currently, the library of materials possible by ALD include metal oxides, nitrides, carbides, chalcogenides, metals etc.
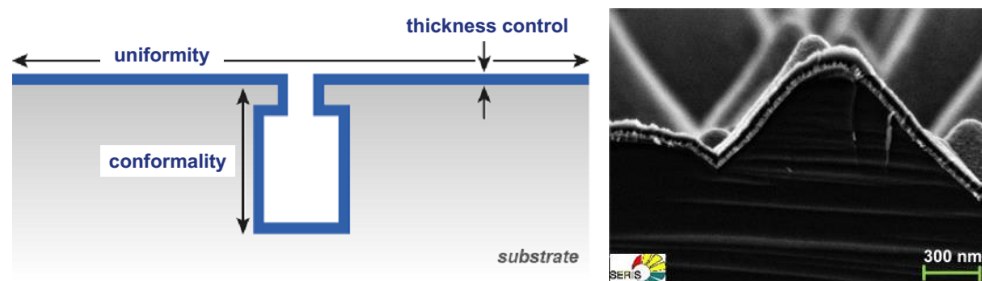
Figure 2.14 (Left) Schematic of the advantages of ALD: film uniformity on a planar surface, conformity over 3D features and precise film growth control. Adapted from Ref. [101]. (Right) Scanning electron micrograph of a Al₂O₃/ZnO film stack deposited by ALD on a textured c-Si surface, demonstrating high uniformity and conformity at the pyramid peak and valley.

2.5   Atomic layer deposition of thin films in photovoltaics

ALD was first introduced to photovoltaics in 2004 by Agostinelli *et al.* who investigated the surface passivation properties of Al_2O_3 fabricated by ALD [102]. In the following years, the PV community's interest in ALD grew strongly as a consequence of the excellent passivation results obtained for Al_2O_3 films deposited by ALD. Today, Al_2O_3 layers prepared by ALD can account for a ~1% absolute increase in conversion efficiency of commercial c-Si solar cells and have been incorporated in solar cells with record efficiencies of > 25% on the lab-scale [77, 79].

The success of ALD Al_2O_3 also triggered the exploration of ALD for the preparation of other functional layers for various commercial solar cells. For example, ALD is also used for the deposition of TCOs such as ZnO and In_2O_3 yielding good transparency and conductivity. The application of ALD in PV comes with the unique advantages of high material quality, precise thickness control, large-area uniformity and conformal film growth. In this section, a brief overview of the application of ALD in high-efficiency c-Si solar cells will be discussed with a focus on the implementation of an industrial-scale ALD technique.

2.5.1   Spatial atomic layer deposition (spatial ALD)

In conventional (or *temporal*) ALD, the four steps in the ALD cycle are separated in time. Of the four steps, particularly the purging or pumping cycles are very time-intensive. Insufficient purging can result in a direct reaction between the precursor gases giving rise to a less-controlled CVD part of the reaction. Hence, for pure ALD growth, lengthy purging cycles are necessary. As a consequence, the growth rate and throughput of conventional (temporal) ALD is limited for single wafer reactors (e.g. ~1 wafer/hour for Al_2O_3 films). Such a low throughput is not viable on the industrial scale and can significantly increase the cost of operation in solar cell manufacturing.

The success of ALD Al_2O_3 as a passivating layer was sufficient incentive to lead to the development of high-throughput ALD systems suitable for the industry. Higher throughputs are achieved in the semiconductor industry with the use of more expensive batch ALD reactors (3-10 \$/wafer, 10-50 wafers/hr).[7] This is the approach pursued by companies such as Beneq and ASM [103, 104]. However, the PV industry is much more demanding when it comes to throughput and costs (0.03-0.05\$/wafer, 1000-3000 wafers/hr) [79]. To compete with PECVD and PVD deposition techniques, ALD must meet the requirements of high throughput and low cost.
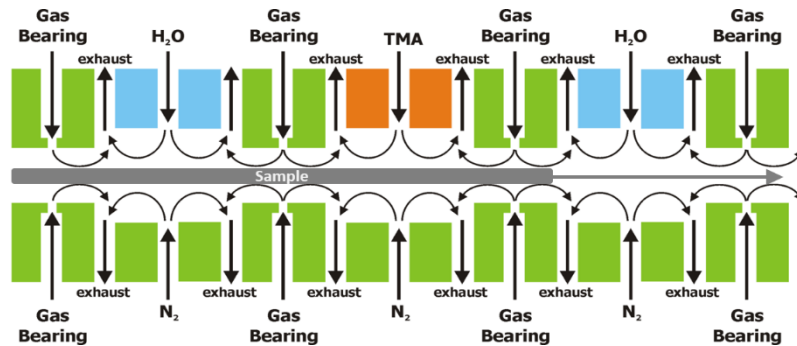
Figure 2.15 Schematic representation of a spatial ALD reactor with spatially separated precursor (TMA) and reactant (H_2O). Adapted from [105, 106].

This is achieved with the recent development (in the year 2009) of atmospheric-pressure *spatial* ALD where the precursor and co-reactant are separate in *space* rather than in time [73, 105]. In spatial ALD, the precursor and co-reactant gases are typically separated by N_2 curtains that prevent the gases from mixing, as illustrated in Figure 2.15. A wafer is then moved across these gaseous inlets and each point along the wafer is exposed to a cycle of spatially separated precursors (N_2-precursor-N_2-reactant-N_2) which effectively results in one ALD cycle. In this way, the lengthy purge cycles are avoided and high throughput (> 3000 wafers/hr) can be achieved. Also, spatial ALD is generally an atmospheric process which does not require vacuum, which helps to

---

[7] It should be noted that the reported requirement in the semiconductor industry is in the range of 10-50 wafers. However, batch reactors can also be scaled up to throughputs of 500-1000 wafers/hr by placing a larger number of wafers (back-to-back) in each batch.

reduce costs further. The development of spatial ALD has paved the way for the wide-scale application of ALD in the PV industry. Examples of companies currently manufacturing spatial ALD equipment are SoLayTec and Levitech [107, 108].

2.5.2   ALD passivation layers in homojunction c-Si solar cells

The solar cell structures increasingly gaining popularity in the PV industry are the PERC and Al-LBSF solar cells which are based on p-type c-Si with a n^+ homojunction emitter (Figure 2.16a) [109]. The key advantage of Al-LBSF over standard p-type silicon solar cells is the use of local contacts instead of a full-area Al contact (see Figure 2.1). The non-contacted rear surface region is passivated by a dielectric film and the whole rear is covered with an Al rear electrode. This dielectrically displaced Al rear also has a significantly higher reflection for near-bandgap photons compared to a standard Al-BSF rear, thereby further improving the solar cell efficiency. Since ALD of Al_2O_3 has proven to be very successful at the passivation of lowly-doped p-type Si, it is a natural candidate for incorporation in the rear passivation stack. Al-LBSF cells with ALD Al_2O_3 have yielded efficiencies of up to 21.7% [75]. In fact, the application of Al_2O_3 in this type of cell paved the way for ALD in solar cell manufacturing.
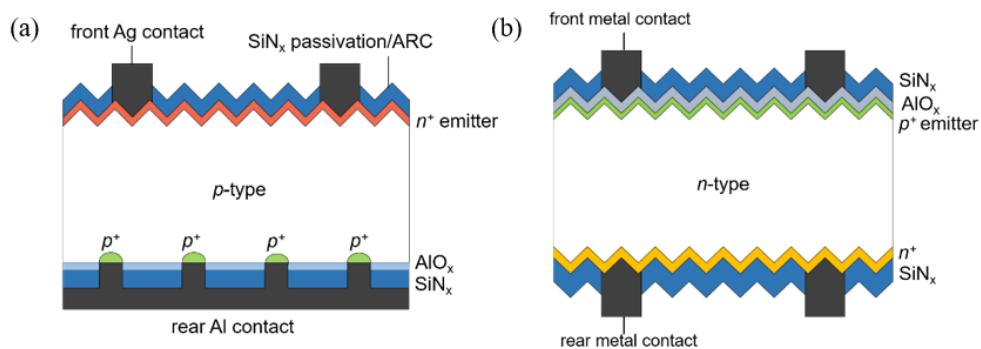
Figure 2.16 High-efficiency homojunction c-Si solar cell concepts: (a) p-type aluminium local back surface field (Al-LBSF) solar cell structure and (b) n-type bifacial front and back contact (nFAB) structure.

In addition to high-quality surfaces, a good quality bulk is also essential to pushing the limits of c-Si cell efficiencies. A better bulk quality is achieved with *n*-type c-Si wafers instead of *p*-type c-Si wafers. In *n*-type cell structures, a boron-doped p^+ layer functions as the emitter (Figure 2.16b). For a long time, such a cell structure was difficult to fabricate due to the lack of a suitable passivation scheme for p^+ until the breakthrough with Al_2O_3. With the application of ALD Al_2O_3 for the emitter passivation, *n*-type solar cell structures have achieved conversion efficiencies of up to 23.9% [70, 110].
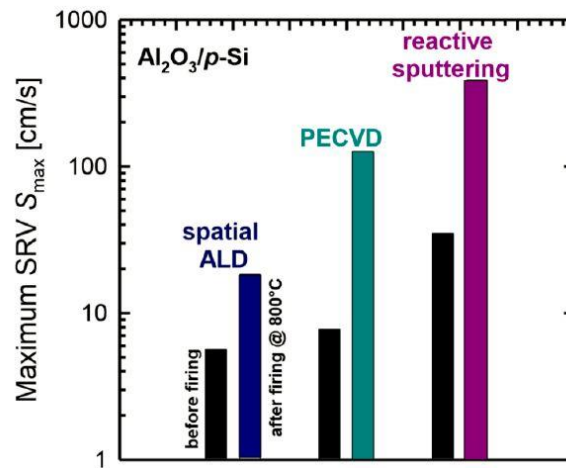
Figure 2.17 Comparison of the upper limit of surface recombination velocity, S_{max} of Al_2O_3 films prepared on c-Si by spatial ALD, PECVD and sputtering (where a lower S_{eff} is desired). Graph from Ref. [111].

Besides ALD, the PECVD and sputtering techniques are also suitable for the passivation of c-Si surfaces. PECVD in particular is a strong competitor for ALD in the PV industry since PECVD reactors are already used in most production lines for the deposition of SiN_x films. However, the drawback of PECVD is its difficulty in growing ultra-thin (< 2 nm) conformal Al_2O_3 layers (sufficient for silicon passivation), which can be achieved by ALD. Such thin layers are of interest for high-volume manufacturers to reduce costs. Moreover, in direct comparisons, the best passivation properties of Al_2O_3 have, until now, been achieved by ALD. For example, Schmidt *et al.* demonstrated in 2010 that Al_2O_3 deposited by spatial ALD showed better

performance when compared to PECVD and reactive sputtering (results presented in Figure 2.17) [111]. It is important to note, however, that research in Al_2O_3 is still ongoing and that significant improvements in each fabrication technique have been made since then.

2.5.3 ALD TCOs in heterojunction c-Si solar cells

A heterojunction, as the name suggests, is a junction formed by combining two dissimilar materials. In the case of c-Si heterojunction solar cells as shown in Figure 2.18, intrinsic and doped hydrogenated amorphous Si (a-Si:H) layers are used for the passivation of the Si surfaces and to achieve selectivity for the extraction of charge carriers, respectively. This type of solar cell has been successfully developed by Panasonic Corporation to record cell efficiencies up to 25.6%, currently the highest achieved for any c-Si wafer solar cell [58]. This solar cell is typically an *n*-type c-Si base wafer passivated with a-Si:H (*i*) layers with a p^+ doped a-Si:H layer making up the front emitter and an n^+ doped a-Si:H layer constituting the back-surface-field region at the rear. One difference between homojunction and HET solar cells is that the former have metal contacts to highly doped Si regions whereas the latter has metal contacts to TCOs. Lateral conductivity in the a-Si layers is very poor and thus TCO layers are added on both sides to improve the conductivity to the metal contacts. The fabrication of TCO layers must fulfil the following pre-requisites: low deposition temperature ($\leq$ 250 ℃), low-energy species during deposition (to prevent damage to underlying layers), as well as high conductivity and high transparency, all of which can be achieved with ALD. As a result, the deposition of various TCOs using ALD is of great interest [92, 112-114].
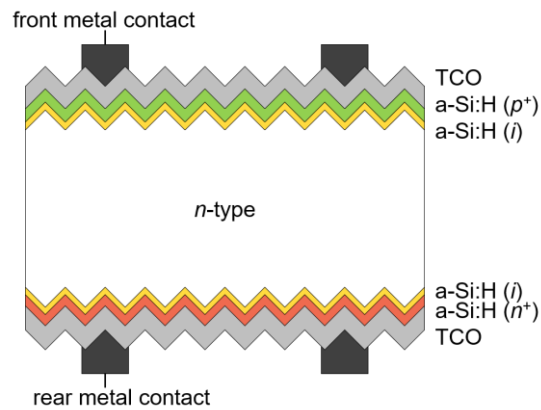
Figure 2.18 Schematic of an a-Si:H/c-Si heterojunction (HET) solar cell structure.

2.6.   Conclusion

This thesis focuses on the development and investigation of functional surface passivation layers and transparent conductive oxides deposited by the industrial-scale spatial ALD technique. Chapter 3 will describe the investigation of low-cost precursors for Al_2O_3 films deposited by spatial ALD by the comparison of their surface passivation properties. In Chapters 4 and 5, doped and undoped ZnO films deposited by the spatial ALD process will be developed for the first time to evaluate their potential for application as TCOs in the PV industry. In the remaining chapters, the developed Al_2O_3 films deposited by spatial ALD will be applied in Al-LBSF and nFAB c-Si solar cells as a passivating layer, and doped ZnO will be applied in silicon HET solar cells as a TCO.

Chapter 3: Low-cost spatial ALD of Al$_2$O$_3$ for silicon surface passivation[1]

3.1   Introduction

Aluminium oxide (Al$_2$O$_3$) films have demonstrated excellent levels of surface passivation on low resistivity n- and p-type c-Si as well as on highly doped p^+-type emitters [68, 72, 115]. More recently, it was also shown that Al$_2$O$_3$ can provide a good level of passivation for highly doped n^+-type emitters in a certain doping range [116-118]. One major difference to most other dielectric passivation layers applied so far in photovoltaics is that they usually contain a fixed positive charge density while Al$_2$O$_3$ contains a high density of fixed negative charges [102, 119, 120]. As a consequence, Al$_2$O$_3$ films show better passivation on p- and p^+-type surfaces as the minority electrons are shielded resulting in accumulation conditions. A nice result of this is a negligible injection level dependence of S_{eff} on p-type silicon unlike what is typically reported for p-type samples passivated with, for example, silicon nitride. In addition, these accumulation conditions prevent parasitic shunting at the rear of locally contacted and passivated p-type silicon solar cells [71, 121]. Following these results, there has been much interest in the PV community regarding the use of Al$_2$O$_3$ for surface passivation in industrial solar cells. In early reports, ALD-Al$_2$O$_3$ was used in p-type passivated emitter and rear contact (PERC) solar cells to passivate the rear surface achieving a champion efficiency of 20.6 % [122]. In later publications, efficiencies as high as 21.5% were obtained for similar cells with laser fired contacts at the rear [123]. For n-type solar cells in which Al$_2$O$_3$ is used for the passivation of

---

the p^+ emitter, a champion efficiency of 23.9 % was reported in 2010 [124]. More recently, *n*-type solar cell structures using Al$_2$O$_3$ layers as a tunnelling passivated contact on the front the p^+ emitter yield cell efficiencies up to 25.1 % [77, 125]. The PERC solar cell family includes the passivated emitter, rear locally-doped (PERL) or aluminium local back-surface-field (Al-LBSF) structure [109]. This particular solar cell concept is rapidly gaining popularity in the PV industry, with companies such as Trina Solar achieving record efficiencies of 22.1 % for *p*-type large-area industrial solar cells [126][2]. Consequently, the demand for Al$_2$O$_3$ films as a surface passivating layer in solar cell manufacturing has also increased significantly.

The fabrication techniques for Al$_2$O$_3$ thin films in the PV community include ALD, PECVD and physical vapour deposition (PVD) techniques (e.g. sputtering). Amongst these, ALD has been reported to provide the highest level of surface passivation e.g. by Schmidt *et al.* where Al$_2$O$_3$ films demonstrated S_{eff} ~20 cm/s on 1.3 Ωcm *p*-type FZ-Si [127]. However, despite the better performance of Al$_2$O$_3$ films deposited by ALD, this fabrication technique is not yet widely used in the silicon wafer solar cell industry. PECVD, a cost-effective and well established technique already in use in most production lines for the deposition of the SiN$_x$ antireflection coating (ARC), is the preferred choice for PV manufacturers. For the widespread adoption of ALD Al$_2$O$_3$ in the industry, the main challenge lies in making ALD as cost-effective as PECVD.

Until recently, the first concern preventing the industrial inline application of ALD was primarily the extremely low throughput of conventional (or *temporal*) ALD. Due to the long purging cycles in temporal ALD, growth rates for Al$_2$O$_3$ films were limited to ≤ 2 nm/min. Batch ALD reactors (typically 500 – 1000 wafers) offer a high-throughput alternative [128]. However, batch reactors generally require longer purge and dosing

---

[2] Note that though this record efficiency is reported for the PERC cell structure, whether or not Al$_2$O$_3$ films are used is not revealed.

times (~ nm/hr) as compared to single wafer ALD tools [79]. The concerns of the PV industry were addressed by the introduction of the *spatial* ALD technique. In spatial ALD the precursors are separated in *space* rather than in *time*. Wafers can be processed fully inline or quasi-inline, and equipment was developed with throughputs up to ~5000 wafers per hour (~nm/min), paving the way for the adoption of ALD Al_2O_3 in the manufacture of high-efficiency silicon solar cells [106, 129].

Another key concern is the relatively high cost of ownership for ALD Al_2O_3 passivation, and also for Al_2O_3 passivation in general, due to the usage of relatively expensive trimethylaluminium [TMA, $Al(CH_3)_3$] as the precursor for aluminium. The high cost of trimethylaluminium is due to the large number of distillation steps required to obtain "semiconductor-grade" TMA (due to the strict impurity requirements of the semiconductor industry [130]). These impurities include metals such as iron and copper that are well-known to reduce the minority carrier lifetime in silicon. Hence, the initial tests in the PV industry were also done using semiconductor-grade TMA.

When a lower-purity "solar-grade" TMA would be used instead, the cost of ownership for the adoption of Al_2O_3 in the PV industry would be significantly reduced. An earlier report briefly compares the passivation quality of Al_2O_3 films deposited using a cheaper solar-grade TMA to the semiconductor ("semicon") grade TMA and no significant differences were observed [131]. However, the sample size reported was fairly small and a detailed investigation was not conducted. In this work, the surface passivation mechanism and properties of Al_2O_3 films deposited using both solar- and semicon-grade TMA were investigated in more detail for a clearer comparison. High effective lifetimes were obtained for Al_2O_3 films deposited by both grades of TMA, with solar-grade TMA performing as well if not better than semiconductor-grade TMA. Further investigations revealed a lower interface defect density for solar-grade TMA and only very small differences in the fixed charge density between the two

grades. These results demonstrate that low-cost solar-grade TMA can replace semiconductor-grade TMA for the passivation of *n*-type and *p*-type c-Si surfaces in the PV industry.

3.2 Characterisation techniques used in this chapter

In this section, a brief overview of the characterisation techniques used in this chapter will be provided.

3.2.1 Quasi-steady state photoconductance decay (QSS-PC)

Photoconductance decay is the most widely used technique for measuring the effective minority carrier lifetime τ_{eff} in c-Si. As was discussed in Chapter 1, τ_{eff} is very sensitive to surface recombination, particularly for high-quality c-Si wafers with a high bulk lifetime, τ_{bulk}. In the quasi-steady-state photoconductance decay (QSS-PC) method, charge carriers are generated in the c-Si wafer during a short exposure to a light flash which briefly increases the conductance of the sample. This excess conductance then decreases over time when the excess minority carrier density is reduced by carrier recombination processes. From the derivative of this signal, an effective lifetime can be determined according to [36]:

$$\tau_{eff} = \frac{\sigma_L}{[J_{ph}(\mu_n+\mu_p)]} \ .$$

(3.1)

where σ_L is the excess photoconductance, J_{ph} is the photo-generated current density and $(\mu_n + \mu_p)$ is the sum of the electron and hole mobilities, which are well known for Si.
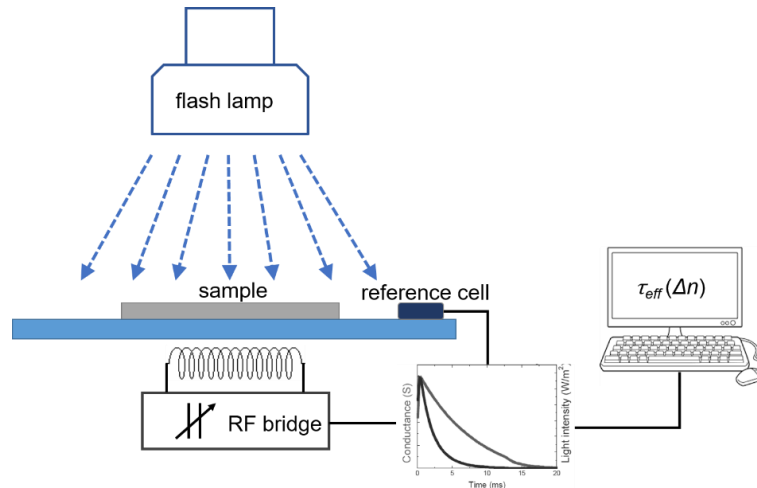
Figure 3.1 Schematic illustration of the principle of the photoconductance technique. A high-quality c-Si sample is illuminated by a short flash and the incident light intensity and wafer conductance are used to calculate the effective lifetime of the charge carriers in the c-Si wafer.

In this thesis the WTC-120 photoconductance tool from Sinton Instruments was used. The experimental setup includes a xenon flash lamp with a spectrum filtered to a range within the wavelengths of 900 to 1000 nm. When a silicon wafer is illuminated with this near-infrared light, it results in a fairly uniform distribution profile of the excess carrier density Δn in the silicon wafer. During and after the flash, the photoconductance $\Delta\sigma$ of the c-Si wafer is measured using an inductive coil in a non-contact manner. Knowing the optical properties of the measured sample allows for the determination of the photogeneration rate G within the sample. The illumination intensity from the light source is also recorded by a reference solar cell. Once the values of Δn, $\Delta\sigma$ and G are determined, τ_{eff} is calculated as a function of Δn. The WTC-120 Sinton tool operates in quasi-steady-state or transient mode. The former uses a relatively long decay time of the light intensity and is suitable to measure relatively low τ_{eff} values ($< \sim$150 µs). The transient mode uses a very short illumination (< 1 µs) and is used to measure higher τ_{eff} values. More details can be found in Refs. [36, 38].

3.2.2 Contactless corona-voltage measurement

The contactless corona-voltage (*C-V*) measurement used in this thesis is an adaptation of the extensively used corona-voltage metrology used for monitoring dielectrics and interfaces in the field of semiconductors [132, 133]. The measured quantities of interest for this thesis are the fixed charge density Q_f and the interface defect density D_{it} at the interface between a dielectric film (in this case Al_2O_3) and a c-Si substrate.

The principle of the contactless *C-V* technique is illustrated in Figure 3.2. A corona charging gun (consisting of a high-voltage needle electrode) deposits an electric corona charge, ΔQ_c of positive or negative polarity on the dielectric surface by ionising air (predominantly $[H_2O]_nH^+$ positive ions and $[CO_3]^-$ negative ions [133, 134]). The charged site is then transferred to a position under a vibrating capacitive electrode (i.e. a Kelvin probe) to determine the change in the surface potential. The surface potential is measured in the dark, as well as under illumination (using two LED light sources). The sample is repeatedly charged with the same dose of corona charge (ΔQ_c) and its *V-Q* characteristics are extracted as a basis for determining Q_{tot} and D_{it}.
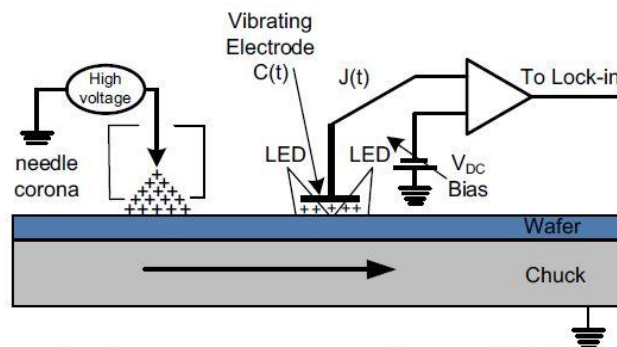
Figure 3.2 Schematic illustration of the corona charging and vibrating Kelvin probe for measurement of surface voltage in contactless corona-voltage (C-V) metrology. Adapted from [132].

In this thesis, the PV-2000 metrology platform from Semilab Inc, USA was used for contactless *C-V* measurements. In the PV-2000 system, the corona-dose spans a diameter of 15 mm and a 2 mm diameter Kelvin probe is used at a frequency of about

1100 Hz enabling fast measurements. The measured potential by the Kelvin probe is, in fact, the contact potential difference between the metal electrode and the coated semiconductor substrate:

$$V_{CPD} = \Phi_{ms} + V_{SB} + V_D \tag{3.2}$$

where Φ_{ms} is the metal electrode/semiconductor work function difference, V_{SB} is the semiconductor surface barrier, and V_D is the dielectric voltage. The Φ_{ms} contains the semiconductor work function that depends on the electron affinity χ_s and on the Fermi energy $E_C - E_F$ as shown in Figure 3.3. Each corona charging step changes the V_{SB} (written as ΔV_{SB}) and V_D (written as ΔV_D). Assuming a constant Φ_{ms} ($\Delta\Phi_{ms} = 0$), with each corona charging step $\Delta V_{CPD} = \Delta V_{SB} + \Delta V_D$.
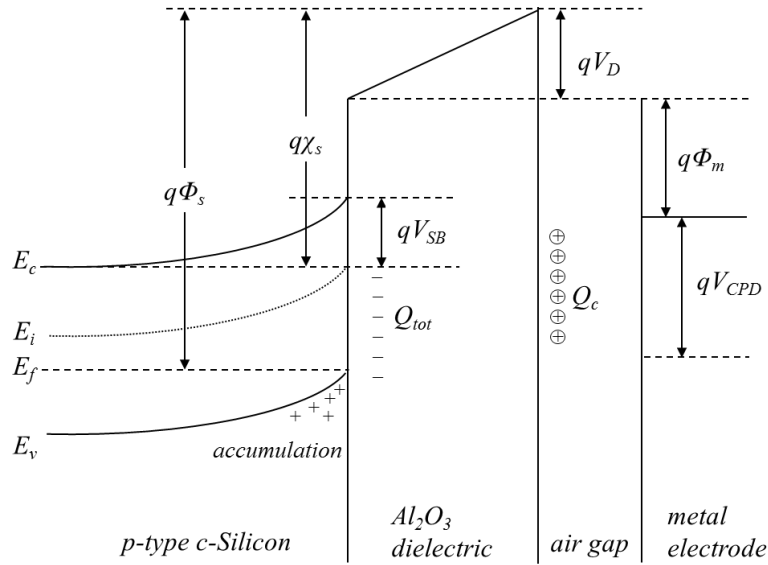
Figure 3.3 Schematic illustration of the energy band diagram of a p-Si/Al₂O₃ interface with a contactless metal electrode for the measurement of surface band-bending. E_c, E_i, E_f and E_v - conduction band, intrinsic, Fermi-level and valence band energy respectively. $q\Phi_s$ - semiconductor work function, $q\Phi_m$ - electrode work function, and $q\chi_s$ - semiconductor electron affinity. V_{SB} - surface barrier voltage, V_D - dielectric voltage and V_{CPD} - measured contact potential difference.

Strong illumination of the Si underneath the CPD probe flattens the surface barrier ($\Delta V_{SB} \to 0$) but does not affect ΔV_D. This effect is exploited to determine the flat-band condition at the Si-dielectric interface with each incremental corona dose as given by

$$\varDelta V_{SB} = V_{CPD}^{Dark} - V_{CPD}^{Light} \; . \tag{3.3}$$

It should be noted that $\varDelta V_{SB}$ is an important parameter that controls the surface recombination velocity of c-Si surface. When the surface is in accumulation $\varDelta V_{SB} = 0$, whereas in inversion $\varDelta V_{SB} > 0$. Considering the case of Al$_2$O$_3$ (negatively charged dielectric) on *p*-type c-Si, the initial state of the surface is in accumulation and $\varDelta V_{SB} = 0$. In this case, application of positive corona charge will drive the surface towards flat-band which is determined by $\varDelta V_{SB} > 0$. The amount of positive corona charge required to push the surface to flat-band conditions equals the total fixed charge Q_{tot} (in elementary charges per cm^2 or qcm^{-2}) in the dielectric, as demonstrated in Figure 3.4.
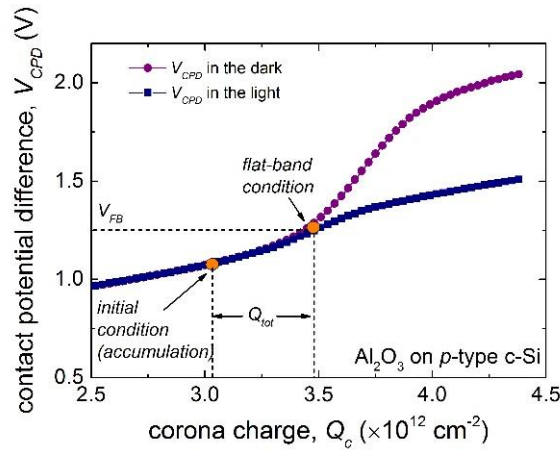
Figure 3.4 Measured contact potential difference V$_{CPD}$ as a function of corona charge Q$_c$ (in elementary charges per cm^2) illustrating the determination of flat-band voltage and Q$_{tot}$ for the case of Al$_2$O$_3$ on p-type c-Si (2 Ωcm).

The density of interface traps D_{it} (in eV^{-1}cm^{-2}) is calculated as the ratio of extracted interface trap charges to $\varDelta V_{SB}$. The D_{it} spectrum is then plotted as a function of $\varDelta V_{SB}$. D_{it} can be determined from flat-band conditions where $\varDelta V_{SB} = 0$ up to deep inversion where $\varDelta V_{SB} > 0$. $\varDelta V_{SB}$ is analogous to the position in the energy band-gap of c-Si from the valence band edge, E_v to the conduction band edge, E_c. From the Shockley-Read-Hall (SRH) statistics it is well know that the defect levels in the middle of the Si bandgap have the largest influence on carrier recombination [24, 29]. Hence, the D_{it}

value in the middle of the bandgap ($D_{it,midgap}$) is the value commonly reported. More details can be found in Refs. [132, 135, 136].
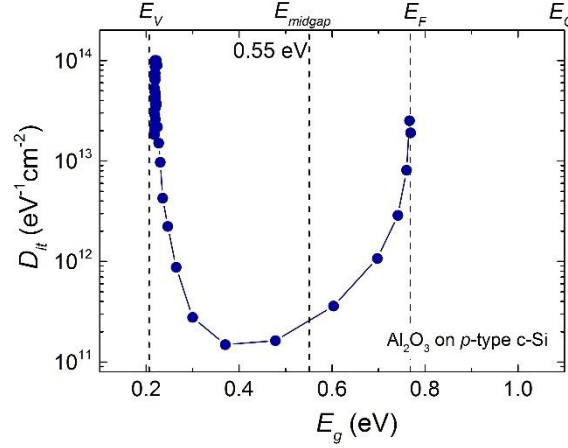
Figure 3.5 Density of interface states D_{it}, as a function of the band gap energy of silicon, E_g, for Al₂O₃ on a p-type c-Si (2 Ωcm).

3.2.3 Secondary ion mass spectrometry (SIMS)

Secondary ion mass spectrometry (SIMS) is a popular technique used to analyse the chemical composition of solid surfaces and thin films. It uses a focused primary ion beam to sputter the surface of a specimen and the secondary ions ejected from the surface are collected and analysed to identify the atomic mass of the atoms and molecules arriving at the detector. The elemental, isotopic or molecular composition of the sample surface up to a depth of 1-2 nm can be identified. A depth profile of a sample may be obtained simply by recording sequential SIMS spectra as the surface is gradually eroded away by the primary ion beam probe. In the SIMS technique, the detection limit for most trace elements is between 10^{12} and 10^{16} atoms/cm³ [137].

In this thesis, a time-of-flight or ToF-SIMS system was used for the surface analysis of fabricated Al₂O₃ layers. Known for its high sensitivity and high mass resolution, ToF-SIMS uses a pulsed primary ion beam to ionise surface atoms and molecules and the resulting secondary ions are accelerated into a mass spectrometer which determines

their mass by measuring the exact time of impact at the detector (i.e. "time-of-flight") on a scale of nano-seconds. A depth profile is obtained by measuring the mass spectra for each sputtered layer. The schematic of a ToF-SIMS setup is shown in Figure 3.6.
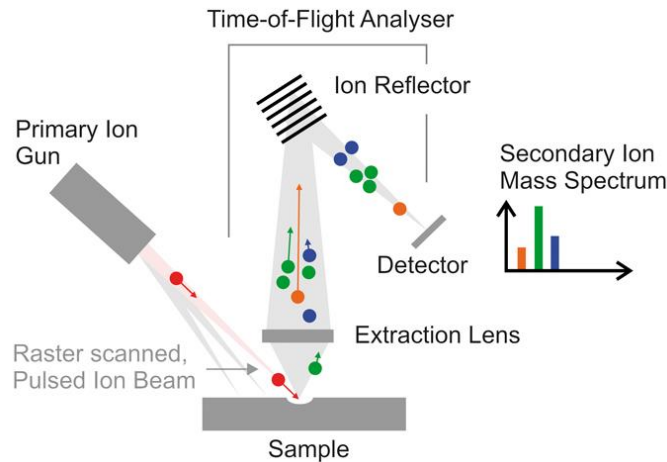
Figure 3.6 Schematic illustration of a time-of-flight secondary ion mass spectrometer (ToF-SIMS). Adapted from [138].

3.3 Comparison of Al$_2$O$_3$ films fabricated by solar-grade and semiconductor-grade TMA

Symmetric samples of large-area (156 mm × 156 mm) *n*-type (170 μm, 2.5 Ωcm) and *p*-type (170 μm, 1.5 Ωcm) <100>-oriented Cz silicon wafers were used as substrates. Before Al$_2$O$_3$ deposition, the saw damage of the wafers was removed using KOH solution and an RCA (Radio Corporation of America) clean was done without a final HF dip to preserve the thin chemical oxide layer formed during cleaning. The samples were then rinsed in deionised water and dried in gaseous nitrogen. Al$_2$O$_3$ films were deposited using SoLayTec's InPassionLAB ultrafast spatial ALD reactor, which has a throughput of ~100 wafers per hour (wph). Trimethylaluminium (TMA, AkzoNobel) and deionized water vapour (H$_2$O) were used as the ALD precursors. Nitrogen (N$_2$ > 99.999%, Air Liquide) was used as the carrier gas for both precursors and also as a gaseous separation curtain for the precursor gases in the reactor. All precursors were transported to the reactor through heated lines to prevent condensation. Both TMA and

H_2O were further heated to the deposition temperature in a heat exchanger before being injected into the reactor through slits. Each slit was flanked by exhaust channels that carry away excess gas on each side, with two adjacent slits sharing one exhaust. During deposition, the sample is supported by N_2 gas bearings from the top and bottom which keep the sample floating in the reactor throughout deposition. The sample was also moved steadily back and forth inside the reactor at a fixed wafer speed, using pulses of N_2 at both ends of the reactor. During each ALD cycle, the wafer was exposed to one TMA slit and two H_2O slits. The the TMA and H_2O precursor exposure (pulse) and purge durations were fixed at 10 ms in this experiment. The films were deposited using a TMA flow rate of 5 slm, a total H_2O flow rate of 10 slm and N_2 flow rates of 5 slm for each slit. These flow rates were adopted based on prior optimisation of the TMA partial pressures to ensure saturation of the Al_2O_3 ALD growth.

The typical temperature window in the spatial ALD system is from 100 to 250 °C. For the deposition of the Al_2O_3 films, a fixed temperature of 200 °C was chosen. Prior to the ALD process, the wafer is heated from room temperature to the deposition temperature in the run-in heating chamber in an inert N_2 atmosphere. In this study both solar-grade TMA and semiconductor (or 'semicon') grade were used as Al precursors. For each grade of TMA, Al_2O_3 films with thickness in the range of 4 – 12 nm were deposited on both *n*-type and *p*-type Cz-Si samples (five samples for each thickness). After Al_2O_3 deposition, all the samples were annealed at 425 °C in N_2 for 30 minutes to ensure the activation of the surface passivation.

The effective minority carrier lifetime (τ_{eff}) for each sample was measured by QSS-PC (WCT-120, Sinton Consulting), as detailed in Section 3.2.1. The system was operated in both the transient and quasi-steady-state mode for measurement over an injection level range from 1×10^{14} to 1×10^{17} cm^{-3} [139]. From the measured τ_{eff}, the effective surface recombination velocity was calculated using:

$$S_{eff} = \frac{W}{2}\left(\frac{1}{\tau_{eff}} + \frac{1}{\tau_{bulk}}\right) \tag{3.4}$$

where W is the wafer thickness and τ_{bulk} the minority carrier lifetime in the wafer bulk. For both n-type and p-type Cz-Si samples, τ_{bulk} was calculated using the empirical parameterization by Richter *et al.* to account for Auger recombination [31]. The upper limit of surface recombination velocity $S_{eff,max} = W/2\tau_{eff}$ is considered for the case of $\tau_{bulk} \rightarrow \infty$. The total charge density in the film (Q_{tot}) and the interface defect density at midgap ($D_{it,midgap}$) were determined by contactless corona-voltage (C-V) measurement using a commercial system (PV2000, Semilab SDI), as detailed in Section 3.2.2. The chemical composition of the Al₂O₃ films fabricated using solar- and semiconductor-grade TMA was analysed using a ToF-SIMS system (ToF-SIMS 4, IONTOF). The measurement was conducted in positive mode using an Ar gun for sputtering. The known Al₂O₃ film thickness was correlated to the point where the measured Al intensity reduced to half-maximum and the time scale was converted into depth using this point as the reference.

3.3.1 Evaluation of the effective minority carrier lifetime (τ_{eff})

As shown in Figure 3.7, Al₂O₃ films deposited using solar- and semicon-grade TMA resulted in high τ_{eff} on both p-type and n-type c-Si surfaces. On p-type Cz-Si, τ_{eff} values of 246 and 208 µs were obtained for solar- and semicon-grade Al₂O₃, respectively, at an injection level of 1×10^{15} cm^{-3}, which corresponds to S_{eff} values of 32 and 28 cm/s. It should be mentioned that τ_{eff} is very likely limited by bulk recombination for these Cz p-type wafers. On n-type Cz-Si, very high τ_{eff} of 4.6 and 2.8 ms corresponding to extremely low S_{eff} values of 1.1 and 2.3 cm/s were obtained at an injection level of 1×10^{15} cm^{-3} for samples passivated with both solar- and semicon-grade grown Al₂O₃ films, respectively. The slightly better performance of solar-grade TMA shows that its

higher concentration of impurities does not seem to degrade the surface passivation properties of Al_2O_3 films.
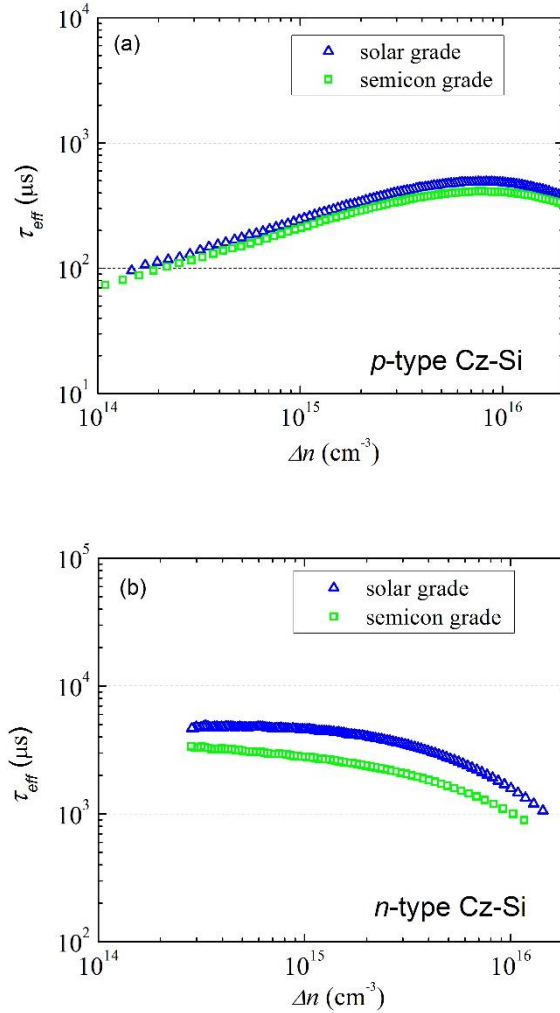
Figure 3.7 Effective carrier lifetime τ$_{eff}$ as a function of excess carrier density Δn, for 6 nm thick Al₂O₃ films deposited using solar- and semiconductor-grade TMA as precursors on 2.8 Ωcm (a) p-type and (b) n-type Cz-Si.

Recombination losses at a semiconductor interface or surface can be reduced by two different passivation mechanisms as discussed in Section 2.2.2. The first is by the chemical passivation of the interface and surface defect states. The D_{it} at the Si surface can be reduced significantly by the passivation of the uncoordinated atoms or the dangling bonds, for example, by atomic hydrogen. The second mechanism for surface passivation is a reduction in the electron or hole concentration near the semiconductor

surface by the use of a built-in electrical field which is known as field-effect passivation. Since recombination processes require both electrons and holes, the highest recombination rate occurs when the electron and hole concentrations at the interface or surface are comparable in magnitude. The recombination rate scales with the minority carrier concentration at the surface. Field effect passivation originates from an internal electric field at the interface or silicon surface that causes electrostatic shielding of the charge carriers and alters the electron or hole concentration near the interface. This internal field is either obtained by a doping profile below the interface or by the presence of fixed electrical charges near the interface (Q_{tot}). We investigate the role of both chemical and field effect passivation mechanisms at the Si/Al₂O₃ interface by comparing the $D_{it,midgap}$ and Q_{tot} for films deposited using solar-grade and semicon grade TMA.

3.3.2   Evaluation of the interface defect density ($D_{it,midgap}$)

The average $D_{it,midgap}$ at each thickness of Al₂O₃, determined from measurements on all five samples in each sample set is shown in Figure 3.8. It is observed that for both solar- and semicon-grade TMA grown Al₂O₃ films, quite low $D_{it,midgap}$ values around 1×10^{11} cm^{-2}eV^{-1} were obtained at the *p*-type and *n*-type Si/Al₂O₃ interface. Further, on both *p*-type and *n*-type Cz-Si, $D_{it,midgap}$ values were consistently lower for solar-grade TMA samples as compared to semicon-grade TMA samples. The reason for this improved interface quality is still under investigation. The difference in $D_{it,midgap}$ for solar- and semicon-grade explains the slightly higher τ_{eff} values (and lower S_{eff} values) of the solar-grade Al₂O₃ films that is observed for all measured samples in each set.
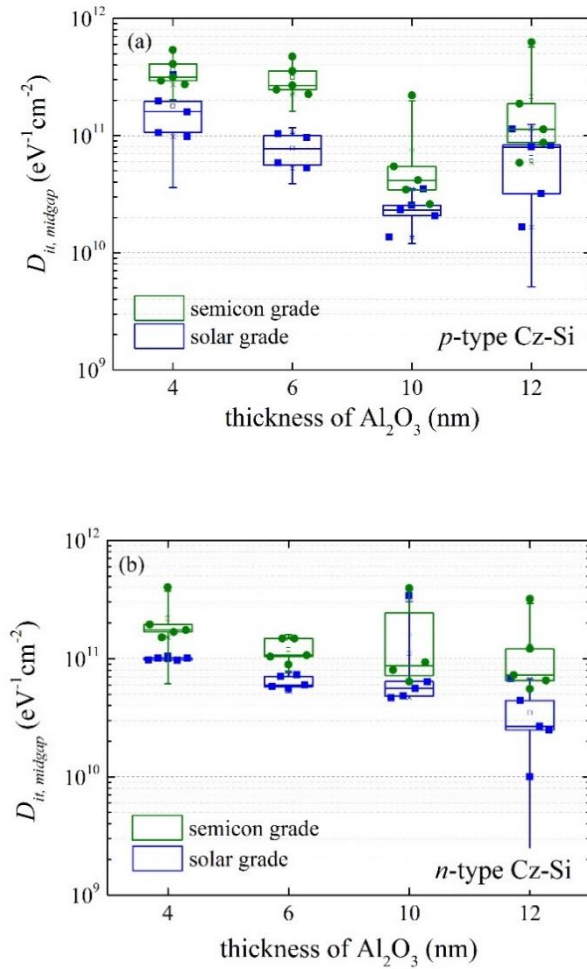
Figure 3.8 Interface defect density $D_{it,midgap}$ as a function of Al_2O_3 film thickness on (a) p-type and (b) n-type Cz-Si deposited using solar- and semicon-grade TMA.

The higher $D_{it,midgap}$ observed for the 4 nm thick films could be due to the relatively poorer interface quality for ultrathin layers. It can be seen that a relatively low $D_{it,midgap}$ is obtained for the 10 nm films on *p*-type and *n*-type substrates, indicating that this could be the optimum thickness for Al_2O_3 films deposited by the spatial ALD reactor. The lower $D_{it,midgap}$ for all solar-grade samples signifies improved chemical passivation of the silicon interface. This is an important advantage for solar-grade TMA over the more expensive semicon-grade TMA.

3.3.3   Evaluation of the total charge density (Q_{tot})

As shown in Figure 3.9, all samples show high negative Q_{tot} values ranging from -3×10^{12} cm^{-2} to -1×10^{13} cm^{-2}. For the Al₂O₃ films deposited on *p*-type substrates, the Q_{tot} is seen to be largely similar for thicknesses of 4 and 10 nm while the solar-grade samples show a higher Q_{tot} for 6 nm and 12 nm thick Al₂O₃ films. On the other hand, for Al₂O₃ films on *n*-type substrates, the semicon-grade samples outperform the solar-grade samples across all thicknesses. However, the difference between the Q_{tot} values for solar- and semicon-grade are not deemed to be significant enough to influence a large difference in the passivation properties. Hence, the field-effect passivation is similar for solar-grade and semicon-grade Al₂O₃ films. Q_{tot} values are seen to decrease slightly with increasing film thickness on both *p*-type and *n*-type Cz-Si substrates. This is consistent with earlier reports of D_{it} and Q_{tot} for varying film thicknesses [140].
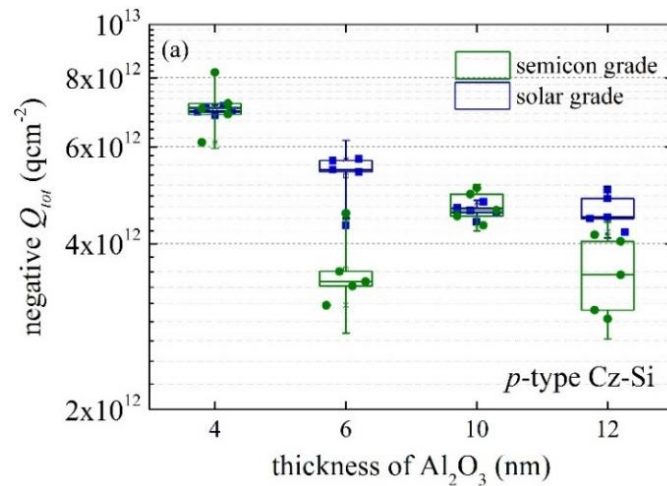
Figure 3.9 (a) Total charge density Q_{tot} as a function of the Al₂O₃ film thickness on p-type Cz-Si deposited using solar- and semiconductor-grade TMA.
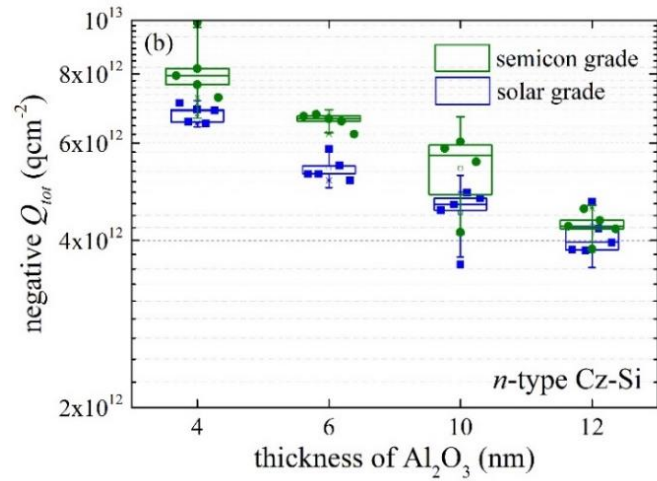
Figure 3.9 (b) Total charge density Q_{tot} as a function of the Al_2O_3 film thickness on n-type Cz-Si deposited using solar- and semiconductor-grade TMA.

3.3.4   Evaluation of chemical composition of the Al_2O_3 films

The chemical composition of Al_2O_3 films fabricated using semicon- and solar-grade TMA as measured by SIMS is shown in Figure 3.10. The aim of this measurement was to identify possible differences in impurity content for Al_2O_3 films prepared by the two grades of TMA.
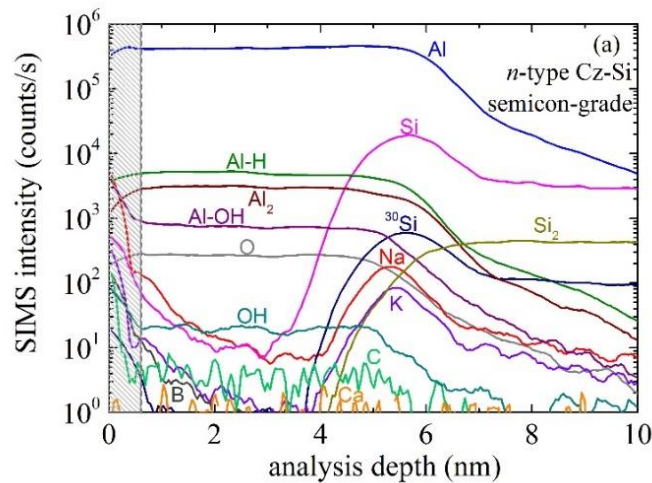
Figure 3.10 (a) SIMS depth profile of 6 nm Al_2O_3 fabricated using semiconductor-grade TMA on n-type Cz-Si as function of sputtered depth during measurement.
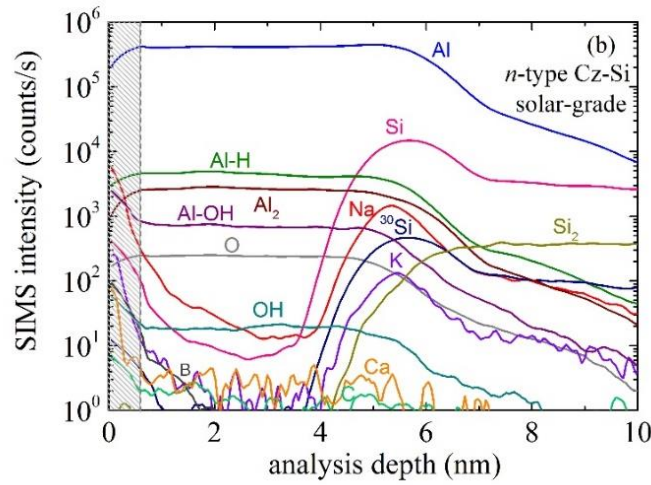
Figure 3.10 (b) SIMS depth profile of 6 nm Al₂O₃ fabricated using solar-grade TMA on n-type Cz-Si as function of sputtered depth during measurement. Al₂ and Si₂ represent the diatoms of Al and Si respectively, while ³⁰Si represents an isotope of Si. Al-H and Al-OH represent secondary molecules ejected during measurement. The first 0.6 nm of the depth profile represent the contaminated top surface layers of the films.

A number of alkaline impurity peaks (e.g. Na, K, Ca) were identified in both films from the mass spectra. On the other hand, heavy metals that are more likely to degrade the passivation quality of the films (e.g. Fe, Ni, Cu, Zn) were not detected. The chemical composition of the solar-grade and semicon-grade samples are seen to be very similar with respect to the Al, Si, and O content. However, a small difference in the Na and K content is observed with solar-grade sample indicating a higher peak alkaline impurity content (Na ~1400 and K ~130 counts/s) as compared to the semicon-grade sample (Na ~170 and K ~85 counts/s). This result is consistent with the knowledge that semicon-grade TMA has a higher purity than solar-grade TMA. Since alkaline impurities are not expected to degrade passivation qualities significantly, the higher impurity content does not affect the passivation quality of Al₂O₃ films fabricated with solar-grade TMA as is observed from the effective carrier lifetime and interface properties of the films.

3.4   Chapter Summary

A comparative study of Al_2O_3 films deposited using solar- and semiconductor-grade TMA as precursors in an inline high-rate spatial ALD reactor gave very high effective minority carrier lifetimes and ultralow surface recombination velocities when deposited on Cz-Si substrates. Detailed investigations showed that the c-Si/Al_2O_3 interface defect quality of the solar-grade samples is, in fact, better than that of the semiconductor-grade samples while the total charge density was almost the same for both. A slightly higher alkaline impurity content was observed in the solar-grade samples which does not influence the passivation quality significantly. Hence, this study shows that Al_2O_3 films deposited using low-cost solar-grade TMA demonstrate surface passivation properties comparable to those deposited using higher-cost semiconductor-grade TMA. This statement applies to both *n*-type and *p*-type Cz-Si surface passivation. This makes solar-grade TMA an ideal choice for surface passivation of *n*-type and *p*-type Si surfaces by Al_2O_3 in the industry.

Chapter 4: Undoped ZnO films deposited by spatial ALD[1]

4.1   Introduction

As briefly discussed in Chapter 2, undoped or intrinsic zinc oxide (*i*-ZnO) is a wide-bandgap semiconductor with a variety of useful properties that have made it a material of increasing attention in numerous fields of research [88]. The high transparency of ZnO in the visible wavelength range combined with its tunable electrical conductivity enables its use in devices such as transparent electronics [141], gas sensors [142] and solar cells [85]. ZnO has a direct bandgap of 3.37 eV at room temperature [114]. Thin films of ZnO are used in the photovoltaic (PV) industry in the undoped, as well as doped form, for example in record-efficiency $Cu(In,Ga)Se_2$ (CIGS) thin film solar cells and in silicon heterojunction solar cells [143-145]. In a standard CIGS configuration, a ZnO bilayer is used, consisting of a resistive *i*-ZnO layer capped with a doped ZnO layer. This thin *i*-ZnO layer has been an integral component of CIGS solar cells over the years because it has consistently shown to improve the reproducibility and production yield for this type of solar cell [85]. This improvement is attributed to the role of resistive *i*-ZnO in preventing the formation of shunts between the highly doped ZnO front contact and the molybdenum rear contact through pinholes and crevices in the inhomogeneous absorber layer [146]. The presence of the resistive *i*-ZnO layer

---

[1] Parts of this chapter have been published in the following papers:

N. Nandakumar, B. Dielissen, D. Garcia-Alonso, Z. Liu, R. Görtzen, W. M. M. Kessels, A. G. Aberle and B. Hoex, "Resistive intrinsic ZnO films deposited by ultrafast spatial ALD for PV applications", *IEEE Journal of Photovoltaics*, vol. 5, no. 5, pp. 1462-1469, 2015.

N. Nandakumar, B. Dielissen, D. Garcia-Alonso, Z. Liu, R. Görtzen, W. M. M. Kessels, A. G. Aberle and B. Hoex, "Spatial atomic layer deposition of intrinsic zinc oxide films for applications in the photovoltaic industry", *Technical digest of the 6th World Conference on Photovoltaic Energy Conversion (6th WCPEC), Japan,* pp. 573-574, 2014.

results in higher resistive losses and increased carrier recombination at the buffer/absorber interface due to an increased separation between the Fermi level and the conduction band of the absorber as illustrated in Figure 4.1 [147]. However, numerical modelling and experimental studies have shown that this high series resistance provided by the *i*-ZnO layer prevents spatial electrical inhomogeneity (*e.g.* low-performance areas of locally enhanced recombination) from dominating the open-circuit voltage of the entire device [147-149]. This explains the high solar cell efficiencies obtained even when ~100 nm *i*-ZnO layers are used [150].
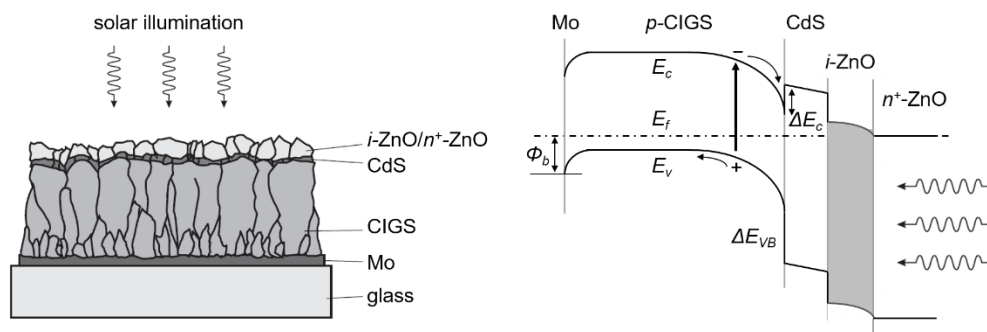
Figure 4.1 Schematic illustration of the structure and energy band diagram of a Cu(In,Ga)Se₂ or CIGS thin-film solar cell. The ZnO window layer typically consists of a combination of a nominally undoped ZnO and a highly doped ZnO layer. E_c, E_f and E_v are the conduction band, Fermi-level and valence band energies, respectively. Φ_b denotes energy barrier for electrons and holes to the metal contact. Adapted from Refs [85, 147, 151].

The preferred deposition technique for *i*-ZnO films in the PV industry is direct current and reactive sputtering from ceramic and metal targets, respectively [85]. However, sputtering of *i*-ZnO films has been shown to cause significant surface damage to the underlying absorber layer due to highly energetic ions and other plasma induced effects [113, 152]. Consequently, there is a need for a low-damage technique for the deposition of the *i*-ZnO layer.

ALD is one such deposition technique. As introduced in Chapter 2, Section 2.4.4, ALD offers uniform growth and precise thickness control in addition to low surface damage

due to its self-limiting chemical reactions at low substrate temperatures. The limitations of temporal ALD are overcome by the spatial ALD technique (see Section 2.5.1) [105]. In spatial ALD, a moving substrate is sequentially exposed to each precursors as illustrated in Figure 4.2, removing the requirement for the lengthy pumping cycles between each exposure. This combines the advantages of conventional ALD (i.e. the growth of uniform, pinhole-free and highly conformal films on large-area substrates) with high deposition rates, making it an attractive option for the deposition of ZnO in the PV industry.

In 2011, Illiberi *et al.* demonstrated the deposition of *i*-ZnO films by spatial ALD on a prototype lab-scale system consisting of a circular reactor head with inlets for each precursor [93]. The substrate was placed on a circular table that rotated underneath the reactor head. In this chapter, the deposition of *i*-ZnO has been successfully scaled up using a commercial spatial ALD system currently employed in the PV industry. Highly uniform *i*-ZnO films with precisely controlled thickness, high transparency (> 90 % in the visible wavelength range), and exceptionally high resistivity (~100 Ω-cm) were deposited at growth rates up to ~35 nm/min at low deposition temperatures (< 250 $^{\circ}$C) and atmospheric pressure. We investigate the properties of the *i*-ZnO films in detail and study the influence of the short exposure and purge durations of spatial ALD on the electrical and structural properties of *i*-ZnO.

4.2 Fabrication of undoped *i*-ZnO films by spatial atomic layer deposition

In this work, *i*-ZnO films were deposited using SoLayTec's InPassion LAB spatial ALD system. A schematic of the system is shown in Figure 4.2. Diethyl zinc (DEZn SSG, AkzoNobel) and deionized water vapour (H_2O) were used as the ALD precursors. Nitrogen (N_2 > 99.999%, Air Liquide) was used as the carrier gas for both precursors and also as a gaseous separation curtain for the precursor gases in the reactor. All precursors were transported to the reactor through heated lines to prevent condensation.

Both DEZ and H_2O were further heated to the deposition temperature in a heat exchanger before being injected into the reactor through slits. Each slit was flanked by exhaust channels that carry away excess gas on each side, with two adjacent slits sharing one exhaust as shown in Figure 4.2. During deposition, the sample was supported by N_2 gas bearings from the top and bottom which keep the sample floating in the reactor throughout deposition. The sample was also moved steadily back and forth inside the reactor at a fixed wafer speed, using pulses of N_2 at both ends of the reactor. During each pass the wafer was exposed to one DEZ slit and two H_2O slits for each ALD cycle. Hence, the DEZ and H_2O precursor exposure (pulse) and purge durations were fixed for a certain wafer speed in this experiment. Unlike in temporal ALD, the pulse for each reactant and the purge time in between pulses cannot be independently varied.
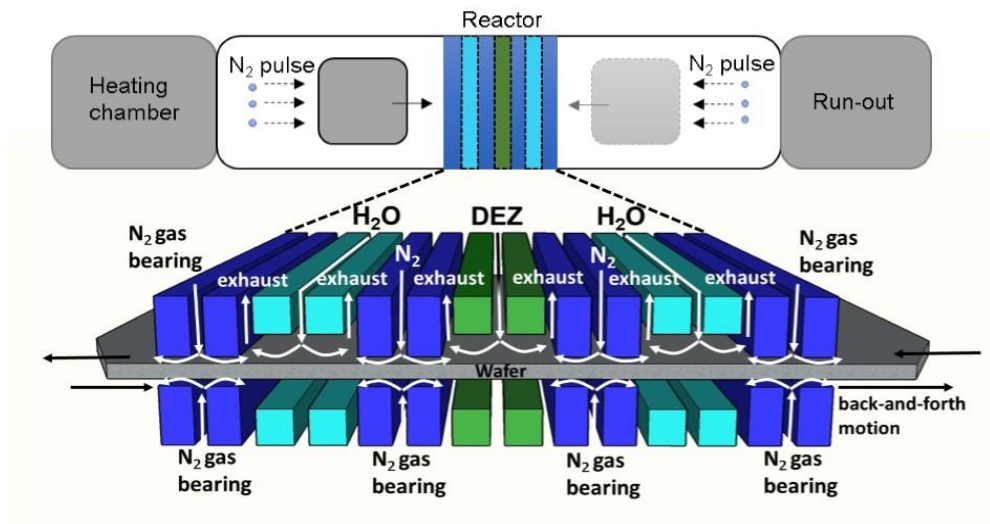
Figure 4.2 Schematic illustration of the working principle of spatial ALD. The gaseous precursors (DEZ and H2O) are separated in space rather than in time as in the case of temporal ALD. The substrate is moved back and forth by N2 pulses on either side of the reactor. Each pass results in one ALD cycle.

Typical DEZ-based *i*-ZnO deposition temperatures for ALD range from 100 to 250 °C [153]. In the present work, this same temperature range was used for the reactor and

precursor gases. Prior to the ALD process, the wafer is heated from room temperature to the deposition temperature in the run-in heating chamber and in an inert N_2 atmosphere.

i-ZnO films were deposited on pseudo-square 125 mm × 125 mm p-type Cz c-Si substrates with a (100) crystal orientation. However, 156 mm × 156 mm wafers can also be easily processed in the same system. All substrates were cleaned using a standard Radio Corporation of America (RCA) clean [154], followed by a dip in 1 % hydrofluoric (HF) acid with a final rinse in water before drying. To enable spectroscopic ellipsometry (SE) measurements, the films were deposited on single-side polished c-Si substrates. The SE substrates were prepared by chemical-mechanical polishing (CMP), resulting in a surface roughness of less than 5 Å. For electrical measurements, the films were deposited on as-procured polished c-Si samples with a 150 nm insulating layer of thermally grown SiO_2.

The thickness and optical properties of all films were measured using a spectroscopic ellipsometer (J.A. Woollam, M2000) in the visible and near-infrared (NIR) wavelength range from 250 to 1700 nm at 65°, 70° and 75°. The 'pSemi-M0 oscillator model' was used to model the dielectric function of the ZnO film [155]. The refractive indices (n) and extinction coefficients (k) obtained from the ellipsometry measurements were used to simulate transmission and absorption spectra of the i-ZnO films for a typical CIGS solar cell structure, using the transfer matrix method in Mathematica$^{©}$. The n and k values of magnesium fluoride (MgF_2), cadmium sulphide (CdS) and CIGS were obtained from the literature [156-158], while those of Al-doped ZnO ('AZO') were measured in-house. Electrical properties were measured using a four-point probe mapping system (4PP, Advanced Instrument Technology, CMT-SR2000N-PV). The structural characterization of the films was done by scanning electron microscopy (SEM, Carl Zeiss, Auriga) and X-ray diffraction (XRD, PANalytical, X'Pert Pro MRD). X-ray photoelectron spectroscopy (XPS, Thermo Scientific K-Alpha, KA1066)

with monochromatic Al K_α X-ray radiation (hv = 1486.6 eV, spot size = 400 µm) was used to assess the chemical composition of the films. All samples were corrected for sample charging with a flood gun. The sensitivity factors used for quantification were calibrated with Rutherford backscattering spectrometry as reported elsewhere [159]. For depth profiling, an Ar gun was applied to sputter the *i*-ZnO films. The details of the characterisation techniques used are provided in the Appendix.

4.3   Film growth characteristics

DEZ and H_2O used for ALD of *i*-ZnO react as follows:

$$s\text{-Zn}(CH_2CH_3)_2 \text{ (g)} + H_2O \text{ (g)} \rightarrow s\text{-ZnO (s)} + 2C_2H_6 \text{ (g)} \qquad (4.1)$$
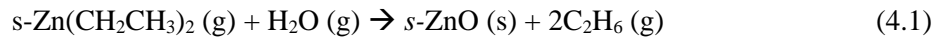
where *s*- denotes surface species. The above reaction can be split further into two self-limiting half-reactions that occur on exposure to each precursor [160]:

$$s\text{-Zn-OH} + Zn(CH_2CH_3)_2 \rightarrow s\text{-Zn-O-Zn}(CH_2CH_3) + C_2H_6 \qquad (4.2)$$

$$s\text{-Zn-}(CH_2CH_3) + H_2O \rightarrow s\text{-Zn-OH} + C_2H_6 \qquad (4.3)$$
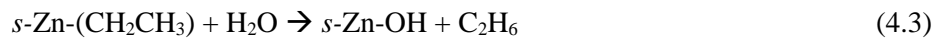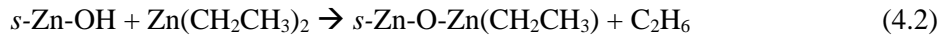
The reaction of DEZ with H_2O is exothermic and can be used to deposit *i*-ZnO thin films at substrate temperatures much lower than are required for other processes with different precursors. In Figure 4.3(a), the relation between film thickness and the number of ALD cycles is shown for an *i*-ZnO film deposited at a substrate temperature of 225 °C. It can be seen that the film thickness increases linearly with the number of ALD cycles, as is expected for an ALD process. The linear fit of the data in Figure 4.3(a) indicates a short nucleation delay, which is quite typical for ALD of *i*-ZnO. The increase in thickness was linear after this initial lag. From the slope of the line, the growth per cycle (GPC) was found to be ~0.19 nm/cycle for a DEZ partial pressure of 2 mbar, an H_2O partial pressure of 65 mbar and a pulse and purge time of ~8 ms each.

This GPC value was found to correlate well with the interplanar distances in a hexagonal unit cell of *i*-ZnO, which range from 0.25 nm for the (101) planes to 0.26 nm and 0.28 nm for the (002) and (100) planes, respectively. This indicates that the *i*-ZnO GPC was very close to ideal monolayer growth values [161] and is consistent with existing reports of *i*-ZnO GPC values by temporal ALD as well as spatial ALD in this deposition temperature range [93, 114]. Each cycle takes ~0.3 s, resulting in a deposition rate of ~35 nm/min for a GPC of 0.19 nm/cycle clearly illustrating that spatial ALD is capable of deposition rates rivalling conventional PECVD.
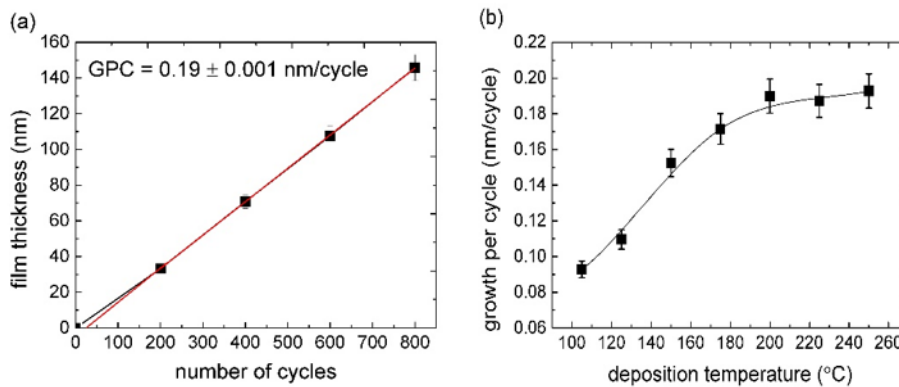
Figure 4.3 (a) Film thickness as a function of the number of ALD cycles at a deposition temperature of 225 ºC. Growth per cycle (GPC) was determined from the slope of the curve determined from a linear fit of the measured data. (b) GPC as a function of deposition temperature for a DEZ partial pressure of 2 mbar, a water partial pressure of 17 mbar, and a pulse and purge time of ~8 ms each.

The reported optimum ALD temperature window and the temperature at which growth saturation for *i*-ZnO is achieved vary greatly [114]. It is likely that reactor design and other factors such as the position of temperature sensors, reactor shape and reactor size influence the values reported for ALD temperature windows. A temperature range from 100 to 250 °C was chosen in this work. Figure 4.3(b) illustrates the growth per cycle of *i*-ZnO films as a function of the substrate temperature. Maximum GPC for *i*-ZnO growth was achieved at 200 °C, after which the GPC remained constant at ~0.19 nm/cycle. The DEZ and H_2O partial pressures were optimised in previous work to identify the precursor saturation regime [15]. Another point worthy to note is that some

studies show a drop in the GPC of ALD deposited *i*-ZnO for substrate temperatures above 175 °C [162, 163]. This is attributed to "precursor desorption" or specifically to the decrease in hydroxyls at the surface at higher temperatures. A detailed study by Nelson *et al.* showed that this desorption is influenced by the purge time, whereby longer purge cycles result in a decreased GPC [164]. In comparison, spatial ALD offers the advantage of very short purge durations, maintaining a high GPC even at higher deposition temperatures.
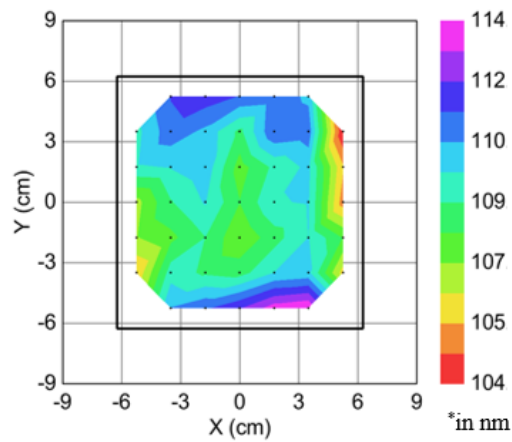
Figure 4.4 Spatially resolved thickness (in nm) of i-ZnO films deposited at a substrate temperature of 225 ºC on a 125 mm × 125 mm c-Si substrate. The i-ZnO thickness was measured at 45 points on the sample using spectroscopic ellipsometry.

The spatially resolved thickness was measured on a polished 125 mm × 125 mm c-Si wafer and is presented in Figure 4.4. The thickness non-uniformity across the wafer was calculated using the following formula:

$$Non-uniformity = \frac{d_{max} - d_{min}}{2d_{avg}} \times 100 \tag{4.4}$$

where d_{max}, d_{min}, and d_{avg} are the maximum, minimum, and average thicknesses, respectively. With this formula, the average non-uniformity value for a 100 nm thick *i*-ZnO film was ~3.5 %. This value is ~1 % lower than the film non-uniformity values reported in the literature for *i*-ZnO films deposited by temporal ALD [165]. By virtue of its self-saturating nature, ALD films should have high uniformity; nevertheless, non-

uniformity in the thickness of ALD films have been consistently observed, reported
and studied [165] which can e.g. be the result of precursor injection and/or flows.

4.4   Optical and structural properties

Along with film thickness, the SE measurements were also used to extract *n* and *k*
values of the *i*-ZnO films. Figure 4.5 shows the *n* and *k* values as a function of photon
energy for *i*-ZnO films (600 cycles) grown at different deposition temperatures. The
film thicknesses vary with temperature due to the temperature dependence of the GPC.
The measured dielectric functions are in close agreement with spectra reported in the
literature for *i*-ZnO films [166, 167].
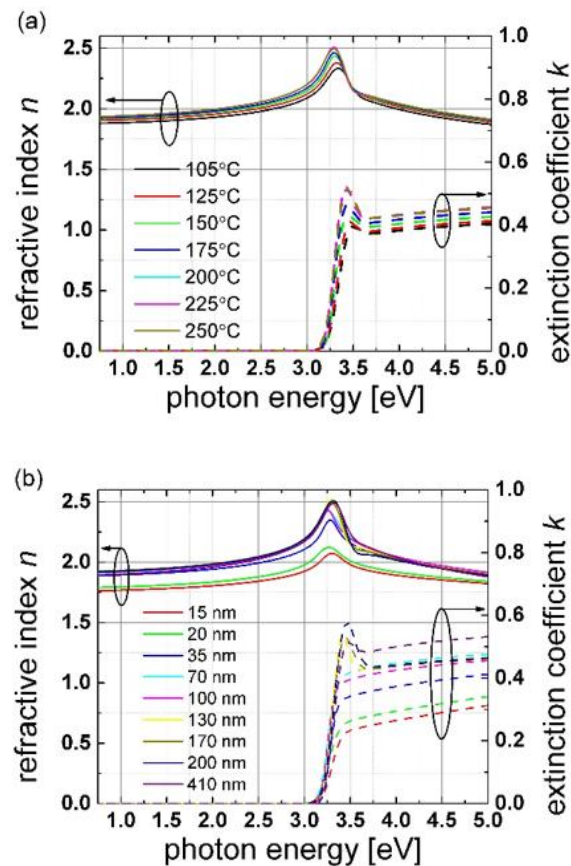
*Figure 4.5 Refractive index (n) and extinction coefficient (k) as a function of photon
energy of i-ZnO films deposited (a) at various temperatures and (b) with various
thicknesses using a fixed deposition temperature of 230°C.*

The refractive index of the deposited *i*-ZnO films was found to be between 1.8 and 2.0 at a wavelength of 632 nm, which is consistent with most reports in the literature [93]. The refractive index shows a peak at the bandgap energy, as shown in Figure 4.5(a). A shift the peak refractive index is observed with increasing deposition temperature. This shift can be attributed to a change in the film quality with increasing deposition temperature. The absorption edge of the *k* spectra was found to be at ~3.3 eV, which corresponds closely to the *i*-ZnO bandgap. However, a distinct peak is observed at ~3.4 eV which is attributed to excitonic energies in wurtzite ZnO [168, 169]. The excitonic interaction of electrons and holes has a strong influence on the absorption spectrum, preventing the accurate determination of the bandgap value by extrapolation of the absorption edge. On the other hand, the presence of the excitonic peak indicates that the *i*-ZnO film is polycrystalline with possibly large crystal grains, indicating good film quality. In Figure 4.5(b), the shift in the *n*-spectra and the absence of the excitonic peak in the *k*-spectra for films with thickness of ≤ 100 nm could indicate that the thinner films are not completely developed in terms of crystallinity. However, the presence of the excitonic peak for higher thicknesses clearly indicates a high crystalline content in the *i*-ZnO films. Structural investigations using SEM presented below for different *i*-ZnO thicknesses further support these observations.

The *n* and *k* values of *i*-ZnO deposited by spatial ALD obtained from SE measurements were further used to simulate the reflection, transmission and absorption spectra for relevant interfaces in a CIGS solar cell structure with an *i*-ZnO layer between the Al-doped ZnO front contact and the CdS buffer layer, as shown in Figure 4.6. The simulated spectra are shown for an 80 nm thick *i*-ZnO film deposited at 230 °C. The *i*-ZnO film shows very low absorption (A_{iZnO}) at wavelengths above 400 nm. Hence, it gives high transmission to the CIGS absorber (T_{CIGS}) of > 90 % in the visible and near-infrared wavelength ranges, which makes the developed *i*-ZnO films well-suited for application as transparent window layers.
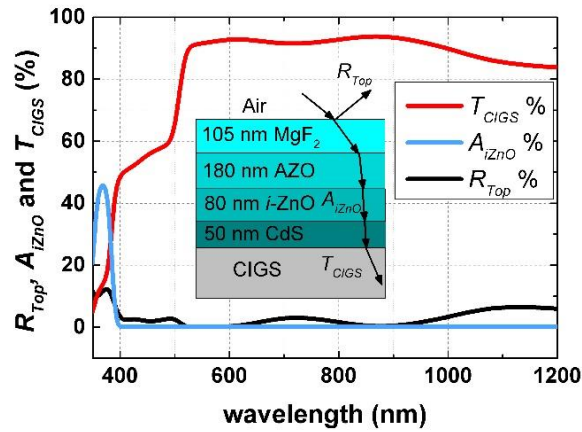
Figure 4.6 Simulated reflection from the top surface (R_{Top}), absorption in the i-ZnO layer (A_{iZnO}) and transmission to the CIGS absorber (T_{CIGS}) for i-ZnO films applied as the window layer in a CIGS solar cell structure. Inset: Illustration of the CIGS cell structure and interfaces used for the simulation.
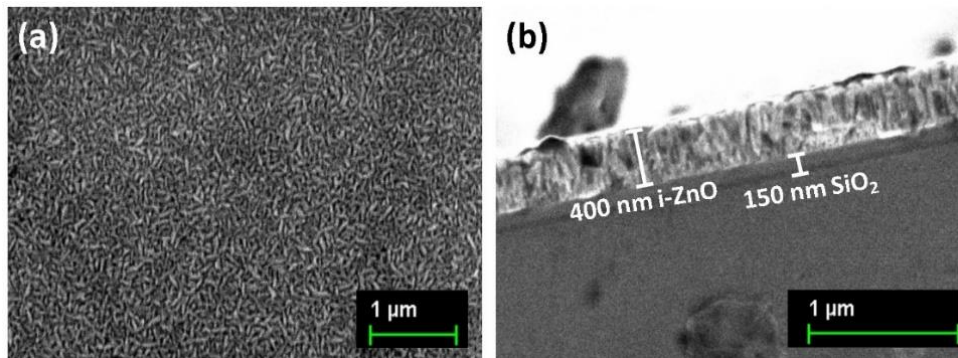
Figure 4.7 (a) SEM micrograph (plan view) of a 400 nm thick i-ZnO film deposited by spatial ALD on a c-Si/SiO$_2$ substrate. (b) SEM micrograph (cross-section) of the sample of graph (a), showing a columnar grain structure.

Figure 4.7 shows SEM images of the top surface and cross-section of a thick (400 nm) i-ZnO film on a SiO$_2$ covered c-Si wafer. Columnar crystal grains with a grain size of the order of 50 nm can be seen. The columnar crystal structure was not observable for very thin i-ZnO films of < 50 nm thickness. We believe that thin i-ZnO films do not have columnar grains, although it needs to be mentioned that clear SEM images were difficult to obtain for such samples due to their high resistivity, which resulted in electron charging. The large crystalline grains observed for the thicker i-ZnO films

confirm their highly polycrystalline nature. This also corresponds well with the observations from the *n* and *k* spectra in Figure 4.5.

4.5   Electrical properties

i-ZnO films are intrinsically *n*-type and are frequently found to be highly conductive, with resistivity values as low as 10^{-3} Ωcm being reported for as-grown *i*-ZnO without any additional doping, as summarised in Table 4.1.

Table 4.1 Properties of intrinsic ZnO films fabricated by various techniques

Deposition technique	Deposition temperature (°C)	Resistivity (Ωcm)	Comments	Ref.
PECVD	250	3×10^{-3}	UV exposure ~ 1 min	[41]
PLD	200	$(4-7) \times 10^{-3}$		[42]
Sputtering	60-120	$\sim 4 \times 10^{-1}$		[43]
MOCVD	620	42.7		[44]
Spray Pyrolysis	180	10^{-3}	Annealed in N_2 at 400 °C	[45-46]
Sol-Gel	80	28.2	Annealed in air at 500-600°C	[47]
Temporal ALD	200-220	$\sim 1 \times 10^{-3}$	Exposure ~1 s, Purge ~10 s	[5]
Spatial ALD-prototype	75-250	4×10^{-3}	Exposure ~30ms Purge ~0.3 s	[17]
This work	200-225	~100-200	Exposure ~8 ms Purge ~8 ms	

*PECVD = Plasma-Enhanced Chemical Vapor Deposition, PLD = Pulsed Laser Deposition, MOCVD = Metal-organic Chemical Vapor Deposition, ALD = Atomic Layer Deposition.

In contrast, the *i*-ZnO films deposited in this study all showed very high sheet resistances of the order of $10^7 - 10^8$ Ω/sq for 100-nm films, corresponding to a film resistivity in the range of 100–200 Ωcm, see Figure 4.8. Nelson *et al.* [164] recently showed that the resistivity of *i*-ZnO films exponentially increases with decreasing purge time after the DEZ exposure. They reported sheet resistance values of $\sim 10^5$ Ω/sq. for a 100 nm thick *i*-ZnO film deposited with pulse and purge times of 80 ms.

Specifically, their study showed that for a fixed exposure time (2 s) the DEZ purge time influences the resistivity much more than the H_2O purge time.
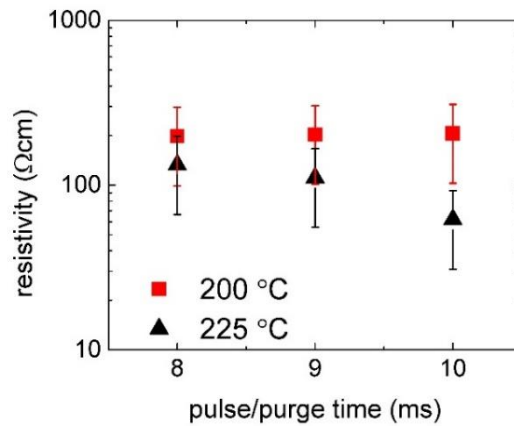
Figure 4.8 Film resistivity as a function of pulse and purge duration (ms) for 100 nm thick ZnO films deposited at 200 and 225 °C.

Here it is worthy to note that the exposure and purge cycles for this spatial ALD are asymmetric, in contrast to conventional temporal ALD. The details of the spatial ALD process used in this work are shown in Figure 4.9. Unlike in temporal ALD (where a sample is exposed to consecutive H_2O-purge-DEZ-purge-H_2O-purge-DEZ cycles), in spatial ALD the sample experiences two H_2O exposures after each DEZ exposure. The DEZ/H_2O exposure times (for a constant wafer speed) are each only ~8 ms. The purge times between the H_2O and the DEZ exposures is also ~8 ms during each wafer pass. Upon completion of one pass, the wafer is pushed back by a pulse of N_2 (as seen in Figure 4.2) and this results in a longer N_2 purge followed by another H_2O exposure.
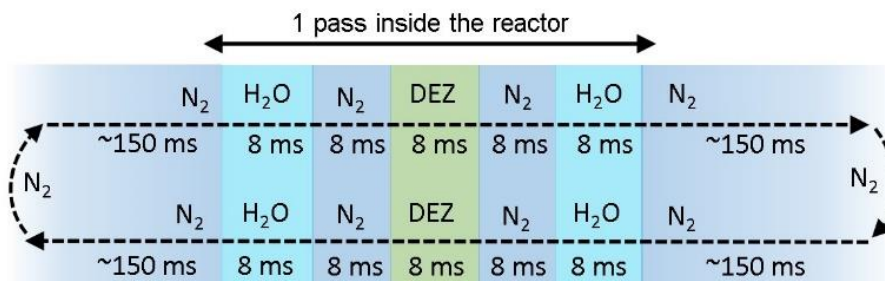
Figure 4.9 Schematic highlighting the DEZ and H_2O pulse and purge durations experienced by the substrate during one back-and-forth motion for the spatial ALD technique used in this study.

As mentioned earlier, Nelson *et al.* also showed that longer purge times result in lower growth rates, most likely due to desorption of the hydroxyl (OH) groups. If this was the case, the 300 ms long purge in our system would result in higher desorption of (OH) groups from the surface. However, the subsequent second H_2O exposure refreshes the surface with (OH) groups followed by only a short ~8 ms N_2 purge that prevents any further desorption.

Keeping this in mind, the high resistivity of the *i*-ZnO films deposited in this study is easily explained by the results of Nelson *et alia*. The DEZ pulse/purge time in our spatial ALD system was ~8 ms, much shorter than the 80 ms used in Nelson's work [164]. This also explains the high resistivities obtained by spatial ALD compared to temporal ALD where the exposure and purge durations are of the order of ~1 s and ~10 s, respectively. On the other hand, Illiberi *et al.* reported a resistivity of $4{\times}10^{-3}$ Ωcm for *i*-ZnO films that were deposited by spatial ALD. This low resistivity value can be explained by noting that in their spatial ALD setup the DEZ/H_2O exposure time is ~30 ms and the purge time is ~0.3 s, both significantly longer than the time durations used in this study. From an industrial point of view, it should also be noted that longer pulse/purge durations would result in lower deposition rates; hence, shorter pulse/purge durations are more desirable for high volume manufacturing.

The additional carriers in low resistive *i*-ZnO films are often associated with defects due to oxygen vacancies while higher oxygen content and oxygen interstitials are associated with high resistivity [85, 114, 163, 170, 171]. The observations in this study fit this line of thinking very well. With shorter exposure/purge times it is expected that the O atoms have a lower probability to desorb from the surface, resulting in fewer oxygen vacancies and hence a lower defect density, which corresponds to a higher resistivity. This is further supported by the lower resistivity obtained for films deposited at 225 °C as compared to those deposited at 200 °C. It is expected that higher temperature also results in higher densities of vacancies and defects.

4.6 Material properties

In Figure 4.10, the atomic percentage (at%) of oxygen, zinc, silicon and carbon as obtained from the XPS depth profiles are presented for an *i*-ZnO film deposited at 225°C. First, no carbon contamination was detected in the bulk of the film. Second, the relative at% of O is seen to be comparable to that of Zn indicating that the *i*-ZnO films are nearly stoichiometric. This agrees well with earlier reports for ZnO films prepared by ALD [172] and indicates that there is no significant O/OH deficiency in the films due to the short pulse and purge durations.
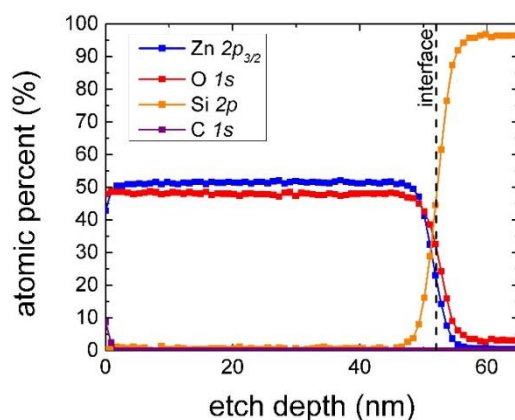
Figure 4.10 XPS depth profile of a 50-nm i-ZnO film deposited at 225 °C with a DEZ partial pressure of 2 mbar, a water partial pressure of 17 mbar, and pulse and purge durations of ~8 ms each.

The variation in crystal orientation with changing deposition temperature of *i*-ZnO films was measured with XRD, see Figure 4.11. The predominant grain orientation of the films changed from (002) for *i*-ZnO films grown at low deposition temperature (105 °C) to (100) for films grown at high deposition temperatures (250 °C). Most reports in the literature show a predominant grain orientation of (002) for *i*-ZnO films deposited by temporal ALD [173, 174]. Nelson *et al.* also found that with shorter exposure/purge times, the (100) and (101) peaks seemed to dominate [164], whereas at longer exposure/purge durations the (002) orientation dominates. This is consistent with the dominance of the (100) peak over the (002) peak in the *i*-ZnO films deposited

in this study. The preferred (100) orientation is consistent with earlier results for *i*-ZnO deposited by spatial ALD [93]. It was proposed that the longer exposure/purge times increase the ability of the precursor molecule to find low-energy sites on the surface.
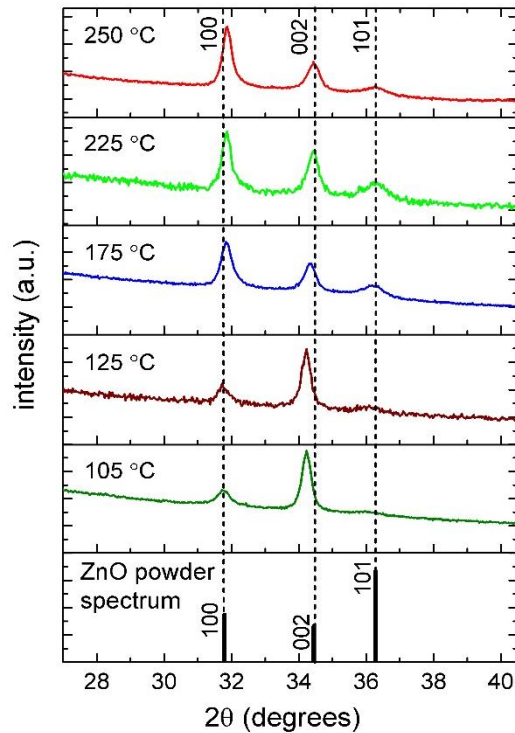
Figure 4.11 XRD 2θ scan of i-ZnO films grown at different deposition temperatures, showing a change in the preferential crystal orientation. The i-ZnO powder spectrum has been included for reference.

4.7   Chapter Summary

In this chapter, the fabrication of *i*-ZnO films by the spatial ALD technique was developed and optimised and the film properties were investigated in detail. A high deposition rate of ~35 nm/min on large-area (125 mm × 125 mm) c-Si substrates was obtained for an industrially-scalable spatial ALD system. The *i*-ZnO films have a high resistivity (~100 Ω-cm) and a refractive index that results in a high transparency (> 90%) in the visible range. The high resistivities of the *i*-ZnO films deposited in this study were attributed to the short precursor exposure and purge times of the spatial ALD technique, as compared to other deposition techniques. XPS results showed that

the *i*-ZnO films were nearly stoichiometric. The preferential crystallographic orientation of the *i*-ZnO films was found to be (100) at higher deposition temperatures, rather than (002) as reported for conventional temporal ALD ZnO films. This is also attributed to the short exposure/purge times. These properties make these *i*-ZnO films ideal for application as the window layer between the CdS buffer and the conductive front contact in CIGS solar cells, to reduce the influence of absorber layer defects from affecting the cell performance. However, one should take into account that ZnO would grow differently on CdS as compared to c-Si, resulting in potentially different material properties. For applications of ZnO as a TCO in CIGS and silicon heterojunction solar cells, lower resistivities are desired and can be achieved by impurity doping *e.g.* Al, B, Ga or In doped ZnO. This preliminary study on *i*-ZnO paves the way for its application in existing and new PV technologies while the advantages of the spatial ALD technique described in this work make it an attractive option for the PV industry.

Chapter 5: Gallium doped ZnO films deposited by spatial ALD[1]

5.1   Introduction

TCOs find applications in optoelectronic devices such as thin-film transistors [175], light-emitting diodes [176], and transparent displays [177]. In the PV field, TCOs are an important part of various thin-film and heterojunction silicon wafer solar cells [83]. Since these applications often require large-area deposition and the usage of temperature sensitive materials, both improvements in materials and the development of scalable and low-temperature processes are important drivers for the application of TCOs in the industry.

The deposition techniques most commonly used for TCOs in the optoelectronic and PV industry are direct current and reactive sputtering [85]. The advantages of sputtering are its relatively low-cost and the availability of high-throughput equipment. However, its main limitation is the surface damage induced to underlying layers and substrates caused by high-energy ions during the process. This surface damage has been shown to directly affect solar cell performance, particularly in the case of heterojunction silicon wafer solar cells [113, 178, 179].

ALD is a low-damage alternative for TCO deposition that does not involve high-energy ions. Though popular for its self-limiting chemical reactions that offer uniform growth and precise control of thickness, the application of conventional (or temporal) ALD in the PV industry was limited until now by its low throughput due to the long purging

---

cycles after each precursor exposure, particularly when H_2O is used as an oxidising agent. However, the advent of high-throughput techniques such as batch and spatial ALD have made ALD industrially viable [180]. Temporal ALD batch reactors can be used to process 50-100 wafers simultaneously [128]. Multiple batch reactors would significantly increase throughput (for the same deposition rate) but would also increase the capital cost. The recent development of the spatial ALD technique offers a cost-effective high-throughput (~3000 wafers per hour, wph) alternative by separating the precursor exposure in space rather than in time [181]. In combination with the industrialisation of ALD-based Al_2O_3 passivation layers for c-Si solar cells [115] has recently triggered the development of spatial ALD on the commercial scale, especially in the PV industry [182].

Currently, indium tin oxide (In_2O_3:Sn or ITO) and variously doped zinc oxide (ZnO:Xx) are the most commonly used TCO materials for PV applications [83, 85]. ITO offers excellent electrical and optical properties. However, its main drawback is the relatively high cost and scarcity of indium. ZnO, on the other hand, is more favourable because of its lower cost and material abundance. Undoped or intrinsic ZnO (*i*-ZnO) films show varying degrees of *n*-type conductivity as presented in Chapter 4. The level of conductivity depends on the presence of defects such as oxygen vacancies, which are largely the result of the material synthesis process and can only be controlled in a very narrow range [85]. To further increase the conductivity of the ZnO films, dopants such as Al, B, Ga, or In are typically used [114].

Undoped and doped ZnO films deposited by temporal ALD have been extensively investigated in the past, with reports of low resistivity and high transparency [114, 159, 163, 172, 183-186]. On the other hand, the development of ZnO films deposited by spatial ALD only gained interest in recent years, predominantly triggered by the need for a high-throughput and low-cost ZnO deposition process for application in the oxide electronic and PV industries [93, 164, 174, 187]. Chapter 4: investigated the properties

of undoped ZnO films deposited by a commercial spatial ALD system [188]. The films showed a uniquely high resistivity which was attributed to the short reaction times of ~8 ms in the spatial ALD technique [188]. Hence, to increase the conductivity of spatial-ALD ZnO films, the use of dopants is essential. Amongst the several doped ZnO films deposited by *temporal* ALD, Al-doped ZnO films are the most widely studied [114, 189-191]. For *spatial* ALD, recent reports discuss Al- and In-doped ZnO films [94, 97, 192]. Unfortunately, the typical Al precursor used (TMA) reportedly etches the ZnO film during the deposition process thereby restricting ZnO growth [193-195]. Further, the high cost of In, even when used as dopant, warrants the investigation of alternate dopants for ZnO.

Table 5.1 Selection of various doped ZnO films deposited by temporal and spatial ALD

No	Dopant	Dopant precursor	ALD type	T_{dep} (ºC)	Doping level (at. %)	Min. ρ (mΩ.cm)	Ref
1	Al	$Al(CH_3)_3$	Temporal	200	1.9	3.1	[189]
2	Al	$Al(CH_3)_2(OiPr)$	Temporal	250	7	1.1	[195]
3	Al	$Al(CH_3)_3$	*Spatial*	200	8	2.0	[94]
4	B	$B(O^iPr)$	Temporal	150	1.6	3.5	[159]
5	In	$In(CH_3)_3$	*Spatial*	200	6	3.0	[97]
6	Ga	$Ga(CH_3)_3$	Temporal	130-210	0-5	0.8	[196]
7	Ga	Ga isopropoxide (GTIP)	Temporal	250	5	3.5	[173]
8	Ga	$Ga(C_2H_5)_3$	Temporal	250	1	2.5	[197]

Gallium-doped ZnO (ZnO:Ga) is relatively less explored as a potential candidate for application in solar cells. ZnO:Ga deposited by temporal ALD exhibits low resistivity $\sim 10^{-3}$ Ωcm with high transmittance > 85% [173, 197, 198]. A summary of the reported properties of ZnO films deposited by temporal and spatial ALD is given in Table 5.1. In this chapter, the material properties of ZnO:Ga films deposited by the industrially-scalable spatial ALD technique are investigated in detail with an aim to demonstrate the potential of ZnO:Ga as a transparent conductive layer for applications in opto-electronic and photovoltaic devices.

5.2 Background information for the fabrication of ZnO:Ga by spatial ALD

ZnO:Ga films deposited by temporal ALD primarily use the technique of supercycles where doping is achieved by the separate ALD growth of the ZnO and Ga_2O_3 phases [96, 173, 197, 199]. This is done by alternating *x* cycles of diethylzinc (DEZ) and water (H_2O) with one cycle of the Ga precursor and H_2O. The published work on ZnO:Ga films deposited by temporal ALD often report some difficulty in growing the Ga_2O_3 phase using a Ga precursor such as trimethylgallium (TMGa) and water (H_2O) at substrate temperatures of < 300 °C [199, 200]. The obstacle arises from using H_2O as an oxidant at lower substrate temperatures. The (CH_3) ligands of TMGa are not easily oxidised by H_2O and require either relatively high substrate temperature ($\geq$ 300 °C), a high-energy plasma source [199], or ozone [200]. If not completely oxidised, the (CH_3) ligands may remain on the surface, preventing subsequent film growth and hence "poisoning" the surface.
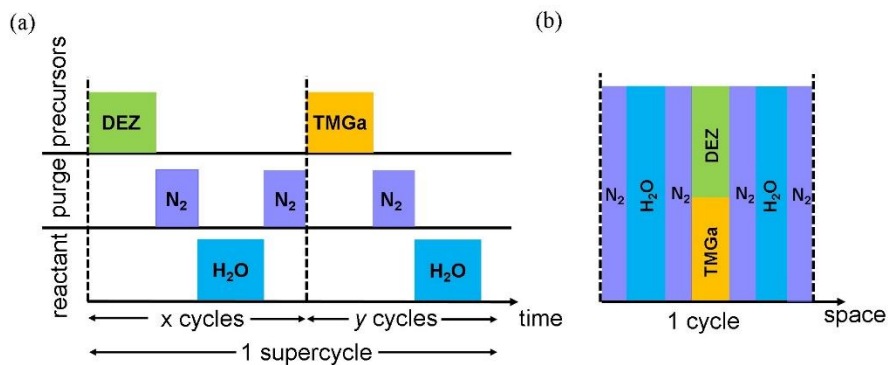
Figure 5.1 Schematic representation of the sequence for precursors during the deposition of Ga doped ZnO films using (a) temporal ALD (supercycles of DEZ and TMGa) and (b) spatial ALD (introduction of pre-mixed DEZ and TMGa simultaneously).

In spatial ALD, on the other hand, the premixed DEZ and TMGa precursors are introduced simultaneously during deposition, as illustrated in Figure 5.1. This results in the incorporation of Ga dopants into the ZnO film during film growth itself, removing the need for the separate growth of the ZnO and Ga_2O_3 phases to enable

doping. Illiberi *et al.* reported similar observations for ZnO:In and ZnO:In,Ga films grown by spatial ALD where film formation was only achieved on co-injecting the In and Ga precursors with DEZ [97, 201]. It has been suggested that exposing the OH-terminated surface simultaneously to both DEZ and the Ga precursor helps catalyse the surface reactions, promoting the incorporation of Ga. The chemisorbed and fragmented Zn atoms possibly form an activated transition state which is reactive enough to cause a polarity-induced dissociation of the metal-ligand bond of a TMGa dopant molecule impinging onto this reactive entity [197, 201]. However, pre-mixing does not ensure the complete oxidation of all incorporated -Ga(CH$_3$)$_2$ ligands to prevent surface poisoning. Further, the potential drawback of pre-mixing the precursors is that the film properties would now be flux-dependent, thus losing out on some of the unique characteristics of ALD. In this work, we investigate for the first time the growth and material properties of ZnO:Ga thin films deposited by industrially scalable spatial ALD, demonstrating its potential for application as a TCO in the PV industry.

5.3   Synthesis of ZnO:Ga thin films using a spatial ALD system

The ZnO:Ga films were deposited using an InPassionLAB$^©$ spatial ALD system from SoLayTec [107, 202]. Diethylzinc (DEZ SSG, AkzoNobel) and deionized water (H$_2$O) were used as the ALD precursors for ZnO deposition. Trimethylgallium (TMGa SSG, AkzoNobel) was used as the dopant source. Nitrogen (N$_2$ > 99.999%, Air Liquide) was used as the carrier gas for all precursors and also as a gaseous separation curtain for the precursor gases in the reactor as illustrated earlier in Figure 4.2. In the setup used for this study, the DEZ and TMGa precursors were first premixed in a gas mixer in the desired ratio before being transported into the spatial ALD reactor. From the mixer the gases were transported through heated lines (set temperature of 65 °C) to prevent condensation. They were then heated further in a heat exchanger to the desired deposition temperature before being injected into the reactor through slits. During each pass the wafer was exposed to one DEZ + TMGa slit and two H$_2$O slits for each ALD

cycle. In this study, constant pulse and purge durations of ~8 ms were used. The H_2O partial pressure was fixed at 65 mbar for each slit. For the DEZ + TMGa mixture, the DEZ partial pressure was kept constant at 2 mbar while the partial pressure of TMGa was varied to control the relative dopant concentration. The ratio of TMGa in the total DEZ + TMGa gas mixture was calculated using the following formula:

$$TMGa\ \% = \frac{(TMGa_{dose})}{(DEZ_{dose} + TMGa_{dose})} \times 100\ \% \qquad (5.1)$$

where *TMGa*$_{dose}$ and *DEZ*$_{dose}$ correspond to the dosage rate of each precursor per slit in the reactor, taking into consideration their partial pressures and carrier flow.

Before deposition, each wafer was heated from room temperature to the desired deposition temperature in a run-in heating chamber and in an inert N_2 atmosphere. The ZnO:Ga films in this study were deposited at 200, 230 and 250 °C. The thickness of the ZnO:Ga films was varied by changing the number of ALD cycles. Pseudo-square 125 mm x 125 mm *p*-type Cz c-Si substrates with a (100) crystal orientation were used as substrates. All substrates were cleaned using a standard RCA clean [154], followed by a dip in a HF solution (1 %) before rinsing and drying. To enable SE measurements, all substrates were polished (surface roughness < 5 Å) on one side by chemical-mechanical polishing. For electrical measurements, the films were deposited on as-procured polished c-Si samples with a 150-nm insulating layer of thermally grown SiO_2 (Latech Scientific Supply Pte. Ltd.).

The thickness of the ZnO:Ga films was measured by SE. A 'pSemi-M0 oscillator model' was used to model the dielectric function of the ZnO:Ga films [155]. The *n* and *k* values obtained from ellipsometry were used to simulate transmittance and absorption spectra of the ZnO:Ga films on an amorphous silicon substrate, using the online simulation tool OPAL2 [203]. The structural properties of the films were investigated using XRD and SEM (see Appendix). Electrical properties were measured using a 4PP system. The carrier concentration and mobility were measured using a Hall

measurement system (Accent, HL5500). XPS with a monochromatic Al K$_\alpha$ X-ray radiation (*hv* = 1486.6 eV, spot size = 400 µm) was used to determine the chemical composition of the films. A flood gun was used to compensate for photoelectron loss and to prevent the samples from charging. The sensitivity factors used for quantification were calibrated with Rutherford backscattering spectrometry (Ga 2$p_{3/2}$, 12.620; O 1s, 2.881; Zn 2$p_{3/2}$, 21.391; C 1s, 0.919) as reported in [159]. For depth profiling, an Ar gun was used to sputter the ZnO:Ga films. In this study, the fraction of Ga atoms incorporated in the ZnO film was defined as:

$$Ga\ \% = \frac{[Ga]}{[Ga + Zn]} = \frac{Ga_{at}\%}{Ga_{at}\% + Zn_{at}\%} \text{ x } 100\ \% \tag{5.2}$$

5.4 Analysis of the growth characteristics of the ZnO:Ga films

In Figure 5.2(a), the growth per cycle (GPC) of the deposited ZnO:Ga films as a function of deposition temperature and TMGa gas ratio is shown. As a reference the GPC of intrinsic ZnO (*i*-ZnO) is also shown [188]. Spatial ALD growth of ZnO:Ga films was successfully achieved at low substrate temperatures with a GPC of ~0.157 nm/cycle at 200 °C (for a range of 0.15 – 0.3% TMGa gas %). It can be seen that the GPC of ZnO:Ga is much lower than the GPC of *i*-ZnO (0.187 nm/cycle for temperatures ≥ 200 °C). Furthermore, it reduces with increasing TMGa gas ratio and with increasing substrate temperatures reaching a minimum of 0.113 nm/cycle at 250°C for a TMGA gas ratio of 0.5%. At higher temperatures, it is expected that an increase in reactivity enables a higher incorporation of –Ga(CH$_3$)$_2$ ligands after exposure to TMGa in the first half of the ALD reaction. In the second half of the ALD reaction, the oxidation rate of the –Ga(CH$_3$)$_2$ surface ligands is also expected to increase with increasing temperature. However, since a corresponding increase in GPC is not observed, it is postulated that Ga is successfully incorporated but not all the

–Ga(CH$_3$)$_2$ ligands are successfully oxidised on exposure to H$_2$O. It is likely that the thermal energy at these temperatures is not sufficient to remove all the remnant –(CH$_3$) ligands using H$_2$O as the oxidant [200]. The remnant -Ga(CH$_3$)$_2$ surface species now "poison" the surface restricting the availability of these sites for subsequent film growth. They may also cause steric hindrance limiting the bonding of Zn-O to adjacent sites. Similarly, the decrease in GPC with increasing TMGa gas ratio is also attributed to a reduction in the availability of reactive surface sites due to the increased incorporation of partially oxidised -Ga(CH$_3$)$_2$ ligands. This observation is consistent with reports of ZnO:In deposited by spatial ALD [97, 201].
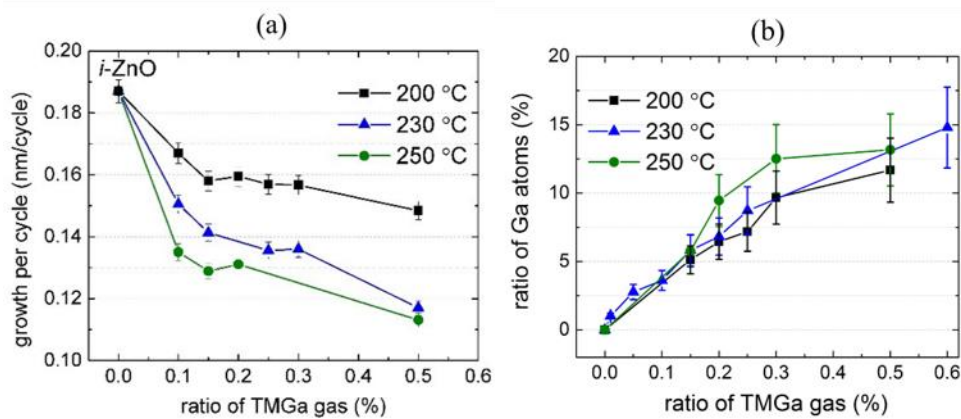
Figure 5.2 (a) Growth per cycle (GPC) of ZnO:Ga films deposited by spatial ALD and (b) ratio of Ga atoms (Ga %) in the films determined by XPS, as a function of the ratio of TMGa gas (TMGa %) in the DEZ + TMGa precursor mixture for substrate temperatures of 200, 230 and 250 °C. The estimated relative error is ~2% and ~10%, respectively.

5.5   Chemical analysis of the ZnO:Ga films

Figure 5.2(b) shows the ratio of Ga atoms (Ga %) incorporated in ZnO as a function of the temperature and TMGa gas ratio during deposition. The Ga % was found to increase with higher TMGa gas ratio with a measured maximum of 15 % for a TMGa gas ratio of 0.6 %. It is important to note that the Ga % reflects the total incorporated Ga dopant in the ZnO film and, hence, is expected to increase linearly with increasing TMGa gas ratio [159]. Some of the Ga forms active dopants whereas the rest form

inactive oxide clusters that do not contribute any charge carriers [159, 190, 204]. The Ga % is not seen to vary largely with deposition temperature. It is only observed to be slightly higher at 250 °C for TMGa gas ratios > 0.2 %. Together Figure 5.2(a) and Figure 5.2(b) indicate that the increased incorporation of Ga (with increasing TMGa gas ratio) corresponds to a decrease in GPC. This supports the hypothesis that the increased incorporation of –Ga(CH$_3$)$_2$ ligands contaminates the surface, which in turn reduces the growth rate of the ZnO:Ga film. GPC displays a strong temperature dependence; however, the same is not observed for the Ga %, which does not vary much with temperature. This suggests a concurrent increase (or decrease) in Ga as well as Zn at higher (or lower) temperatures. Since XPS is a point measurement, an estimate of the non-uniformity of the spatial distribution of Ga over the 125 mm × 125 mm silicon sample is included in the error margin of the measurement result.
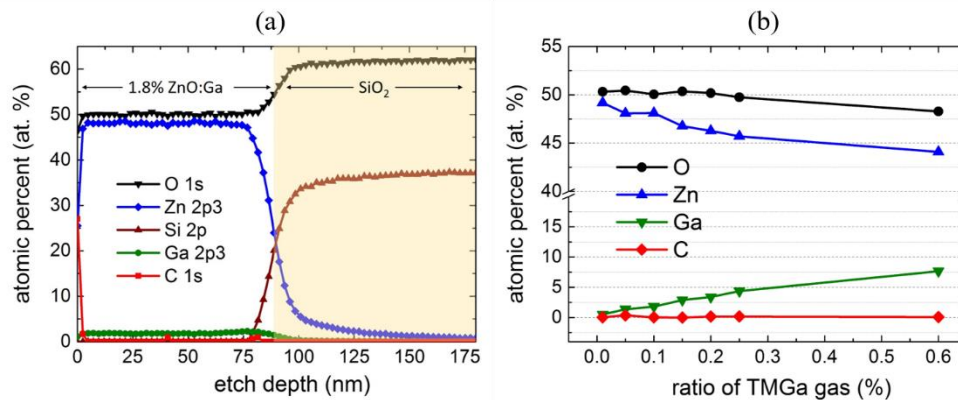
Figure 5.3 Zn, O, Ga and C atomic percentage as a function of (a) the depth from the surface measured by XPS depth profiling and (b) the ratio of TMGa gas (TMGa %), for a 80 nm thick ZnO:Ga sample deposited at 230°C on a c-Si/SiO$_2$ substrate.

The XPS depth profile of an 80 nm thick ZnO:Ga film is shown in Figure 5.3(a). Adventitious carbon (C) was observed at the surface of the film. The C concentration across the bulk of the film after removal of the top layers was found to be lower than the XPS detection limit. The depth profile indicates that the film is O-rich, with an average of 50 at. % oxygen, 48 at. % zinc and 1.8 at. % gallium. The oxygen-rich nature of the films was observed consistently for all the samples in this study and can

be attributed to the short pulse and purge duration used during the spatial ALD process that prevents the formation of oxygen vacancies [188].

Figure 5.3(b) shows the atomic percentages of Zn, O, Ga and C as a function of the TMGa % during deposition. The atomic percentage of Zn and O decrease for higher Ga incorporation. This supports the observation that the ZnO growth rate decreases as more Ga is incorporated for the same DEZ and H_2O partial pressures. Further, from this correlation it is expected that Ga^{3+} dopants substitute the Zn^{2+} ions in the form of electron donors when being incorporated into the ZnO film, as is also observed for Al doping of ZnO [172, 205].

5.6   Structural analysis of the ZnO:Ga films

In Figure 5.4, scanning electron micrographs (top view and cross-section) of a 350 nm thick ZnO:Ga film are shown. The surface morphology exhibits needle-like columnar crystallites, indicating a polycrystalline structure. The crystallites are closely packed together and resemble similar images reported for intrinsic ZnO [93, 188]. The crystallographic orientation of the ZnO:Ga films obtained from XRD measurements is shown in Figure 5.5 for different Ga % as well as for intrinsic ZnO (0%) as a reference. The preferred crystallographic orientations for the ZnO:Ga films are (100) and (101), while the preferred orientations of *i*-ZnO films grown on the same spatial ALD system are (100) and (002) as reported earlier [188]. In the case of ZnO:Ga, the (002) peak appears to be suppressed. Further, a systematic shift of the peaks towards lower angles is observed ($2\theta = 31.85$ for intrinsic ZnO with 0 % Ga and $2\theta = 31.65$ for ZnO with 6.7 % Ga). This shift is attributed to the substitution of Zn^{2+} ions with Ga^{3+} ions in the ZnO lattice, leading to a change in the lattice constant [206, 207]. These observations are all consistent with reports of ZnO:In deposited by spatial ALD where it was

proposed that the quality of the ZnO crystal lattice degrades with increasing dopant content inducing a transition from polycrystalline to amorphous morphology [97, 201].
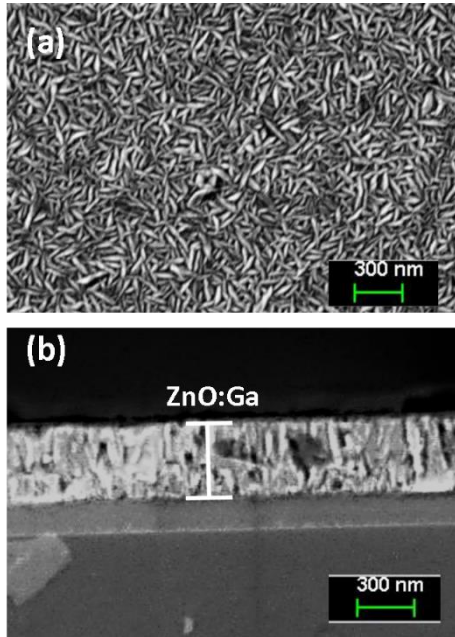
Figure 5.4 (a) Top-view and (b) cross-section SEM images of a 350 nm thick ZnO:Ga film deposited at 230 °C with 4.7 at. % of Ga incorporated as measured by XPS.
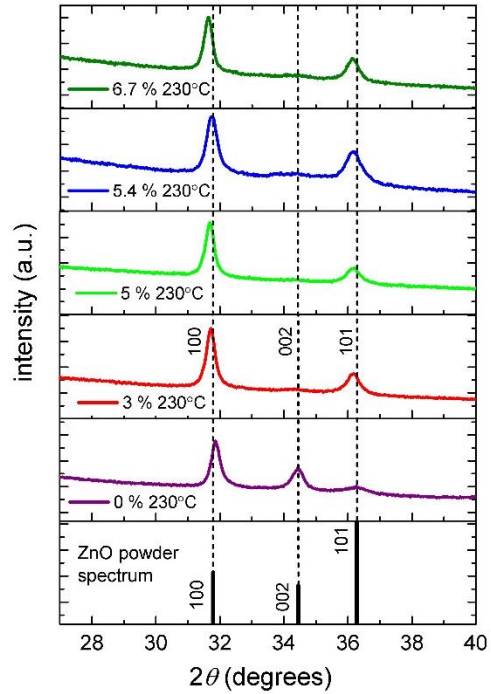
Figure 5.5 XRD 2θ scan of 80 nm thick ZnO:Ga deposited at 230 ºC with increasing Ga at. % incorporated as measured by XPS. The ZnO powder spectrum is also included for reference.

5.7   Electrical analysis of the ZnO:Ga films

The first requirement of a TCO is that it should have a low resistivity to prevent excessive resistive losses during lateral charge transport to the metal grid. The resistivity of ZnO:Ga films as a function of TMGA gas ratio (TMGa %) during deposition at a temperature of 230 °C is presented in Figure 5.6. It is observed that the resistivity decreases with increasing TMGa % to a minimum resistivity of 3.5×10^{-3} Ω.cm for a TMGa range of 0.15 to 0.2 %. On further increasing the TMGa %, the resistivity starts to increase again due to the incorporation of additional Ga dopants that form inactive oxides and do not contribute free carriers to the ZnO film. In Figure 5.7, the resistivity as a function of the incorporated Ga is shown for substrate temperatures

of 200, 230 and 250 °C during deposition. It can be seen that a substrate temperature greater than 230 °C is required to obtain ZnO:Ga films with low resistivities. At a substrate temperature of 200 °C, the minimum resistivity obtained was 37×10^{-3} Ω.cm at a Ga fraction of 6.4%. At 230 °C, a minimum resistivity of 3.5×10^{-3} Ω.cm was obtained for a Ga range from 5.8% to 8.2% while at 250 °C, a relatively low resistivity of 2×10^{-3} Ω.cm was obtained for much higher Ga %. These resistivity values are comparable to resistivities reported for doped ZnO films deposited by temporal and spatial ALD as can be seen in Table 5.1.
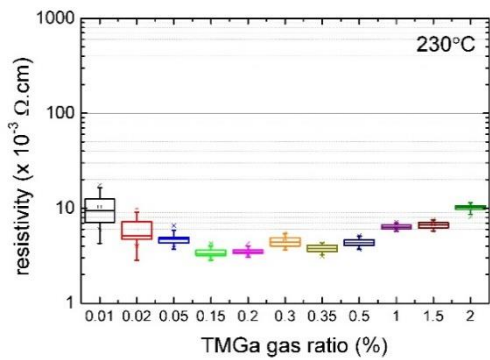
Figure 5.6 Resistivity of Ga-doped ZnO films as a function of TMGa gas % for 100 ± 10 nm thick films deposited at a substrate temperature of 230 °C. The box plots represent the 25th, 50th and 75th percentile along with the standard deviation of the data.
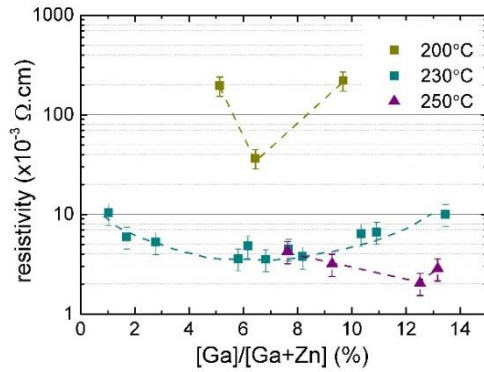
Figure 5.7 Average resistivity as a function of the Ga fraction ([Ga]/[Ga + Zn]) for 100 ± 10 nm thick films deposited at temperatures of 200, 230 and 250 ºC. An error of 25 percent is taken into consideration and the dashed lines are guides to the eye.

Figure 5.8(a) presents the average sheet resistance (R_{sheet}) as a function of the ZnO:Ga film thickness for a fixed TMGa gas ratio of 0.2% at 200, 230 and 250 °C. Due to the effect of temperature on Ga incorporation, the corresponding Ga % is 6.4 % (for 200°C), 7.7 % (for 230 °C) and 9.3 % (for 250 °C). At 230 °C, a 85 nm thick ZnO:Ga film was found to have a sheet resistance of ~400 Ω/sq which was reduced down to ~100 Ω/sq for a thickness of 200 nm. It can also be seen that the average sheet resistance for films deposited at 230 °C and 250 °C follow similar trends whereas for a temperature of 200 °C the sheet resistance values were significantly higher. The

average resistivity of the ZnO:Ga films in Figure 5.8(a) is shown as a function of film thickness Figure 5.8(b). It can be seen that at 230 °C, the average resistivity drops from 3.5×10^{-3} Ω.cm for an 85 nm thick film to 2×10^{-3} Ω.cm for thicknesses greater than 200 nm. This drop is attributed to a reduction in crystallographic defects (e.g. grain boundaries) for thicker films which reduces carrier scattering [79]. As expected, the resistivities for films deposited at 200 °C were much higher with values $> 10 \times 10^{-3}$ Ω.cm while the trend of films deposited at 250 °C for a similar TMGa ratio of 0.2 %, follows closely that of 230 °C. Since this work aims to study the potential of ZnO:Ga films for application as TCOs in heterojunction silicon wafer cells, where high substrate temperatures are intolerable, the majority of this paper focuses on ZnO:Ga films deposited at 230 °C.
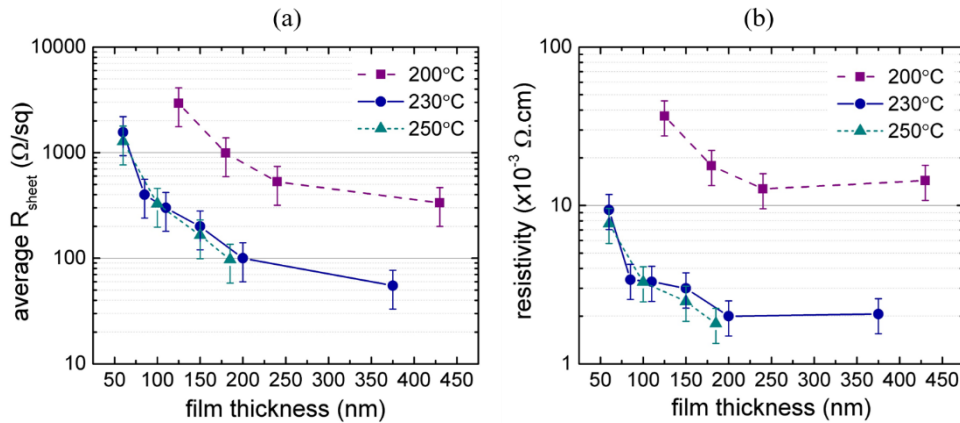
Figure 5.8 (a) Average sheet resistance R_{sheet} and (b) average resistivity as a function of film thickness for Ga-ZnO films deposited with 0.2 % TMGa at 200, 230 and 250 °C. A measurement uncertainty of (a) 40% and (b) 25 % is considered. The lines are guides to the eye.

The carrier concentration determined by Hall measurements for ZnO:Ga films deposited at a substrate temperature of 230 °C and a thickness 100 ± 10 nm is shown in Figure 5.9(a) as a function of the Ga fraction in the films. A negative charge carrier concentration N_c was measured for the ZnO:Ga films indicating *n*-type conductivity. The carrier concentration was found to increase with increasing Ga % up to 5.6×10^{20} cm^{-3} (for 6.2 % Ga) and then decreased for higher Ga content in the films.

This trend is consistent with reports in the literature of ZnO:Ga films deposited by temporal ALD [173, 197]. The decrease in the charge carrier concentration may be due to the dopants occupying interstitial sites, dopant clustering, or the formation of oxides and metastable phases that make the dopant inactive [159, 190]. The charge carrier mobility also obtained from Hall measurements is presented in Figure 5.9(b). For low Ga % the mobility is as high as 5.4 $cm^2V^{-1}s^{-1}$. However, this drops down rapidly to values < 2 $cm^2V^{-1}s^{-1}$ for higher Ga %. Typically the most dominant scattering process that limits carrier mobility when $N_c \geq 1 \times 10^{20}$ cm^{-3} is the Coulombic scattering that arises from the introduction of ionised dopants, known as ionised impurity scattering [79, 90, 208]. For homogeneously dispersed ionised dopants, the impurity scattering scales with N_c. The observed decrease in μ_H was attributed to this increase in impurity scattering.
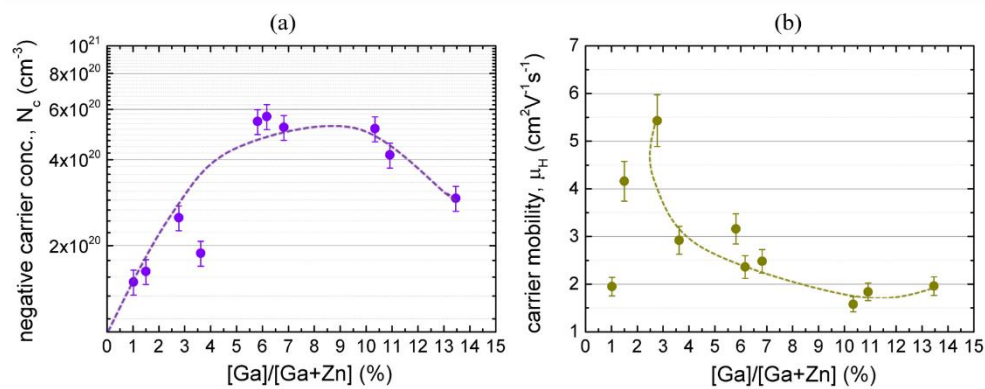
Figure 5.9 (a) Charge carrier concentration N_c and (b) charge carrier mobility μ_H of ZnO:Ga films as a function of [Ga]/[Ga+Zn]. The films were deposited at a substrate temperature of 230 °C and had a thickness of 100$\pm$10 nm. The dashed lines are guides to the eye. A standard error of 10% is estimated.

5.8   Optical analysis of the ZnO:Ga films

SE measurements were used to extract the *n* and *k* values of the ZnO:Ga films. Figure 5.10(a) shows the *n* and *k* values for ZnO:Ga films with various Ga %. The dielectric functions closely follow the spectra reported in the literature [166, 167, 188].The refractive index, *n* of the ZnO:Ga films was found to be between 1.85 (higher Ga

fractions) to 1.95 (lower Ga fractions) at 632 nm. The value of *n* can be seen to decrease with increasing Ga fraction accompanied by a shift in the *n* peak towards higher photon energies. A distinct broadening of the *n* peak can be seen with increasing Ga in the films. A similar decrease, shift and broadening is observed for the *k* edge at higher photon energies whereas at lower energies the value of *k* increases instead with increasing Ga. The shifts at higher photon energies was attributed to an increase in optical bandgap (Burstein-Moss shift) and will be discussed in more detail below. The increase in *k* at lower photon energies was attributed to an increase in free carrier absorption [166]. The peak in the *k*-spectra at ~3.5 eV for low Ga % originates from excitonic transitions as reported earlier [166, 209]. The broadening of a transition peak is inversely proportional to the lifetime of carriers or excitons [210, 211]. Keeping this in mind, Figure 5.10(a) implies that the carrier or exciton lifetime is shorter when the electron concentration increases which has also been observed for ZnO:Ga films deposited by magnetron sputtering [166].
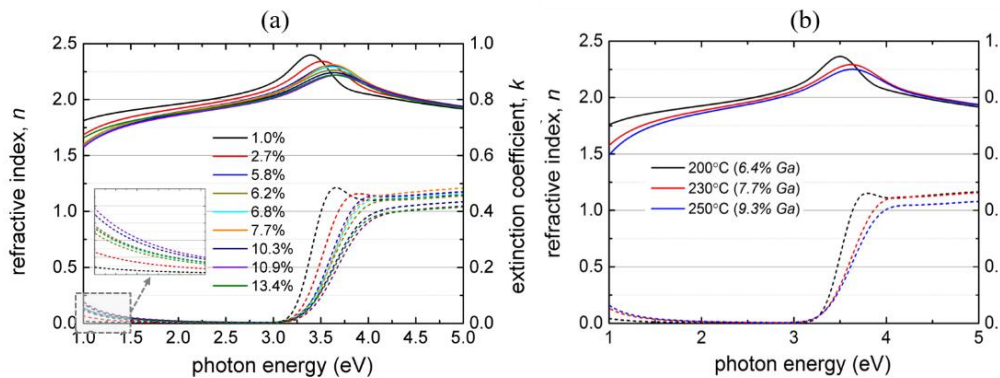
Figure 5.10 The refractive index (n) and extinction coefficient (k) extracted from SE measurements as a function of photon energy for 80-100 nm thick ZnO:Ga films (a) deposited at 230 °C with increasing TMGa gas ratio and hence increasing Ga %, and (b) deposited at 200, 230 and 250 °C with a fixed TMGa gas ratio of 0.2%.

The *n* and *k* values of ZnO:Ga films deposited at a substrate temperature of 200, 230 and 250 °C are shown in Figure 5.10(b). The films were deposited with a constant TMGa gas ratio of 0.2 % resulting in Ga % of 6.4, 7.7 and 9.3 % for 200, 230 and 250 °C respectively, as measured using XPS. The effect of increased carrier

concentration on the *n* and *k* spectra for films with higher Ga content ≥ 6 % (deposited at 230 and 250 °C) is also observed in Figure 5.10(b) [just as in Fig. Figure 5.10(a)] and is consistent with the results of the electrical measurement.
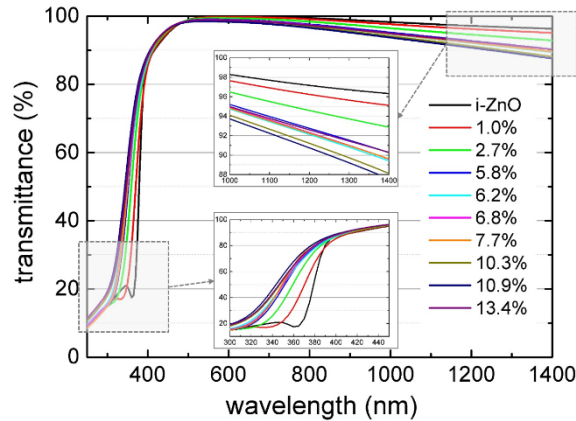
Figure 5.11 Transmittance of a 80 nm thick ZnO:Ga film deposited on a textured c-Si substrate at 230 °C for increasing fractions of Ga %.Transmittance was simulated using OPAL 2 with n and k values obtained from SE measurements [203]

The transparency of the ZnO:Ga films is key to evaluating its potential for application as a TCO. The *n* and *k* values extracted from SE measurements of ZnO:Ga films for increasing Ga % were used to simulate the transmittance of a 80 nm thick film on a silicon substrate and is shown in Figure 5.11. The transmittance is greater than 90 % for large part of the visible and near-infrared wavelength range (500 – 1200 nm). In the infrared region (> 1200 nm), a decrease in transmittance was observed with increasing Ga % explained by an increase in free-carrier absorption. However, for the highest Ga content of 13.4 %, the transmittance is seen to increase instead. This behaviour, also observed by Garcia *et al.* for ZnO:B films, is attributed to the decrease in carrier concentration for such high doping levels which corresponds to a decrease in free-carrier absorption [159]. In the ultraviolet wavelength region, a shift in the absorption edge towards lower wavelengths was observed for increasing Ga %. This blue shift was attributed to an increase in optical band gap as explained below.

The optical bandgap ($E_{g,opt}$) determined from SE measurements is shown in Figure 5.12 as a function of the incorporated Ga for ZnO:Ga films deposited at a substrate temperature of 230 °C. It can be seen that the optical bandgap increases with increasing Ga %. This increase is attributed to the Burstein-Moss shift (B-M shift) [212]. This effect describes the apparent increase in the bandgap of a semiconductor as a result of the energy levels close to the edge of the conduction band being filled dopant carriers as illustrated below. This raises the Fermi level into the conduction band since all the occupied states at the bottom of the conduction band are unavailable for optical transitions. In this respect, high doping of the TCO is beneficial since the transparency is extended to higher photon energies. This effect explains the results of Figure 5.12 and is consistent with reports in the literature [173, 197, 198].
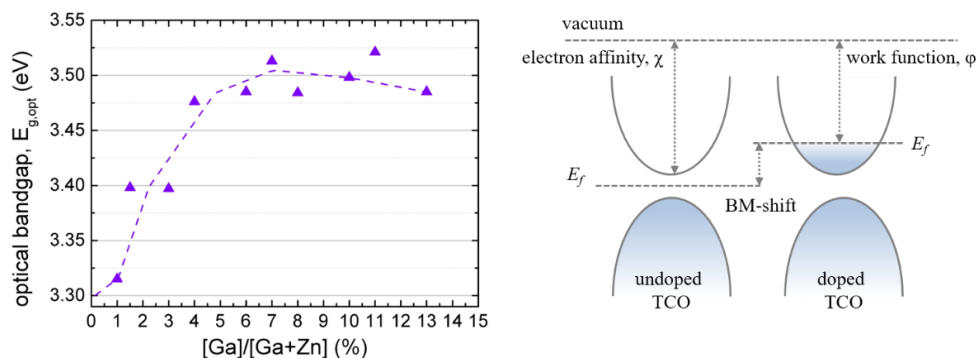
Figure 5.12 (Left) The increase in optical bandgap $E_{g,opt}$ obtained from SE modelling as a funciton of the incorporated Ga % for a 100 nm thick ZnO:Ga film deposited at 230 °C attributed to the Burstein-Moss shift. (Right) Schematic band diagram of an undoped and doped TCO illustrating the Burstein-Moss shift due to filled energy levels in the conduction band that increase the optical bandgap.

5.9 Chapter Summary

ZnO:Ga films were deposited using spatial ALD at relatively low substrate temperatures in the range of 200 – 250 °C. In contrast to conventional temporal ALD where Ga doping of ZnO is commonly achieved by alternating *x* cycles of DEZ and H_2O with 1 cycle of TMGa and H_2O, the DEZ and TMGa were premixed and introduced simultaneously. This circumvents the difficulty of growing the Ga_2O_3 phase

separately using TMGa and H_2O as precursors at low temperatures and Ga doping was achieved by the incorporation of Ga atoms into the ZnO film during film growth itself. However, with increasing Ga incorporation the growth rate of the ZnO:Ga film was found to decrease. This is attributed to remnant partially oxidised $–Ga(CH_3)_2$ ligands that reduce available surface sites for subsequent ZnO film growth. An investigation of the material properties of the ZnO:Ga films revealed that the films were oxygen-rich and polycrystalline, with preferred crystallographic orientations of (100) and (101). The (002) plane, which was dominant for intrinsic ZnO films, was suppressed by the addition of the Ga dopant.

The ZnO:Ga films (100 ± 10 nm) yielded resistivities as low $\sim2x10^{-3}$ Ω-cm when deposited at a substrate temperature of 250 ℃ and $\sim3.5x10^{-3}$ Ω-cm at a temperature of 230 ℃. The high carrier concentration obtained for these films compensated for their relatively low carrier mobility. A substrate temperature of 200 ℃ was found to result in much higher resistivity films, while thinner films (< 80 nm) also showed significantly higher resistivity, attributed to increased grain boundary scattering. At the same time, the ZnO:Ga films displayed a transmittance > 95% in the visible and near-infrared wavelength regions for 80 nm thick films. Further, it was found that the optical bandgap is easily modified by varying the Ga % in the films. These electrical and optical properties demonstrate the potential of ZnO:Ga films for application as a transparent conductive oxide in heterojunction silicon wafer and thin-film solar cells. Furthermore, these properties in combination with the advantages offered by the industrially-scalable high-throughput spatial atomic layer deposition technique, pave the way for its cost-effective large-scale production in the PV industry.

Chapter 6: Application of spatial ALD Al₂O₃ films in 20.1 % *p*-type Al-LBSF solar cells

6.1   Introduction

Conventional *p*-type c-Si solar cells employ a full-area rear Al contact that forms an alloyed back surface field (Al-BSF), first developed in the late 1960s (see Section 2.5.2) [213]. The full-area silicon-metal contact at the non-illuminated rear side of this type of solar cell results in relatively high surface recombination. Furthermore, the relatively low dielectric contrast between silicon and aluminum suppresses rear metal reflection [109]. It was found that reducing the rear contact area and inserting a lower index dielectric material between the rear metal and silicon can significantly reduce these electrical and optical losses. As a result, new schemes were developed where the rear side is passivated by a dielectric covered by a full area metal film and the dielectric is locally opened to allow a contact between the metal and the silicon [214-216]. Early developments led to the first PERC cell which demonstrated an efficiency of 22.8 % [215]. Variations of the p^+ region at the rear gave rise to 'a family' of PERC cell structures. These include the Al-LBSF cell where the Al rear contact forms local alloyed p^+ regions in the Si and the passivated emitter rear locally-doped (PERL) structure where the p^+ region is formed by an additional diffusion process. These cells show significantly higher open-circuit voltage (V_{oc}) and short-circuit current densities (J_{sc}) as compared to the standard Al-BSF solar cells.

In the 1980s/1990s, the Al-LBSF structure was studied extensively by Aberle *et al.* using positively-charged thermal SiO_2 and a-SiN_x:H as the rear surface passivating layer [216]. More recently, it was shown that Al_2O_3 can provide excellent levels of surface passivation on *p*-type silicon surfaces [66]. This is partly due to its intrinsic

high negative fixed charge density which induces an accumulation layer at the p-type c-Si surface rather than an inversion layer induced by the intrinsic positive charge in SiO_2 and a-SiN_x:H, which can even result in parasitic shunting [71]. The first report of PERC solar cell with an Al_2O_3 passivated rear was reported in 2008, with a champion efficiency of 20.6 % [52, 121]. Nowadays, Al_2O_3 (typically capped by SiN_x) is the de-facto standard for the passivation of the rear surface of industrial Al-LBSF and PERC solar cells [14, 126].

As discussed in Chapters 2 and 3, Al_2O_3 deposited by ALD demonstrates excellent surface passivation properties, leading to widespread interest within the PV community. Due to the limitation of conventional (temporal) ALD for high-throughput applications, the PECVD method was preferred in the PV industry since it was already being extensively used for the deposition of the a-SiN_x:H antireflection coating. However, with the recent development of the high-throughput spatial ALD technique, this restriction has been overcome. In this chapter, we demonstrate the application of spatial ALD thin films (fabricated using the low-cost solar-grade precursor tested in Chapter 3) for the rear surface passivation of Al-LBSF solar cells, achieving a champion solar cell efficiency of 20.1 %.

6.2 Solar cell fabrication process

Large-area 156 mm x 156 mm p-type monocrystalline Cz-Si wafers were used for the fabrication of the Al-LBSF solar cells. The process steps for the fabrication and the schematic of the solar cell structure are shown in Figure 6.1.
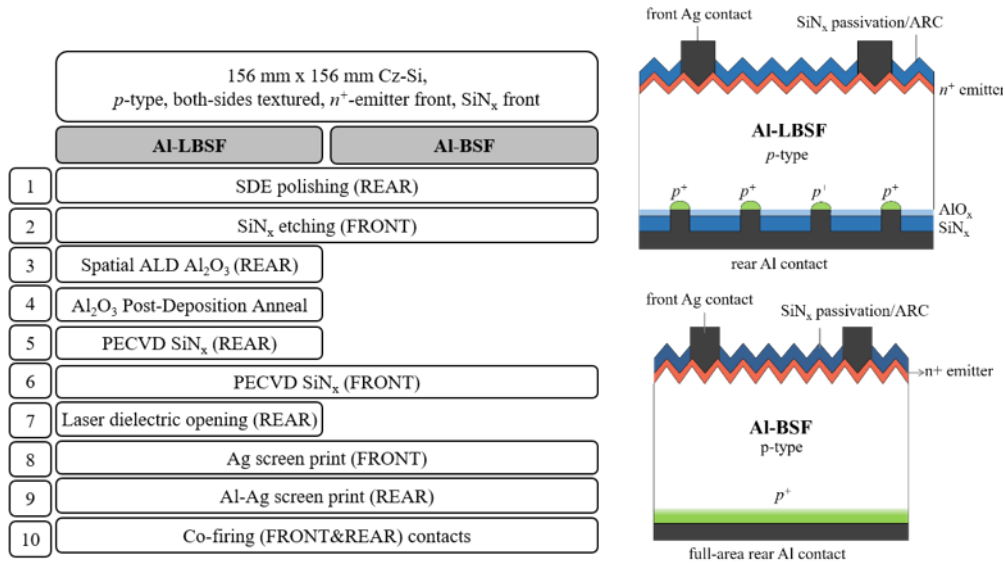
Figure 6.1 Process steps for fabrication of the Al-LBSF and reference Al-BSF solar cells (left) and a schematic illustration of the Al-LBSF and Al-BSF cell structures.

Pre-diffused print-ready wafers (180 µm, 2.5 Ω-cm *p*-type Cz-Si, 90 Ω /sq n^+ emitter with 70 nm a-SiN$_x$:H coating on the front side), procured from a solar cell manufacturer, were used as the starting material. The wafers were first subjected to a saw damage etch (SDE) in potassium hydroxide (KOH) and deionized (DI) water solution to polish the rear side. The a-SiN$_x$:H coating acted as a mask to protect the front surface. This sacrificial a-SiN$_x$:H layer was removed in a 10 % hydrofluoric (HF) acid solution and all wafers were subjected to a standard RCA wet-chemical clean [154]. At this stage, the samples had a bare textured front with the n^+ emitter and a planarised rear. The samples were then split in two groups for the processing of Al-LBSF and standard Al-BSF cells. The Al-LBSF cells were passivated with 10 nm of Al₂O₃ using a commercial spatial ALD system (InPassionALD, SoLayTec) with low-cost solar-grade TMA as the precursor. The samples underwent a post-deposition anneal at 425 ºC for 20 mins, and subsequently both sample groups were capped with 80 nm and 120 nm a-SiN$_x$:H film on the front and rear, respectively, using an inline remote-PECVD reactor (SiNA, Meyer Burger). For the Al-LBSF group, the rear dielectrics were locally opened by laser ablation (InnoLas), with a pitch of 0.85 mm. Finally the front fingers

and busbars were screen-printed (ASYS) using a silver paste and a full-area rear electrode was printed using aluminium paste, for both Al-LBSF and Al-BSF samples. In the former cell structure, the rear Al fills the ablated regions in the dielectric to contact the bulk Si. The samples were then subjected to a co-firing process (~ 850 ºC peak firing temperature) which ensured a good contact formation at the front and the formation of a BSF at the rear. All passivation and metallization steps were conducted at Fraunhofer ISE, Germany, as the solar cell laboratories at SERIS were not available at that time. Initially, Al-LBSF cells with rear Al$_2$O$_3$ films synthesised by PECVD (at an external facility in Singapore) were also included in the study for comparison. However, these Al$_2$O$_3$ films demonstrated poor quality which was attributed to a non-optimised PECVD process. To ensure a fair comparison, these results were not included in this chapter.

6.3   Results and Discussion

6.3.1   Current density-voltage (*J-V*) characteristics

The *J-V* characteristics of the Al-LBSF and Al-BSF cells were measured by a commercial *J-V* tester (SINUS220, Wavelabs) and the results for the champion cells from each group are shown in Figure 6.2 and Table 6.1. The champion Al-LBSF cell (with spatial ALD Al$_2$O$_3$) on the rear performed very well with an efficiency of 20.1 %, as compared to the champion cell from the reference Al-BSF group that showed an efficiency of 19.2 %.

A statistical distribution of the one-Sun *J-V* parameters for the entire batch of Al-LBSF and Al-BSF solar cells is shown in Figure 6.3. The average efficiencies obtained were 19.7 % for the Al-LBSF cells and 19.0 % for the standard Al-BSF cells. The average efficiency gain for the solar cells with rear spatial ALD Al$_2$O$_3$ was thus about 0.7 %$_{abs}$.

This gain was due to the higher open-circuit voltage (ΔV_{avg} of 18 mV) and the higher short-circuit current density (ΔJ_{avg} of 1.2 mA/cm^2). The standard Al-BSF solar cells, however, showed a higher fill factor (*FF*) with an average of 80.2 % as compared to 78.4 % for the Al-LBSF cells.
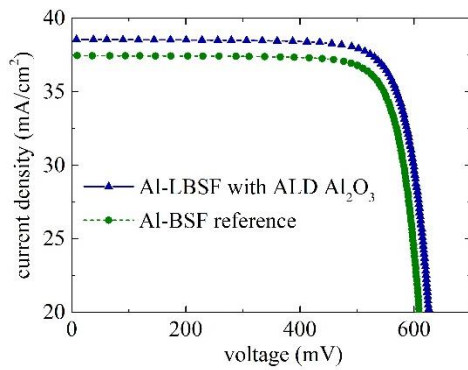
Table 6.1 Best cell J-V parameters at 1-sun

Parameter	Al-LBSF	Al-BSF
Eff* (%)	20.1	19.2
J_{sc} (mA/cm^2)	38.6	37.4
V_{oc} (mV)	654	636
FF (%)	79.7	80.5

*As-deposited efficiency

Figure 6.2 (Left) The champion-efficiency J-V curves for Al-LBSF cells with rear Al₂O₃ synthesised by spatial ALD and reference Al-BSF cells. (Right) A summary of the one-Sun J-V parameters of the same cells.
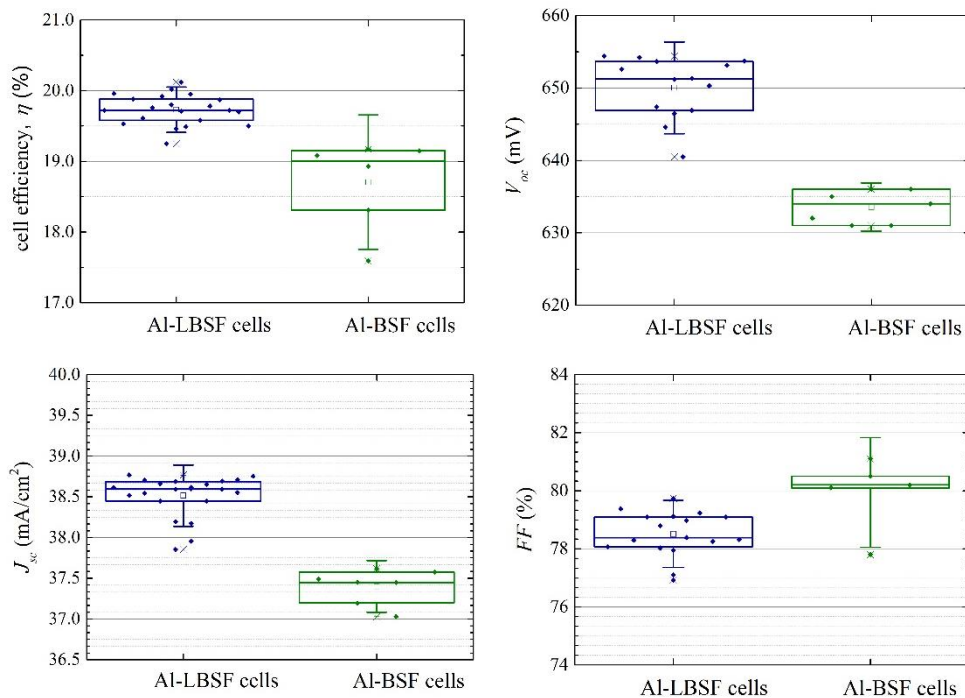
Figure 6.3 Statistical box-chart comparisons of the one-Sun J-V parameters for the Al-LBSF solar cells using spatial ALD Al₂O₃ as the rear passivating dielectric and for the standard Al-BSF solar cells.

6.3.2 Photoluminescence (PL) and Electroluminescence (EL) imaging

Open-circuit photoluminescence (PL) images are obtained by illuminating a sample with light of one-Sun intensity and subsequently measuring the sample's luminescence. In PL, dark areas indicate regions of high carrier recombination, while bright areas indicate regions with high minority carrier lifetime. In electroluminescence (EL) imaging, a forward bias is applied to a solar cell in the dark and the luminescence is captured by a Si camera. PL and EL images give a spatially resolved indication of the electrical quality of a solar cell. A series resistance (R_s) map can be derived from PL imaging following the method of Kampwerth *et al.* [217]. In Figure 6.4, the PL and EL images at open-circuit conditions along with a series resistance (R_s) map derived from the PL measurement for the champion Al-LBSF with spatial ALD Al₂O₃ are shown. The PL and EL images indicate good spatial uniformity, with no local shunts. The R_s map indicates a few regions with relatively higher series resistance.
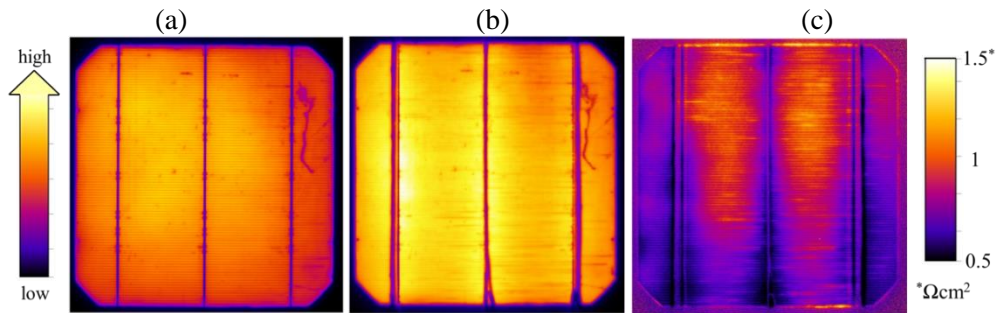
Figure 6.4 (a) Measured PL intensity under one-Sun V_{oc} conditions,(b) measured EL intensity in the dark with a forward current of 8 A, and (c) derived spatial distribution of the one-sun series resistance R_s (in Ωcm^2) for the champion Al-LBSF solar cell with rear Al₂O₃ deposited by spatial ALD.

6.3.3 Open-circuit voltage (V_{oc}) loss analysis

In this section, the methods described by Wong *et al.* were used to identify regions of high recombination in the solar cells that contribute to V_{oc} losses using PL imaging [218]. At reasonable PL illumination intensities, the photon flux density ϕ detected by the PL camera may be written as

$$\phi = C \left(e^{\frac{qV}{kT}} \right) = C \left(\frac{pn - n_i^2}{n_i^2} \right) \tag{6.1}$$

where ϕ is in units of $cm^{-2}s^{-1}sr^{-1}$ denoting photons per second per unit area per unit solid angle, p and n are the free hole and electron concentrations, n_i is the intrinsic carrier concentration at thermal equilibrium. C is a calibration constant related to the optical properties of the solar cells and the PL system and is particularly influenced by the band-to-band absorptance of the sample [218]. In the emission band near 1100 nm, this absorptance largely varies due to the rear internal reflectance of the solar cell. The *pn* product for the analysed samples was determined from their PL count as a function of the PL illumination intensity measured by a monitor photodiode and the values of *C* were extracted. A value of 3.78 was obtained for the Al-BSF reference solar cell while a higher value of 5.63 was obtained for the Al-LBSF. This indicates a much higher reflectance at the rear surface for the Al-LBSF samples as compared to the Al-BSF sample, a result of the lower refractive index Al₂O₃ passivating dielectric at the rear that enable higher internal reflectance. This is consistent with the reflectance spectra of the champion Al-BSF and Al-LBSF solar cells measured in the 1000 to 1200 nm range as shown in Figure 6.5.
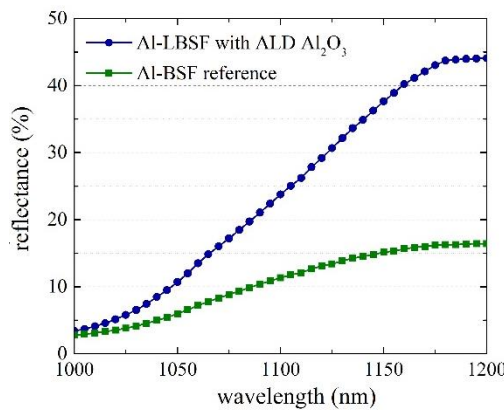
Figure 6.5 Measured reflectance of the champion Al-LBSF and Al-BSF solar cells in the wavelength range of 1000-1200 nm.

The Suns-PL and Suns-V_{oc} curves obtained from PL measurements at different illumination intensities are shown in Figure 6.6 [219, 220]. In Suns-PL, the PL

intensity from a sample is measured for a range of illumination intensities which can be calibrated to one-Sun conditions by measuring the short-circuit current of a solar cell. In this way, the light intensity can be defined in units of "Suns" and the implied and probed V_{oc} of the sample at over a range of suns can be determined. The Suns-PL and Suns-V_{oc} curves can be analysed using the two-diode model for solar cells, under open-circuit conditions, as given by

$$J_L = J_{01} \left[exp \left(\frac{qV}{k_B T} \right) - 1 \right] + J_{02} \left[exp \left(\frac{qV}{2 k_B T} \right) - 1 \right] \tag{6.2}$$

where J_L is the light-induced current density, and J_{01} and J_{02} are the first and second diode saturation current densities, respectively. It is important to note that the shunt resistance was assumed to be large and, hence, has a negligible influence on the *J-V* curve. Table 6.2 lists the J_{01} and J_{02} values derived for the Al-BSF and Al-LBSF solar cells at 25 ºC.
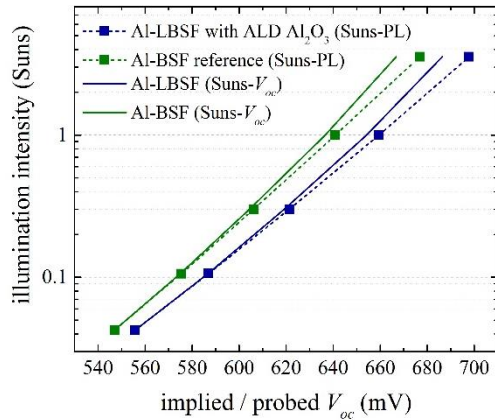
Table 6.2 First and second diode saturation current density values for the BSF and LBSF cells.

Cell type	J_{01} (fA/cm²)	J_{02} (nA/cm²)
Al-LBSF with spatial ALD Al₂O₃	306	18
Al-BSF	670	11

Figure 6.6 Calibrated Suns-PL curves showing illumination intensity as a function of the implied V_{oc} for the LBSF and BSF champion solar cells. The solid lines denote the Suns-V_{oc} curves as a function of probed V_{oc} at different intensities.

It can be seen that the champion Al-LBSF cell with spatial ALD Al₂O₃ exhibits the lowest J_{01} value (300 fA/cm²) as compared to J_{01} for the reference Al-BSF cell (670 fA/cm²). This indicates significantly lower recombination losses for the cell with spatial ALD Al₂O₃. The high value obtained for the Al-BSF cell was attributed to rear surface recombination due to its full-area metal contact. Since all the cells had the same

front metal contacts and passivated emitter, the differences in J_{01} were considered representative of the differences in the J_0 components arising from the rear metallisation and base passivation of the solar cells. On the other hand, the reference Al-BSF cell exhibited the lowest J_{02} current which was attributed to non-ideal recombination associated with the second diode. This is likely a result of the difference in process steps and conditions experienced by the two cell structures.

6.3.4   Short-circuit current density (J_{sc}) loss analysis

The mechanisms contributing to a loss in J_{sc} can be broadly classified as either parasitic absorption losses and collection losses, such that optical current losses (e.g. ARC reflection, front surface escape and parasitic absorption in the rear reflector) can be clearly differentiated from losses due to recombination (e.g. the high recombination at the rear surface). The ratio of current generated by a solar cell to the power of the incident illumination, measured over a range of wavelengths (typically 300 nm to 1200 nm for c-Si cells) at short-circuit conditions, is known as the cell's spectral response (SR). The measured SR can alternately be expressed as the ratio of the number of electron-hole pairs collected by a solar cell to the number of incident photons. This is known as the spectrally resolved external quantum efficiency (EQE) of a solar cell. Figure 6.7 shows the EQE of the champion Al-LBSF and Al-BSF solar cells measured using a single-point SR system (Bentham, PVE300-IVT) with a bias light intensity of 0.3 Suns. For convenience, the same figure is drawn up with various lines to show the spectrally dependent current loss mechanisms. These lines divide the graph into loss components due to reflection from the anti-reflective coating (ARC), combined ARC absorption and imperfect emitter collection (blue loss), imperfect base collection, parasitic absorption (predominantly at the cell rear) and front surface escape. The weighted integral of these current loss fractions with the AM1.5G photon flux

spectrum, upon multiplication with the elementary charge q, are the current density contributions (in mA/cm^2) as displayed in the pie charts in Figure 6.7 [218, 221].
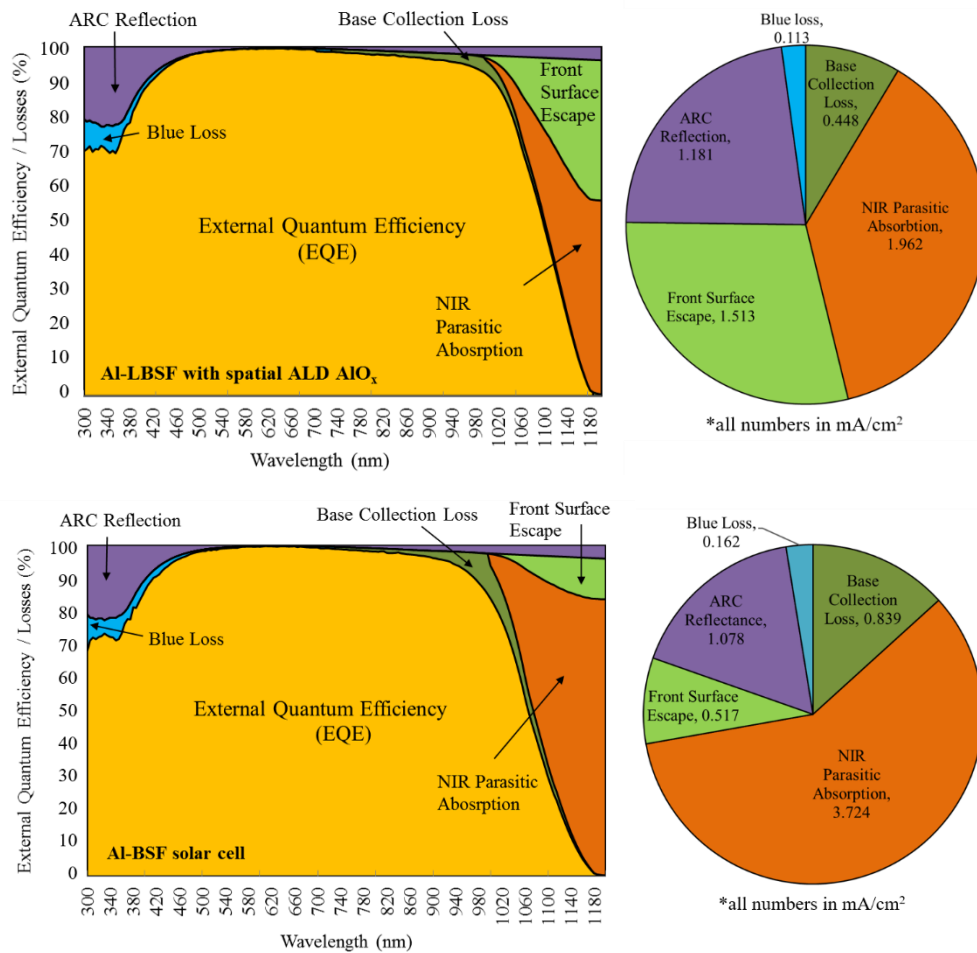
Figure 6.7 Measured external quantum efficiency (EQE) for (top) the champion Al-LBSF cell (20.1%) with spatial ALD Al₂O₃ and (bottom) the champion Al-BSF solar cell (19.2%). The corresponding pie charts of the weighted integral of various loss components (in mA/cm²) is also shown.

The primary difference in the J_{sc} losses for the champion Al-LBSF and Al-BSF cells came from the NIR parasitic absorption with a corresponding current density loss of 1.96 and 3.72 mA/cm^2, respectively. This is accompanied by a distinctly higher front surface escape for the Al-LBSF (1.5 mA/cm^2) cell as compared to the Al-BSF (0.5 mA/cm^2) cell. Both optical losses are explained by the lack of the rear dielectric reflector in the standard Al-BSF solar cells. The recombination losses at the rear surface contribute to a base collection loss of 0.45 mA/cm^2 for the Al-LBSF cell and

0.84 mA/cm^2 for the Al-BSF cell, clearly demonstrating the advantages of the passivating spatial ALD Al$_2$O$_3$ at the rear. All the integrated J_{sc} losses add up to a total of 5.2 mA/cm^2 for the Al-LBSF cell and a total of 6.3 mA/cm^2 for the Al-BSF cell, a difference of 1.1 mA/cm^2 which is very similar to the J_{sc} difference of 1.2 mA/cm^2 measured from *J-V* characterisation. It is evident that the Al-LBSF cell structure displays significantly improved optical light trapping and rear surface passivation. Adding the total loss to the measured J_{sc} of the champion Al-LBSF and Al-BSF solar cells yields a maximum generation current density of 43.8 mA/cm^2.

6.3.5   Fill factor (*FF*) loss analysis

The fill factor of most solar cells is reduced from the ideal diode limit by a combination of parasitic shunt (R_{sh}) and series (R_s) resistances, non-ideal recombination, and localised areas of high recombination. In non-optimized solar cells, the shunt resistance R_{sh} may also significantly impact the *FF*. Using the *FF* loss analysis method from Khanna *et al.* the *FF* losses were quantified [222]. In Figure 6.8, the *FF* losses are shown in absolute percentage points. The R_s was determined from the dark *J-V* and one-sun *J-V* curves, giving 0.58 Ωcm^2 for the champion Al-LBSF cell with spatial ALD Al$_2$O$_3$ and 0.47 Ωcm^2 for the Al-BSF cell [223]. R_{sh} was determined from the slope of the dark *J-V* curve near 0 V and was found to be larger than 10,000 Ωcm^2 for both solar cells.

Using the finite-element analysis software Griddler$^©$ 2.5, the contribution of the effective rear contact resistance for the Al-LBSF cells (with a contact pitch of 0.85 mm and a contact width of 40 µm) was determined to be 0.11 Ωcm^2 [224]. This difference matches that of the measured R_s for the Al-LBSF and Al-BSF cells. It is worthy to note that the measured R_s values are very low for both cells, which suggests that the front and rear metal contact resistances are very small [225]. On the other hand, the second

diode impact on the fill factor was found to be higher for the champion Al-LBSF solar cell as compared to the reference Al-BSF solar cell. This is consistent with the saturation current density (J_{02}) values determined in Section 6.3.3 and warrants further investigation of the processing conditions that lead to this higher second diode recombination.
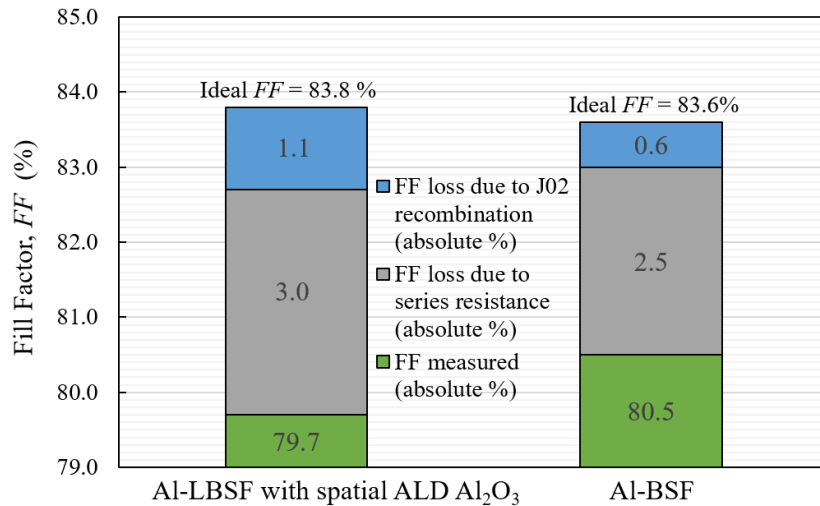
Figure 6.8 Graphical breakdown of the fill factor (FF) loss for the champion Al-LBSF solar cell with ALD Al₂O₃ and the reference Al-BSF solar cell. The magnitude of the FF loss due to each component is shown in absolute %.

6.4   Chapter Summary

In this chapter, aluminium local back-surface-field (Al-LBSF) solar cells were fabricated using Al₂O₃ films synthesised by spatial ALD (using low-cost solar-grade TMA) as the rear surface passivating dielectric along with standard back-surface-field (Al-BSF) solar cells. The *J-V* characteristics show a superior performance for the Al-LBSF cells, with the champion cell having a conversion efficiency of 20.1 % as compared to 19.2 % for the Al-BSF cells. A statistical analysis showed that this difference is attributed to the high V_{oc} and J_{sc} obtained for the Al-LBSF cells with spatial ALD Al₂O₃ as compared to the Al-BSF cells. A detailed loss analysis of the V_{oc} revealed a much lower saturation current density for the Al-LBSF cell with spatial

ALD Al_2O_3 indicating lower recombination at its rear surface which explains its higher V_{oc}. Optically, the ALD Al_2O_3 films demonstrated higher internal reflectance as compared to the Al-BSF cell. An analysis of the J_{sc} loss components displayed higher parasitic absorption and base collection losses for the reference Al-BSF cell, a result of its full-area rear metal contact. This explains the ~1.2 mA/cm^2 difference in the measured J_{sc} of the two cells. On the other hand, the Al-BSF cell displayed a slightly higher *FF* (80.5 %) as compared to the champion Al-LBSF cell (79.7 %). A *FF* loss analysis showed that this was due to a higher J_{02} recombination and series resistance for the Al-LBSF cell. This work demonstrates the application of spatial ALD Al_2O_3 films fabricated with low-cost solar-grade TMA precursors as the rear passivating dielectric in Al-LBSF solar cells.

Chapter 7: Application of spatial ALD Al$_2$O$_3$ in *n*-type bifacial solar cells

7.1 Introduction

The bulk material quality of silicon wafer solar cells is an important factor in pursuit of even higher solar cell efficiencies. In this regard, the relative tolerance of *n*-type c-Si to the most common metallic impurities (e.g. Fe) results in potentially higher minority carrier lifetimes as compared to *p*-type c-Si substrates with a similar impurity concentration [226]. Furthermore, *n*-type c-Si does not suffer from the boron-oxygen related light-induced degradation (LID), which is known to affect *p*-type c-Si solar cells [227].

As a result, solar cell concepts based on *n*-type c-Si show a high potential for achieving very high efficiencies. To realise this potential, a technology for adequate passivation of the p^+-type emitter is essential and has proven to be quite challenging in the past. As discussed in Chapter 2 (Sections 2.2.2 and 2.3.1), negatively charged Al$_2$O$_3$ is an ideal candidate for the passivation of p and p^+ surfaces because it forms an accumulation layer at the *p*-type c-Si surface, resulting in a high level of field-effect passivation. SiO$_x$ and a-SiN$_x$:H films are not ideal for the passivation of *p*-type and p^+-type Si due to their positive fixed charge density which can even result in inversion conditions at the *p*-type c-Si surface. In 2007, Hoex *et al.* reported excellent emitter saturation current density (J_{0e}) as low as 10 fA/cm^2 for planar p^+ emitters passivated with Al$_2$O$_3$ synthesised by plasma-assisted ALD [68]. Al$_2$O$_3$ films fabricated by ALD have also successfully passivated p^+ emitters of *n*-type high-efficiency PERL Si wafer solar cells, resulting in efficiencies of 23.9 % [70]. These results were obtained using a laboratory-type ALD system which is not directly transferable to mass production.

In this chapter, Al$_2$O$_3$ fabricated by a commercial high-throughput spatial ALD system was used for the passivation of the p^+ emitter in an n-type bifacial front and back contact (nFAB) Si wafer solar cell. A stack of a thin Al$_2$O$_3$ grown by spatial ALD using low-cost solar grade TMA precursor (see Chapter 3) capped by a-SiN$_x$:H layer was used to passivate the front p^+ surface and also served as an anti-reflective coating. An SiO$_x$/a-SiN$_x$:H stack at the rear passivates the n^+ BSF.

7.2   Solar cell fabrication process

Monocrystalline pseudo-square large-area 156 mm $\times$ 156 mm, n-type (3 Ωcm, 180 µm) Cz Si wafers pre-textured by China Sunergy were used for the fabrication of the nFAB solar cells of this work. The wafers were first chemically cleaned using the standard RCA clean [154] before the deposition of a 60 nm thick SiO$_x$ and 100 nm thick SiN$_x$ mask on the rear surface by PECVD (MAiA, Meyer Burger). They then underwent a short dip in 1 % HF acid/DI water solution before boron diffusion (p^+ homogenous emitter, 60 Ω/sq.) in a 4-tube diffusion furnace (QUANTUM, Tempress). The boron silicate glass (BSG) formed on the front surface during the diffusion process was removed together with the SiO$_x$/SiN$_x$ mask on the rear surface using a hot (40 ºC) 10 % HF solution. A 60 nm thick SiO$_x$ and 100 nm thick SiN$_x$ masking stack was then deposited on the front (p^+) surface. After a short dip in 1 % HF solution to remove any wrap-around mask, the samples underwent a phosphorus diffusion (n^+ BSF, 50 Ω/sq) in a different tube of the Tempress diffusion furnace. The phosphorus silicate glass (PSG) on the rear surface and the SiO$_x$/SiN$_x$ mask on the front surface were removed in a room temperature 10 % HF solution. The samples were cleaned using a full RCA wet-chemical followed by a final 1 % HF dip to ensure a H-terminated surface. For the front passivation stack, 10 nm of Al$_2$O$_3$ was deposited by spatial ALD (InPassion LAB, SoLayTec) on the front surface using solar-grade TMA. This Al$_2$O$_3$ was capped with

70 nm of a-SiN$_x$:H deposited by PECVD while at the rear, 30 nm of SiO$_x$ was capped with 70 nm of a-SiN$_x$:H also using PECVD. The a-SiN$_x$:H layers on the front and rear act as ARC for these bifacial solar cells. Figure 7.1 presents the fabrication steps and a schematic of the nFAB solar cell structure.

156 mm × 156 mm, 3 Ωcm *Cz*-Si, pre-textured wafers

01	Full RCA Clean
02	Rear 60 nm PECVD SiO$_x$ Mask
03	Rear 100 nm PECVD SiN$_x$ Mask
04	Short 1% HF Dip
05	Back-to-back BBr3 (60 Ω/sq)
06	Hot 10% HF dip (Mask + BSG Etch)
07	Front 60 nm PECVD SiO$_x$ Mask
08	Front 100 nm PECVD SiN$_x$ Mask
09	Short 1% HF Dip
10	Front-to-front POCl$_3$ diffusion (50 Ω/sq)
11	Room temperature 10% HF dip (Mask + PSG Etch)
12	Full RCA Clean
13	10 nm ALD Al$_2$O$_3$ (front)
14	70 nm Front PECVD Capping SiNx
15	30 nm Rear PECVD SiOx
16	70 nm PECVD Rear Capping SiNx
17	Screen print & dry (rear)
18	Screen print & dry (front)
19	Co-firing contacts
20	Laser-edge isolation

Figure 7.1 Process steps (left) for fabrication of the nFAB solar cell structure (right) using 10 nm thick spatial ALD Al$_2$O$_3$ for the passivation of the front p$^+$ emitter.

In addition, symmetrical test structures with boron-doped ($p^+/n/p^+$) and phosphorus-doped ($n^+/p/n^+$) surfaces on both sides were fabricated with identical passivation stacks (Al$_2$O$_3$/SiN$_x$ for p^+ and SiO$_x$/SiN$_x$ for n^+) to isolate the surface passivation properties of the individual front and rear surface in the nFAB solar cell. Fingers and busbars (5-busbar configuration) were screen printed (Eclipse, DEK) onto the front and rear using p^+ contacting and n^+ contacting Ag pastes, respectively. The contacts were dried and co-fired at 850 ℃ (peak set-temperature) in a fast firing furnace (SinTerra, BTU). Finally, all the fabricated solar cells were edge isolated using a picosecond laser (ILS500LT, InnoLas) to minimise parasitic shunts between the front and rear surfaces.

7.3   Results and Discussion

7.3.1   Effective carrier lifetime (τ_{eff}), implied open-circuit voltage (iV_{oc}) and emitter saturation current density (J_{0e})
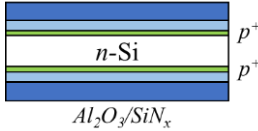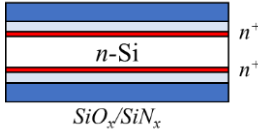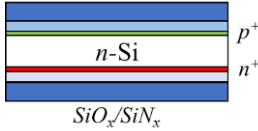
The effective carrier lifetime τ_{eff} for passivated symmetrical and asymmetrical 'lifetime samples' was measured using the quasi-steady-state photoconductance decay (QSSPC, WTC-120, Sinton) method that was described earlier in Section 3.2.1. The implied open-circuit voltage (iV_{oc}) of the samples was extracted from the QSSPC data according to [36]:

$$iV_{oc} = \frac{kT}{q} ln \left(\frac{[\Delta n + N_{dop}] \Delta n}{n_i^2} \right) \tag{7.1}$$

where Δn is the excess carrier density, k the Boltzmann constant, T the temperature, q the elementary charge, N_{dop} the bulk doping concentration, and n_i the intrinsic carrier density. The measured τ_{eff} at a carrier injection level of 1×10^{15} cm^{-3}, the iV_{oc} at 1 sun and the emitter saturation current density J_{0e} (as defined in Chapter 2, Sect. 2.2.2) for symmetrical $SiN_x/Al_2O_3/p^+/n/p^+/Al_2O_3/SiN_x$ samples, $SiN_x/SiO_x/n^+/n/n^+/SiO_x/SiN_x$ samples and asymmetrical $SiN_x/Al_2O_3/p^+/n/n^+/SiO_x/SiN_x$ (just before Step 17) samples are presented in Table 7.1.

The symmetrical Al_2O_3/SiN_x passivation on p^+ samples showed a much lower J_{0e} value (39 fA/cm²) as compared to symmetrical SiO_x/SiN_x passivation on n^+ (280 fA/cm²). It is likely that the SiO_x layers fabricated in this study require further optimisation. Consequently, the asymmetrically passivated samples (that will later be metallized to make the solar cell) show relatively low τ_{eff}, iV_{oc} and higher J_{0e} values, most likely dominated by the poorly passivated rear n^+ BSF surface. This is attributed to the non-optimised deposition process of the SiO_x/SiN_x stack in this study.

Table 7.1 Effective carrier lifetime, implied V$_{oc}$ and J$_{0e}$ of carrier lifetime samples.

Sample type (nCz-Si, 3 Ωcm)	τ_{eff} at 1×10^{15} cm^{-3}, (µs)	iV_{oc} at 1 sun, (mV)	J_{0e} (fA/cm^2)
Al$_2$O$_3$/SiN$_x$ p^+ *n*-Si p^+ *Al$_2$O$_3$/SiN$_x$*	293	669	39
SiO$_x$/SiN$_x$ n^+ *n*-Si n^+ *SiO$_x$/SiN$_x$*	82	628	280
Al$_2$O$_3$/SiN$_x$ p^+ *n*-Si n^+ *SiO$_x$/SiN$_x$*	102	626	275

7.3.2   Current density-voltage (*J-V*) characteristics

The current density-voltage (*J-V*) characteristics of the fabricated nFAB solar cell batch measured at one Sun is presented in Table 7.2. The champion solar cell had an energy conversion efficiency of 19.8 % when measured with the front p^+ side illuminated. The average batch efficiency for a total of 42 samples was 19.1 %. This respectable conversion efficiency is a result of reasonably high short-circuit current (J_{sc}) of ~38 mA/cm^2, implied open-circuit voltage (iV_{oc}) of 645 mV and fill factor (*FF)* of ~79 %.

A quantitative treatment of various losses enables a comparison of this cell with the state of the art. Firstly, the V_{oc} presents a significant scope for improvement when compared to reported values of > 700 mV [70, 124]. From the QSSPC values, we see that reasonably low J_{0e} values of ~40 fA/cm^2 were obtained for the p^+ layer but values as high as ~280 fA/cm^2 were obtained for the n^+ layer. A high J_{0e} of the asymmetrical solar cell precursor of ~275 fA/cm^2 suggests that the poor surface passivation at the rear n^+ surface dominates recombination. Optimisation of the rear surface passivation

stack of SiO$_x$/SiN$_x$ is suggested to achieve higher V_{oc} values (outside the scope of this thesis). Series resistance (R_s) values of 0.5 – 0.7 Ωcm^2 and very high shunt resistance (R_{sh}) values contribute to the relatively high *FF* and compare well to published state-of-the-art values. A detailed loss analysis of the *FF* and the J_{sc} is conducted in following sections to identify areas of improvement for these parameters.

Table 7.2 One-Sun I-V parameters of nFAB solar cells using low-cost ALD Al$_2$O$_3$/SiN$_x$ as the front passivation stack.

	η (%)	V_{oc} (mV)	J_{sc} (mA/cm^2)	*FF* (%)	R_s (Ωcm^2)	R_{sh} (Ωcm^2)
Best cell (p$^+$ side)	19.8	645.7	38.4	79.7	0.47	> 10,000
Batch average (p$^+$ side)	19.1	641.2	38.1	78.0	0.71	> 10,000

7.3.3   Photoluminescence (PL) and electroluminescence (EL) imaging

The spatial electrical uniformity of the champion nFAB solar cell were evaluated using (a) PL imaging at one-Sun open-circuit conditions, (b) EL imaging in the dark by passing a forward current of 9 mA/cm^2 (see Section 6.3.2) and (c) series resistance imaging derived from a series of PL and EL images [217]. These are shown in Figure 7.2 for the champion nFAB solar cell (η = 19.8%) fabricated in this work.
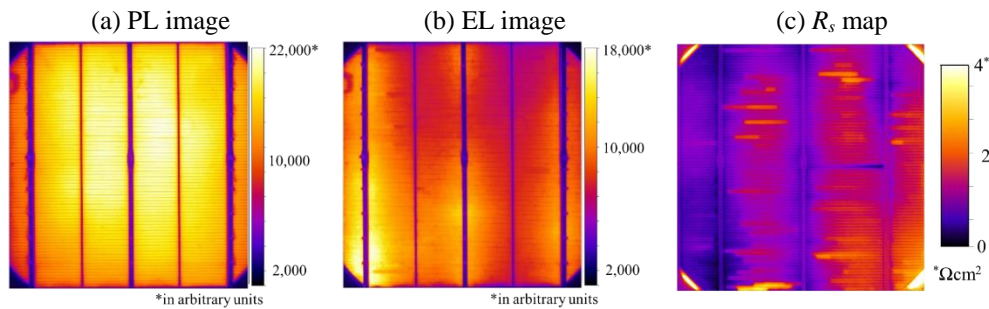
Figure 7.2 (a) Photoluminescence (PL), and (b) electroluminescence (EL) and (c) derived R$_s$ map of the champion nFAB solar cell with 19.8% efficiency passivated at the front with a ALD Al$_2$O$_3$/SiN$_x$ stack and on the rear with a SiO$_x$/SiN$_x$ stack.

The PL image has a very good spatial uniformity reflecting the electronic uniformity of the silicon wafer solar cell. The EL image display some non-uniformity with darker

areas indicating higher local series resistance. This is consistent with the R_s image that indicates areas of higher (brighter) R_s due to finger interruptions and a few local shunts. As expected, the cell regions along the front busbars have the lowest values for R_s which generally increase with increasing distance from the busbars [221].

7.3.4 Short-circuit current density (J_{sc}) and fill factor (FF) loss analysis

The weighted integral of the short-circuit current density (J_{sc}) loss components for the champion solar cell is shown in Figure 7.3 (a). The J_{sc} loss components consist of blue loss (due to ARC absorption and imperfect emitter collection), ARC reflectance, front surface escape (light reflected from the solar cell rear that escapes via the front surface), near-infrared (NIR) parasitic absorption (predominantly at the cell rear) and base collection loss (recombination in the bulk). A very low blue loss component of 0.274 mA/cm^2 indicates that the front Al$_2$O$_3$/SiN$_x$ dielectric stack was non-absorbing and that the front emitter is shallow. The largest J_{sc} loss was obtained from NIR parasitic absorption (the bifacial sample was placed on a reflective metallic chuck) indicating potential for improvement of the rear n^+ BSF diffusion profile and passivating SiO$_x$/SiN$_x$ stack.

(a)

(b)
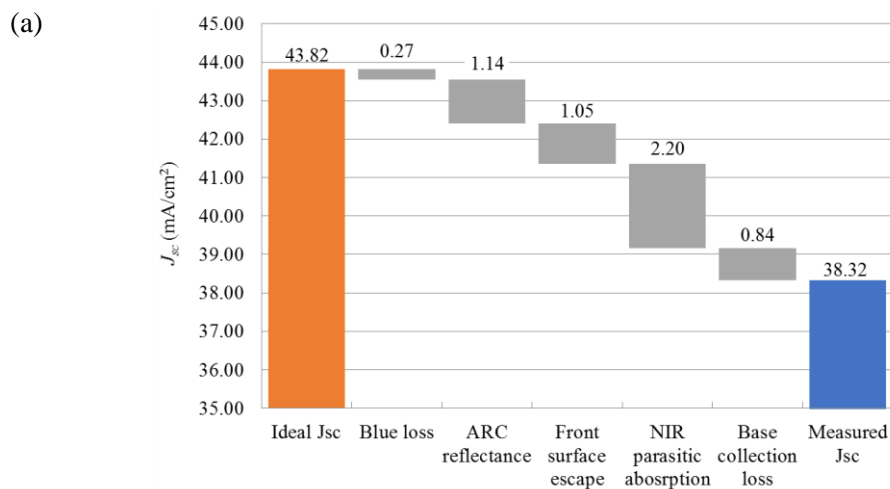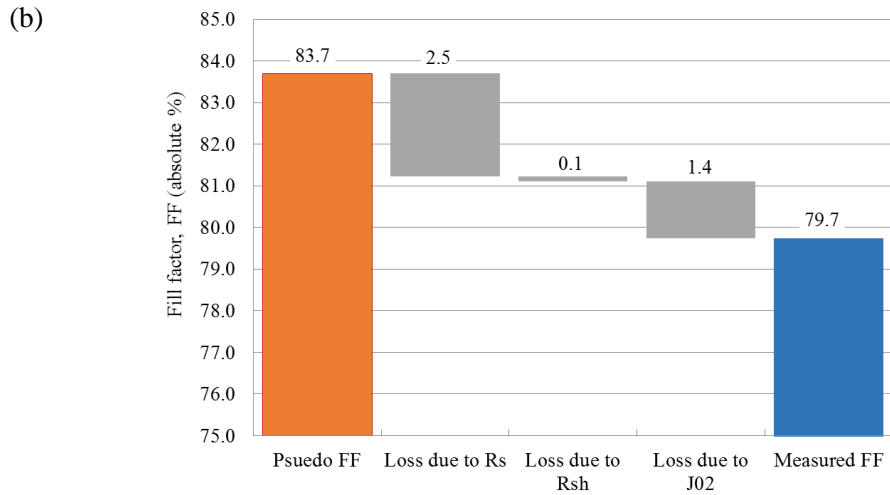
Figure 7.3 Graphical breakdown of the (a) weighted integral of short-circuit current (J_{sc}) and (b) fill factor (FF) loss components for the champion nFAB solar cell with 19.8% efficiency fabricated in this work.

The *FF* loss components (in absolute %) due to series resistance (R_s), non-ideal recombination (J_{02}), and shunt resistance (R_{sh}) are shown in Figure 7.3 (b). The largest loss in *FF* of ~2.5 % is due to the cell R_s (measured value of 0.5 Ωcm²). This is attributed to the lateral resistance of the p^+ and n^+ doped layers (total of 0.34 Ωcm²) as determined by a breakdown of R_s components in Figure 7.4 [222]. On the other hand, the metal contact resistance and finger and busbar line resistances at the front and rear contribute a total of 0.14 Ωcm².
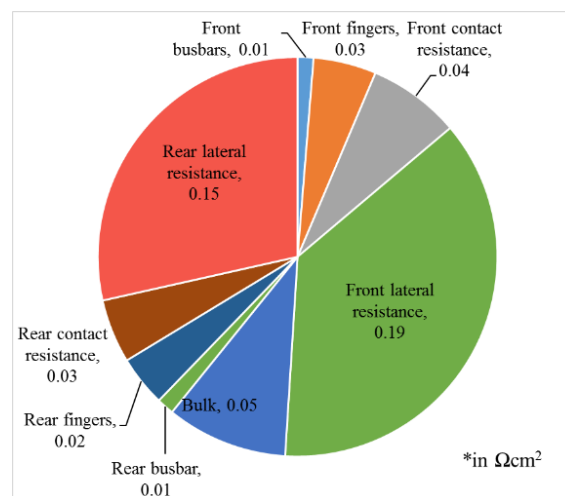
Figure 7.4 Gaphical representation of the series resistance R_s components (arising from the front and rear contacts as well as the Si bulk for the 19.8% champion nFAB cell).

128

7.4   Chapter Summary

In summary, a low-cost high-throughput spatial ALD technique was used to deposit 10 nm thin Al$_2$O$_3$ films for the passivation of the heavily-doped p^+ front surface of *n*-type bifacial nFAB silicon solar cells. A champion cell efficiency of 19.8 % was obtained, with an average batch efficiency of 19.1 %. Carrier lifetime measurements revealed a low J_{0e} of 39 fA/cm^2 for samples symmetrically passivated with Al$_2$O$_3$/SiN$_x$ stacks while samples symmetrically passivated by the SiO$_x$/SiN$_x$ stacks deposited in this study showed a much higher J_{0e}. Hence, the relatively low V_{oc} of the complete nFAB solar cells is attributed to the poor passivation quality of the non-optimized rear SiO$_x$/SiN$_x$ stack. This was also reflected in the J_{sc} loss analysis which revealed high NIR parasitic absorption at the rear surface. An analysis of the *FF* loss components showed a relatively low R_s contribution from the contact and line resistances and a dominant contribution from the lateral resistance of the doped p^+ and n^+ Si layers.

Chapter 8: Application of spatial ALD ZnO:Ga films as a TCO in HET solar cells

8.1 Introduction

In this chapter, the role of TCOs in a-Si:H/c-Si (HET) solar cells is discussed. In conventional homojunction Si solar cells, lateral conduction of charge carriers takes place via highly-doped n^+ and p^+ Si regions that directly contact metal. However, in HET solar cells, doped a-Si:H layers are used to achieve selectivity for the extraction of charge carriers. These doped a-Si:H layers display relatively poor lateral conductance. To improve lateral carrier conductance in HET solar cells TCO thin films are added on both sides, between the doped a-Si:H layers and the metal grid [145].

The intrinsic and doped a-Si:H layers in HET cells degrade at high temperatures (> 200 ºC) due to H-effusion [228]. Hence, low-temperature conditions are required for the deposition of the TCO film on the a-Si:H layers. Furthermore, since the a-Si:H layers are relatively thin (< 30 nm), a low-impact TCO deposition technique that does not involve any high-energy ions is desired. ALD fulfils these conditions demonstrating a high potential for use in the fabrication of HET solar cells. The current world record efficiency for HET silicon solar cells is 25.6 % (achieved by Panasonic Corporation), the highest for any Si cell structure and approaching the fundamental limit of 29.4% for Si solar cells [20, 229]. However, it is not disclosed whether ALD was used in this specific solar cell.

TCO materials are required to be conductive and at the same time transparent, as discussed in Section 2.3.2. In_2O_3-based TCOs (e.g. In_2O_3:Sn or ITO) demonstrate excellent conductance and transparency and hence are a popular choice for application in HET solar cells. However, ITO films are expensive owing to the ever increasing

price of the rare element indium [230]. Furthermore, they are typically synthesised by sputtering which leads to plasma-induced damage of the underlying thin a-Si:H layers, thereby reducing the level of surface passivation [178]. ZnO-based TCOs are a low-cost In-free alternative. However, ZnO-based TCOs show poorer electrical properties than In_2O_3-based TCOs, especially due to low values of the carrier mobility (< 15 cm^2/Vs). On the other hand, they are more transparent due to a lower extinction coefficient [231]. In addition to conductance and transparency considerations, the work function φ of the TCO material is of importance. The front TCO contacting the a-Si:H (p^+) layer should preferably have a value greater than or equal to the φ of the doped a-Si:H layer (i.e. ~5.3 eV). On the other hand, the φ of the TCO contacting the a-Si:H (n^+) layer should preferably be less than or equal to ~4.2 eV [232]. A mismatch in φ leads to a Schottky-type contact between the doped a-Si:H/TCO layer, and the associated depletion region can extend into the Si wafer and reduce band bending. This affects the fill factor as well as the open-circuit voltage [79, 233, 234]. The φ of a doped degenerate TCO is determined by its electron affinity χ and the Burstein-Moss shift [235]. Since χ for ZnO (~4.4 eV) is lower than for In_2O_3 (~5.0 eV), ZnO is possibly more suited to contact the a-Si:H (n^+) whereas In_2O_3 is more suited for the front a-Si:H (p^+) layer [79]. Together with less stringent requirements on transparency at the rear side of the cell (in the case of front emitter, monofacial HET cells), it appears that ZnO-based TCOs are more likely to be an effective low-cost replacement for ITO at the rear.

In fact, it has recently been shown that ZnO:Al can replace ITO at the rear of HET solar cells with no detrimental effect on the solar cell efficiency [231]. In Chapter 5 of this thesis, ZnO:Ga (GZO) films grown by the low-cost high-throughput spatial ALD technique were developed which demonstrated low resistivities (~2×10^{-3} Ωcm) and high transparency. In the present chapter, HET solar cells with GZO films as the TCO are compared to conventional HET cells with sputtered ITO. We also compare the performance of HET cells with GZO as the rear TCO and ITO as the front TCO.

8.2 Process steps for fabrication of HET solar cells

For this study, pre-processed large-area 156 mm × 156 mm, textured *n*-type Cz-Si (3 Ω.cm, 150 µm) samples were used with the intrinsic (*i*) and doped (*p⁺* and *n⁺*) a-Si:H layers fabricated at the Centre Suisse d'Electronique et de Microtechnique SA (CSEM, Neuchatel)[12]. The a-Si:H (*ip⁺*) and a-Si:H (*in⁺*) front and rear stacks were 22 nm thick with a bandgap of 1.74 – 1.79 eV as measured using spectroscopic ellipsometry on planar control wafers. The GZO films were deposited by spatial ALD (InPassion LAB, SoLayTec), as discussed in detail in Chapter 5 of this thesis. All samples were deposited at a substrate temperature of 230 ℃ with a precursor (diethylzinc + trimethylgallium) partial pressure of 2 mbar and a H_2O partial pressure of 65 mbar corresponding to a dopant Ga/(Zn+Ga) ratio of 6.8%. This ratio yielded the lowest resistivity for GZO deposited at 230 ℃ (as seen in Chapter 5). A substrate temperature of 250 ℃ lowers the resistivity further. However, it also significantly degrades the a-Si:H layers and hence is avoided in this work. ITO was deposited using an inline magnetron sputtering system (Line 540, FHR Anlagenbau) at 200 ℃ with a plasma power of 1.5 kW, Ar gas flow of 122 sccm and O_2 gas flow of 3 sccm and an ITO (In_2O_3:Sn) sputter target. The electrical properties of the ITO and GZO films fabricated in this study are presented in Table 8.1. For the TCO deposition, the a-Si:H/c-Si samples were divided into four groups, as detailed in Figure 8.1 and Table 8.2, with various combinations for the front and rear TCO.

Table 8.1 Electrical properties of fabricated ZnO:Ga (GZO) and In_2O_3:Sn (ITO)

TCO material	Deposition technique	Deposition temperature	Resistivity, ρ (Ωcm)	Carrier concentration, N_c (cm^{-3})	Carrier mobility, μ_c (cm^{2}V^{-1}s^{-1})
GZO	Spatial ALD	230 ℃	3×10^{-3}	5.2×10^{20}	2.5
ITO	Sputter	200 ℃	0.6×10^{-3}	3.5×10^{20}	37

---

[12] The facilities at CSEM were used due to the unavailability of lab equipment at SERIS (NUS) during the period Aug, 2012 – March, 2016,
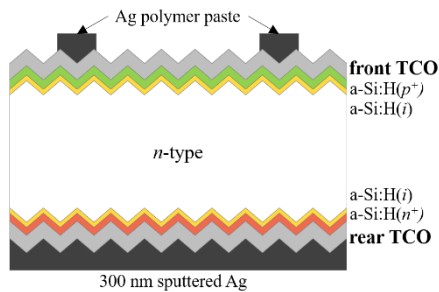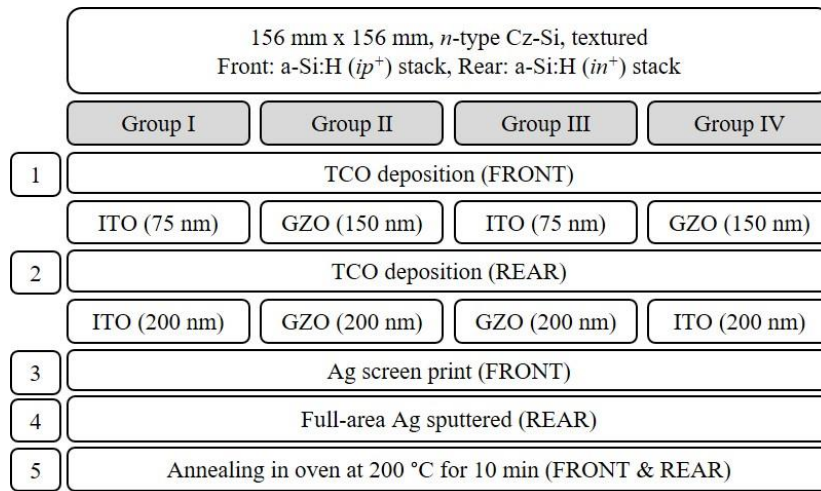
Table 8.2 Description of groups in this study

Group	Front TCO	Rear TCO
I	75 nm ITO	200 nm ITO
II	150 nm GZO	200 nm GZO
III	75 nm ITO	200 nm GZO
IV	150 nm GZO	200 nm ITO

Figure 8.1 (Top) Schematic representation of all process steps, (left) schematic illustration of an a-Si:H/c-Si (HET) monofacial solar cell and (right) a description of the front and rear TCO material and thickness for the different groups of HET cells fabricated in this study. The TCO thickness was estimated from measurements on planar samples. The increase in area on a textured surface is taken into account for the sputtered ITO.

Due to the high resistance of GZO films for thicknesses < 100 nm (as discussed in Section 5.6), a GZO thickness of 150 nm was chosen for the front. This was based on a simulation of the trade-off between the losses in the generated photocurrent (as a result of thicker front GZO) versus the loss in the fill factor (as a result of higher resistance for thinner GZO). The simulated efficiency is presented in Figure 8.2. Ag was then sputtered onto the rear surface of all the samples and a front grid consisting of 83 fingers and 5 busbars was screen-printed onto the front using a low-temperature Ag-polymer paste. All samples were then annealed for 20 mins at 200 ºC to dry and sinter the paste, to improve conductivity.
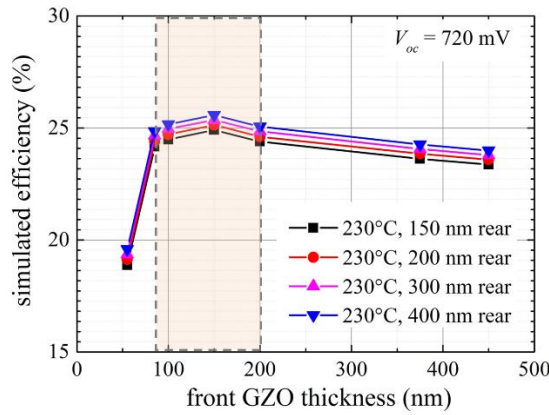
Figure 8.2 Simulated HET cell efficiency as a function of front ZnO:Ga (GZO) thickness for increasing rear thickness. The photocurrent density was simulated using OPAL2 and the fill factor loss estimated using an equivalent two-diode circuit model [203, 222]. V_{oc} of 720 mV and a full-area rear contact were assumed. The optimum thickness window is indicated by the shaded area.

8.3   Results and Discussion

8.3.1   Effective carrier lifetime τ_{eff} and implied open-circuit voltage iV_{oc}

The effective carrier lifetime and iV_{oc} of the HET solar cell samples before and after TCO deposition are presented in Table 8.3. The iV_{oc} is obtained using the method described in Section 7.3.1. The percentile difference in iV_{oc}, calculated as $\Delta = (iV_{oc,bef} - iV_{oc,aft}) / (iV_{oc,bef}) \times 100$, is also shown.

Table 8.3 Effective carrier lifetime (τ_{eff}) and implied V_{oc} (iV_{oc}) for the different groups of HET cell samples (2 per group) before and after TCO deposition.

Group	τ_{eff} at 1×10^{15} cm^{-3} (μs)		iV_{oc} at 1 sun (mV)		Δ_{iVoc}
	Before TCO	After TCO	Before TCO	After TCO	
I	4390	2780	749.1	739.1	1.3%
	4580	3240	747.8	738.5	1.2%
II	5200	3740	749.3	745.8	0.5%
	4070	1930	745.2	737.4	1.05%
III	4040	2320	746.9	735.9	1.5%
	5300	3540	749.2	739.7	1.3%
IV	3770	2140	745.3	736.6	1.2%
	5780	3910	749.3	737.7	1.55%

All the partially processed HET samples displayed a degradation after TCO deposition. It is worthwhile to note here that, in general, a degradation is expected for sputtering due to surface damage from high-energy plasma species. However, no degradation is expected during the 'softer' ALD process. However, a degradation is still observed and

this is attributed to the chosen temperature of 230 ºC during ALD deposition, a temperature at which the a-Si:H layers are expected to degrade[13] [228]. Despite this, a slightly larger degradation is still observed for the sputtered samples (Groups I, III and IV) as compared to the samples with only ALD TCOs (group II).

8.3.2   3D optical profile of the screen-printed front fingers

In order to improve the line conductance of the screen-printed fingers, a double-print method was adopted whereby the fingers were printed twice. This resulted in a significant increase in finger height (from 12 µm to 25 µm) as seen in Figure 8.3 and a decrease in sheet resistance of the finger from 7.5 mΩ/sq to 6 mΩ/sq.
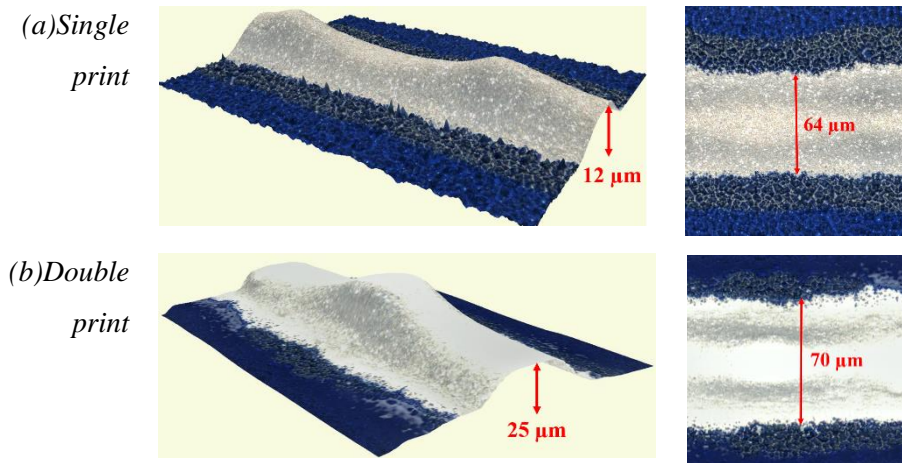
Figure 8.3 Optical images (3-dimensional and top views) of screen-printed lines after a single print and after a double print. A significant increase in finger height was obtained for the double-printed lines with only a small increase in finger width.

8.3.3   HET cell current-voltage parameters

The current density-voltage (*J-V*) parameters of the finished metallized and annealed HET solar cells is summarized in Table 8.4. The excellent surface passivation quality of the intrinsic a-Si:H layers is demonstrated by the very high V_{oc} values (> 700 mV) for all cells. A clear decrease in short-circuit current density (J_{sc}) is observed for groups

---

[13] The extent of degradation depends on the total thermal budget which is influenced by temperature as well as the duration of heat exposure. In this work, each GZO deposition by ALD took approximately 10 mins.

II and IV. The reason for this current loss is the 150 nm thick GZO layer used as the front TCO in both groups. Furthermore, Groups II and IV also show significantly reduced fill factors *FF*. This is attributed to the higher sheet resistance and contact resistance of the front GZO layer compared to ITO as presented in Table 8.5. These resistive components contribute to the series resistance R_s, which is found to be high for all four groups and enormous for Groups II and IV. Since the rear has a full-area sputtered Ag contact, the influence of the rear TCO properties is found to be less than the front. Overall, Groups I and III show relatively better performance with cell efficiencies > 18% and a champion efficiency of 18.9 % for a cell with 75 nm ITO on the front and 200 nm GZO on the rear. For cells with 150 nm GZO on the front (i.e. groups II and IV), a champion cell efficiency of 16.6 % was achieved. The low *FF* in these groups is the main reason for their low efficiency and will be investigated in detail in the next sections.

Table 8.4 Summary of one –Sun I-V parameters of HET cells with different TCOs.

Group	V_{oc} (mV)	J_{sc} (mA/cm²)	*FF* (%)	η (%)	R_s (Ωcm²)	R_{sh} (Ωcm²)
I*	-	-	-	-	-	-
	734.0	35.9	71.3	18.8	2.57	9460
II	723.4	34.7	65.9	**16.6**	3.38	404
	719.0	34.7	63.5	15.8	4.05	488
III	729.0	35.4	72.3	18.6	2.14	729500
	730.4	35.6	72.7	**18.9**	2.13	45015
IV	727.9	34.6	60.0	15.1	5.80	2547
	726.0	34.4	63.0	15.8	4.72	1196

*Each group consisted of 2 cells. Due to breakage during process, Group I was left with only one cell for characterisation

Table 8.5 Summary of sheet resistance, contact resistance, and line resistance values for the front TCO material.

Front TCO material	Sheet resistance* (Ω/sq)	Contact resistivity, ρ_c (mΩcm²)	Front finger line resistance (mΩ/sq)
150 nm GZO	350 ± 50	~35	6.1
75 nm ITO	90 ± 15	~5	

*Measured TCO sheet resistance after annealing the cell at 200ºC for 20 minutes.

8.3.4   Electroluminescence and series resistance imaging

Electroluminescence (EL) images give us information regarding the electrical uniformity of the solar cell. Since photon emission increases with local voltage, regions with poor contact show up as dark areas in the image. An R_s image obtained from photoluminescence (PL) measurements shows areas of high (bright) and low (dark) R_s. The EL and R_s maps of the champion HET cell from each group are presented in Figure 8.4. The Group II and IV cells show local areas of poor electrical contact at equal intervals near the edges. This is a known side-effect of the ALD process due to contact with the runout belt at those points. A possibility to avoid this is currently under investigation by the manufacturer. The R_s images are consistent with the measured *J-V* parameters showing a higher overall R_s for Groups II and IV.
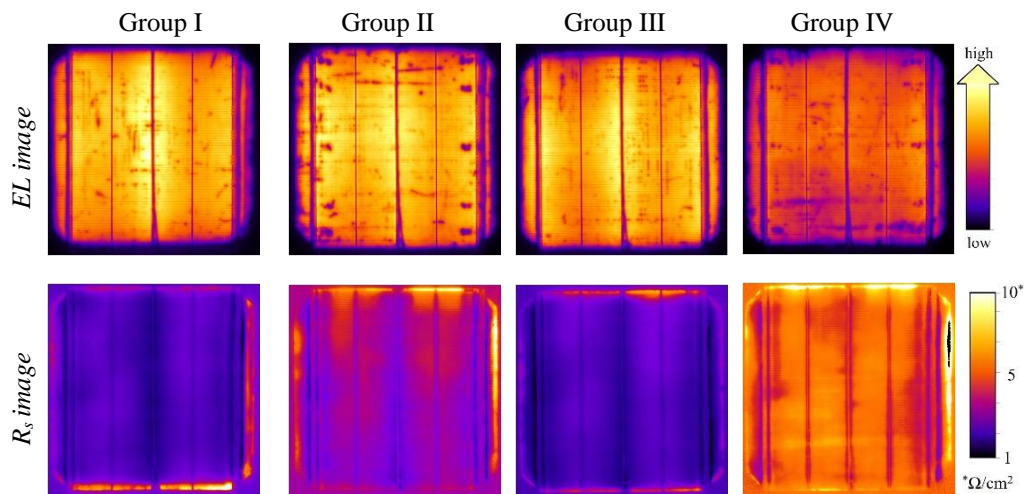
Figure 8.4 EL (top) and R_s (bottom) images of the best cells from Groups I-IV.

8.3.5   Loss mechanisms of the fabricated HET cells

The focus of this chapter is to investigate the potential of GZO films for application as a TCO in HET solar cells (for both surfaces or only for the rear) with ITO films as a reference. The *J-V* parameters showed that the influence of the rear TCO on R_s, *FF* and J_{sc} was not as high as the influence of the front TCO. Hence, in this section a detailed analysis of the loss components is conducted on the champion cells from Groups II and

III, which have the same rear TCO (200 nm GZO) but different front TCO of 150 nm GZO and 75 nm ITO, respectively. A loss analysis of *FF* components for these two cells is presented in Figure 8.5 (a) using the method described by Khanna *et alia* [222]. The largest *FF* loss contributor was found to be R_s for both groups. A further analysis of the R_s components is provided in Figure 8.5(b). The R_{sh} is also a major loss component for Group II while it is insignificant for Group III.
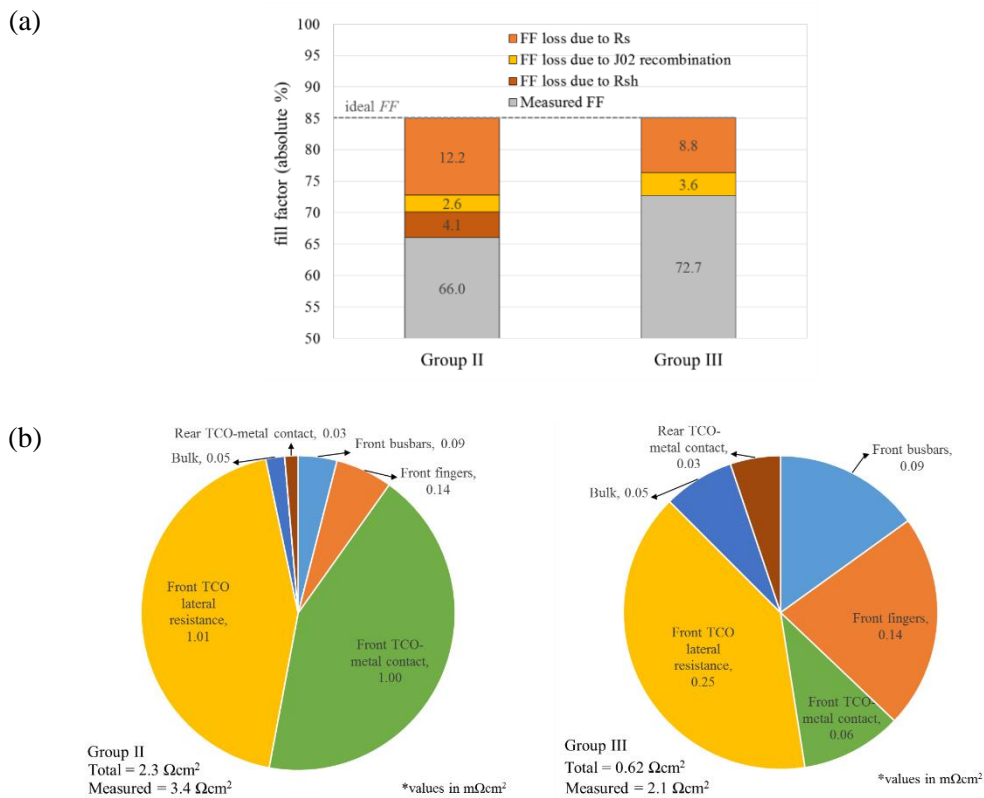
Figure 8.5 A representation of the fill factor loss components (top) and the R_s components (bottom) for the champion solar cells from Groups II and III.

The known contributors to R_s are the TCO lateral sheet resistance (which is much higher for GZO as compared to ITO), front grid components (fingers, busbars, TCO-metal contact resistance) and the resistance from the bulk Si wafer. These known components add up to 2.3 Ωcm^2 for Group II and 0.6 Ωcm^2 for Group III. Since the measured R_s values were much larger (3.4 and 2.1 Ωcm^2, respectively), there appears to be an unknown contributor to the R_s which is most likely the a-Si:H layers

(particularly, the resistive a-Si:H(*i*) layers) which are not accounted for in this analysis. This requires further investigation and is outside the scope of this thesis.

The external quantum efficiency (EQE) of the champion cells from Groups I, II, III and IV are presented in Figure 8.6.
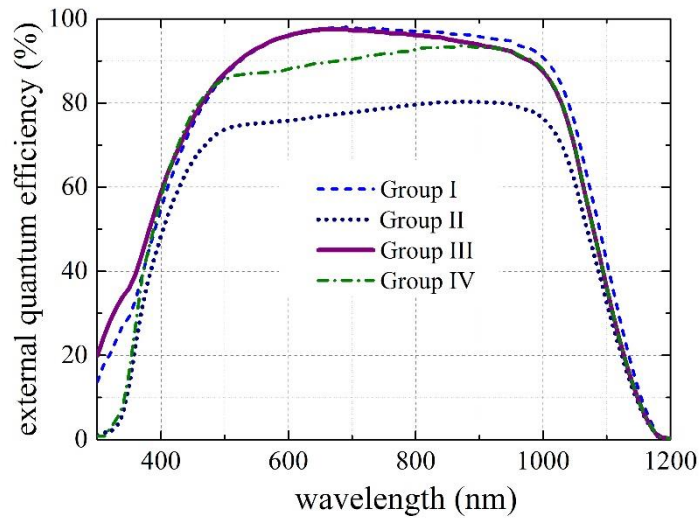
Figure 8.6 Measured external quantum efficiency (EQE) curves for the champion cells from Group I, II, III and IV. The EQE measurements used a bias light intensity of 0.4 suns.

A significant difference in the EQE curves is observed for cells from groups II (150 nm GZO front, 200 nm GZO rear) and IV (150 nm GZO front, 200 nm ITO rear) as compared to groups I (75 nm ITO front, 200 nm ITO rear) and III (75 nm ITO front, 200 nm GZO rear). The difference in the blue-green wavelength range up to 750 nm is attributed to the increased parasitic absorption in the thick front GZO layer and is reflected in the HET cells' J_{sc} values [236]. The differences in the EQE curves at the near-infrared wavelength regions (750 – 950 nm) reflect the optical properties of photons in the c-Si wafer base since these photons do not penetrate deep enough to reach the rear surface of the cell. The EQE curve for group II is found to be much lower than the rest. This observation is supported by a comparison of the V_{oc} of both cells (723 mV for group II and 730 mV for group III). The drop in V_{oc} for Group II is attributed to a low R_{sh} values of ~400 Ωcm^2. The reason for the low R_{sh} is the presence

of wrap-around GZO after deposition. Laser edge isolation can be used to solve this issue.

8.4   Chapter Summary

ZnO:Ga (GZO) films fabricated using spatial ALD were applied as TCO in monofacial a-Si:H/c-Si HET solar cells. Due to the high resistance of GZO films with thickness <100 nm, a thickness of 150 nm was tested as the front TCO and a thickness of 200 nm as the rear TCO. HET cells with ITO (on both surfaces and in combination with GZO) were also fabricated for comparison. A champion efficiency of 18.9 % was achieved for a HET cell with 75 nm ITO as the front TCO and 200 nm GZO as the rear TCO. No conversion efficiency loss was observed when using GZO at the rear instead of ITO. However, using GZO as the front TCO results in significant *FF* and J_{sc} losses. This work demonstrates the potential of using the lower-cost GZO films to replace ITO at the rear of commercial HET solar cells using the industrially scalable spatial ALD technique for fabrication.

Chapter 9: Summary, original contributions and proposed future research

9.1   Thesis Summary

This thesis presented the development and analysis of functional thin films deposited with a relatively new technique for application in c-Si photovoltaics: spatial atomic layer deposition. Functional thin films play a critical role in nearly all types of c-Si solar cells and the conversion efficiency is strongly influenced by the quality and performance of these films. ALD presents many advantages as a film fabrication technique in the PV and semiconductor industries, due to the nature of its low-energy, 'soft' and self-limiting surface reactions that result in uniform and conformal monolayer-by-monolayer growth. However, the relatively low throughput of the conventional (i.e., temporal) ALD method limits its cost-effective application in industry. The spatial ALD technique, where precursors are separated in space rather than in time, overcomes this limitation while retaining the advantages of ALD. In this thesis, Al_2O_3 and ZnO thin films were developed using spatial ALD and studied in detail for large-scale application in the PV industry. The main results from each chapter are briefly summarised below.

In addition to pushing for higher conversion efficiencies, there is a constant drive in the PV community towards lower-cost materials and cost-effective processing. Al_2O_3 films demonstrate excellent surface passivation properties on c-Si surfaces and are increasingly being used in the silicon solar cell industry. In Chapter 3, Al_2O_3 films were fabricated using a low-cost 'solar-grade' TMA precursor which has a higher impurity content but is only one tenth of the cost of the 'semiconductor-grade' precursor. A comprehensive investigation was carried out to compare the surface passivation

properties of Al_2O_3 films deposited using both precursors. It was found that the 'solar-grade' Al_2O_3 films perform as well as, if not even better, than the 'semiconductor-grade' precursors. Both precursors resulted in high effective minority carrier lifetimes of > 200 µs on *p*-type and > 2,000 µs on *n*-type Cz-Si substrates. Furthermore, the $D_{it,midgap}$ resulting from the solar-grade precursors was found to be lower than that of the semiconductor-grade precursors, for all investigated Al_2O_3 film thicknesses. On the other hand, the Q_{tot} of the 'semiconductor-grade' films was similar for both. A chemical analysis revealed a higher alkaline content in the 'solar-grade' films, however, this did not affect the surface passivation quality afforded by the films. Hence, it was demonstrated that the lower-cost 'solar-grade' TMA precursor is well suited for the fabrication of Al_2O_3 films in the PV industry.

TCOs are another important category of functional thin films actively used in the PV community. Although ITO is a popular TCO material, ZnO has long been investigated as a lower-cost and non-toxic alternative. Furthermore, in thin-film solar cells, such as CIGS solar cells, a highly resistive layer of ZnO is often used to improve the cell performance. Conventional fabrication techniques for ZnO include sputtering, which involves high-energy species that often damage the solar cell surface. In Chapter 4, undoped ZnO films were fabricated by the low-damage spatial ALD technique and the growth and material characteristics were studied in detail. The ZnO films displayed very high resistivities, in contrast to ZnO films fabricated by temporal ALD. This difference was attributed to the extremely short precursor and purge durations of the spatial ALD technique as compared to temporal ALD. A higher resistivity is preferred for application in CIGS solar cells, and hence the ZnO films deposited by spatial ALD appear to be well suited for this purpose.

The ZnO films were doped with gallium in Chapter 5, with the aim to improve the conductance of the films for potential application as a TCO in heterojunction silicon wafer solar cells and thin-film solar cells. The ZnO:Ga (GZO) films displayed a

decrease in film resistance with increasing substrate temperature during deposition, with a minimum resistivity of ~2×10^{-3} Ωcm achieved at 250 °C deposition temperature. At a lower deposition temperature of 230 °C, a minimum of ~3.5×10^{-3} Ωcm was achieved for a Ga dopant concentration of 6.8 %. The resistivity was also found to increase significantly for film thicknesses below 100 nm. High carrier concentrations of up to 5.6×10^{20} cm^{-3} and relatively low carrier mobilities of ~3 cm^{2}V^{-1}s^{-1} were measured for the least resistive GZO films fabricated at 230 °C. The optical transparency of the films, as simulated using the measured refractive index extinction coefficient values, was found to be > 90 % throughout the visible and near-infrared wavelength regions. These properties indicated a good potential for application of GZO films as TCOs in heterojunction silicon wafer and thin-film solar cells.

In Chapters 6, 7 and 8, the functional thin films developed and studied in the earlier chapters were applied in homojunction and heterojunction silicon wafer solar cells, to test their influence on the cell performance. Al$_2$O$_3$ films fabricated by spatial ALD using the low-cost 'solar-grade' TMA precursor were used to passivate the rear surface of *p*-type Al-LBSF solar cells and the p^+ front emitter of nFAB solar cells. A very good conversion efficiency of 20.1 % was achieved for an Al-LBSF cell, and an efficiency of 19.8 % was achieved for an nFAB solar cell. In both cases the cost-effective Al$_2$O$_3$ films displayed good surface passivation quality, which contributed to the high conversion efficiencies. In Chapter 8, HET silicon wafer solar cells were fabricated using GZO films deposited by spatial ALD as the TCO. The HET cells with GZO at the front and rear revealed large electrical losses due to a high series resistance and increased parasitic absorption at the front. On the other hand, HET cells with ITO at the front and GZO at the rear performed very well, with a conversion efficiency of up to 18.9 %. This was on par with the reference cell with ITO at the front and rear. The improved performance was attributed to the better work function match of GZO with the n^+ a-Si:H as compared to ITO. This study indicates that low-cost GZO films

fabricated by industrially feasible spatial ALD can be used to replace the costly ITO at the rear for commercial HET solar cells.

Though application of the thin films developed in this work resulted in solar cells exhibiting good performance, the cell efficiencies achieved do not hold up to current state-of-the-art standards. Solar cell efficiencies are dependent on each of the various process steps used during fabrication. In order to attain higher solar cell efficiencies, it is crucial that each of the steps be completely optimized. Due to a severe fire at the labs where this work was conducted, all other processes were being reinstated concurrently with the development of the thin films and solar cells in this work. As such, not all the other process steps were optimized when the solar cells in this work were being fabricated.

9.2   Original contributions of this work

A brief summary of the author's original contributions in this thesis are listed below:

I.   The excellent surface passivation performance of Al_2O_3 films fabricated with the commercially scalable spatial ALD technique and using a highly cost-effective 'solar-grade' precursor was established. This corroborates the replacement of the more expensive semiconductor-grade precursor by the solar-grade precursor in the silicon PV industry.

II.   The low-cost Al_2O_3 films fabricated by spatial ALD were applied in *p*-type and *n*-type homojunction silicon wafer solar cells to test their performance at the device level. High conversion efficiencies of up to 20.1% and 19.8%, respectively, were achieved for the *p*-type and *n*-type cells, demonstrating the excellent performance of these films for future applications.

III.   Undoped ZnO films with unusually high resistivity were synthesised using the spatial ALD technique. A detailed investigation attributed the high resistivity to the short precursor exposure and purge durations of the spatial ALD method. This result is of great significance for CIGS thin-film solar cells, where a highly resistive undoped ZnO layer contributes to improved solar cell efficiencies.

IV.   The fabrication of Ga-doped ZnO films using spatial ALD was demonstrated for the first time and a detailed analysis was conducted to characterise the film properties. The GZO films displayed reasonably low resistivity and good optical transparency, indicating a potential for application as a TCO in heterojunction silicon wafer and thin-film solar cells.

V.   The developed GZO films were tested as the front and rear TCOs in monofacial heterojunction silicon wafer solar cells and important limitations were observed. It was shown that retaining ITO as the front TCO layer but replacing it at the rear by GZO resulted in very good solar cell performance and could contribute to a significant reduction in material costs in mass production.

The author's publications resulting from this PhD research are listed at the end of the thesis.

9.3   Proposed future research

In this section, some interesting possibilities for future research topics motivated by this thesis are briefly discussed.

9.3.1 Spatial ALD Al_2O_3 for tunnel oxide passivation

A potentially interesting research topic is the exploration of thin films fabricated by spatial ALD for application in 'passivated contacts'. Applying the ideas of surface passivation, an ultra-thin Al_2O_3 film can be inserted between c-Si and a metal contact to reduce recombination at the metal/silicon interface. An example of a passivated-contact solar cell is the TOPCon cell that has recently demonstrated an efficiency of 25.1 % [77]. In this case, a thin SiO_2 at the interface between Si and a carrier selective doped layer is the key to achieving such high efficiency [237]. The precise thickness control offered by ALD could play a vital role in the investigation of such contact passivating materials. The implementation of an ultra-thin (0.24 nm) Al_2O_3 film fabricated by ALD between an n^+ emitter and the Al front grid of an Al-LBSF solar cell recently demonstrated a conversion efficiency of 21.7 % [75]. Further research could investigate the application of the Al_2O_3 films developed in this thesis in passivated contacts in novel solar cell concepts.

9.3.2 Spatial ALD thin films for carrier selective contacts

The main difference between a passivating contact and a carrier-selective contact is that the latter needs to be a conductive material. A carrier selective contact structure typically includes a thin passivating oxide layer that permits tunneling of the selected carriers (i.e. a passivated contact). Metal oxides of interest as carrier-selective contacts include MoO_x, WO_x, NiO_x and TiO_2, for which ALD processes already exist [79, 238]. Potential research could focus on the development of such metal oxides as electron- and hole-selective contacts in high-efficiency solar cell concepts.

9.3.3 Alternate dopants for ZnO-based TCOs

The GZO films developed in this thesis demonstrated limitations when used as the front TCO in heterojunction silicon wafer solar cells. Using the results of this study as

a basis, alternate dopants could be investigated for the fabrication of doped ZnO films by ALD with improved characteristics, to replace ITO films at the front and rear of heterojunction silicon wafer solar cells. Possible examples are ZnO:Al and ZnO:B [95, 195]. Trying different dopants could also help to tune the work function of the doped ZnO TCO, thereby giving improved contacts to the p^+ and n^+ a-Si:H layers of HET solar cells. Interestingly, reports have demonstrated that it is also possible to dope ZnO with H, achieving a resistivity of 0.7×10^{-3} Ωcm [239].

APPENDIX

A. General material characterisation techniques used in Chapters 3-5

A brief overview of various characterisation techniques used in this thesis is given in this section. Since these techniques are not unique to the field of photovoltaics or optoelectronics (unlike the techniques used in Chapter 2) and were all used under standard conditions, the mechanism of each technique is not described in detail. More information regarding each characterisation technique may be found in the corresponding references. The main techniques used are:

(i)   *Spectroscopic ellipsometry (SE)*

SE is a common optical characterisation technique used for investigating the dielectric properties of thin films such as the film thickness, complex dielectric functions, refractive index and absorption coefficient. SE measures the change of polarisation of a light beam incident on the sample surface upon reflection or transmission. This polarization change is quantified by the amplitude ratio, Ψ, and the phase difference, Δ. These measured parameters are then converted into the sample's optical constants using established models. The modelled data can then be used to characterise composition, surface roughness, layer thickness, doping concentration, electrical conductivity and other properties. In this chapter, SE is primarily used to measure film thickness, refractive index (n) and absorption coefficient (k). A detailed description of the SE technique and its applications can e.g. be found in Refs. [240, 241].

(ii).   *Scanning electron microscopy (SEM)*

This is an imaging technique that uses a focused electron beam to scan a sample surface and analyses the generated backscattered electrons, secondary electrons, characteristic

X-rays and photons. The signals result from the interactions of the incident electron beam with atoms close to the sample surface. Due to the possibility of generating an extremely narrow electron beam, SEM micrographs have a large depth of field yielding a characteristic three-dimensional appearance useful for understanding the surface structure of a sample. Further information about SEM can e.g. be found in Refs. [242-244].

(iii). *Four-point probe (4PP)*

4PP is a simple apparatus for measuring the electrical properties of conductive samples. The 4PP consist of four, thin collinearly placed electric probes which are made to contact the sample being tested. The sheet resistance of a sample is determined by passing a current through the two outer probes and measuring the voltage through the inner probes. The separation of the current and voltage electrodes eliminates the influence of the contact resistance providing more accurate measurements as compared to a two-probe system. If the thickness of the conductive layer in the sample is known (e.g. the thickness of a conductive film), then the resistivity of the material can be determined. In this chapter, the resistivity of the *i*-ZnO films are determined using 4PP. Further details can e.g. be found in Ref. [245].

(iv). *X-ray photoelectron spectroscopy (XPS)*

XPS is a quantitative technique that measures the elemental composition of a sample surface in the parts per thousand. It is sensitive to the chemical state of elements in the sample and can determine electronic states. An XPS spectrum is obtained when a focused beam of X-rays is incident on the sample and the binding energy of photo-emitted electrons from the sample surface is determined. Unique peaks in intensity at certain binding energies correspond uniquely to known electronic states and can be used to calculate the atomic concentration of elements in the material. A detailed explanation is e.g. provided in Refs. [246, 247].

(v)   *X-ray diffraction (XRD)*

Another fairly standard thin film characterisation technique, XRD is primarily used to identify the crystallographic phases in a material. It is used to determine crystallographic orientation, homogeneity, atomic spacing in a crystal lattice and can also identify average bulk composition. The principle relies on the three-dimensional diffraction grating of X-rays by the planes in a crystal lattice. The technique uses simple tools: an X-ray tube, a sample holder, and an X-ray detector. Further information is e.g. provided in Refs. [248, 249].

B. General material characterisation techniques used in Chapters 6-8

(i) Spectral response (SR) and external quantum efficiency (EQE)

The spectral response (SR) of a solar cell is the ratio of current generated by the cell to the power of the incident illumination, measured over a range of wavelengths (typically 300 nm to 1200 nm for c-Si cells) at short-circuit conditions. SR is normally expressed as the spectrally resolved external quantum efficiency (EQE) of a solar cell. EQE is the ratio of the number of electron-hole pairs separated by a solar cell to the number of incident photons. A cell's EQE is directly related to SR by Eq. (1). Based on the definition of SR and EQE, these terms are indicative of a cell's J_{sc}. J_{sc} is related to EQE by Eq. (2), where $\phi(\lambda)$ represents the photon flux of the AM1.5G spectra and the integral limits are for a c-Si solar cell. The photon flux at a specific wavelength is determined by dividing the spectral irradiance at the wavelength by the corresponding photon energy. The EQE can be corrected for the photons lost due to optical reflection by measuring the solar cell's spectrally resolved reflectance (R), to determine the internal quantum efficiency (IQE) as per Eq. (3). EQE, IQE and R curves can be used to analyze the sources of J_{sc} losses in a solar cell [221].

$$SR = \frac{q\lambda}{hc} EQE \tag{1}$$

$$J_{sc} = q \int_{300nm}^{1200nm} EQE\,(\lambda)\,\phi(\lambda)d\lambda \tag{2}$$

$$IQE = \frac{EQE}{1-R} \tag{3}$$

(ii) Photoluminescence (PL) and electroluminescence (EL) imaging

Photoluminescence (PL) or electroluminescence (EL) refer to photon emission by a semiconductor when excited by incident photons or an external bias, respectively. In both cases the emitted photons are a result of charge carrier excitation and subsequent radiative recombination. The luminescence signal is collected by a Si charge coupled device (CCD) camera that produces a luminesce image. PL and EL are widely used for Si wafer solar cell characterisation, with applications including spatially resolved mapping of diffusion length, Si wafer defects, minority carrier lifetime, R_s, diode-model parameters, electrical cell parameters etc [250]. PL and EL were done at SERIS using a luminescence imaging tool from BT Imaging. In this thesis, PL and EL were used for R_s mapping for solar cells which is useful for finished cell loss analysis. R_s maps were derived from biased PL images (i.e., luminescence images taken under conditions in which the cell was illuminated and maintained at a terminal voltage) using the method of Kampwerth et alia [217].

LIST OF PUBLICATIONS

Journal papers:

[1]   **N. Nandakumar**, B. Hoex, B. Dielissen, D. Garcia-Alonso, Z. Liu, R. Gortzen, W. M. M. Kessels, T. Mueller, and A.G. Aberle, "Atmospheric spatial atomic layer deposition of ZnO:Ga thin films for application in photovoltaics," *ACS Applied Materials and Interfaces* (under review).

[2]   **N. Nandakumar**, B. Dielissen, D. Garcia-Alonso, Z. Liu, R. Gortzen, W. M. M. Kessels, A. G. Aberle, and B. Hoex, " Resistive intrinsic ZnO films deposited by ultrafast spatial ALD for PV applications," *IEEE Journal of Photovoltaics,* vol. 5, no. 5, pp. 1462-1469, 2015.

[3]   B. Hoex, M. Bosman, **N. Nandakumar**, and W. M. M. Kessels, "Silicon surface passivation by aluminium oxide studied with electron energy loss spectroscopy," *Physica Status Solidi – Rapid Research Letters (RRL),* vol. 7, no. 11, pp. 937-941, 2013.

[4]   V. Panwar, P. K. Singh, **N. Nandakumar**, B. Hoex, *et al.*, "Silicon surface passivation with amorphous aluminium oxide films using plasma ALD process: Importance of chemical passivation," *RSC Advances* (submitted).

[5]   **N. Nandakumar**, B. Hoex, B. Dielissen, D. Garcia-Alonso, Z. Liu, R. Gortzen, W. M. M. Kessels, T. Mueller, and A.G. Aberle, "Electrical properties of Ga-doped ZnO thin films deposited by fast spatial atomic layer deposition," (in preparation)

[6]   Z. Hameiri, N. Borojevic, L. Mai, **N. Nandakumar,** K. Kim and S. Winderbaum, "Thermally stable and low absorption industrial silicon nitride films with very low surface recombination," (in preparation).

International conference papers:

[1]   Z. Hameiri, N. Borojevic, L. Mai, **N. Nandakumar**, K. Kim, and S. Winderbaum, "Should the refractive index at 633 nm be used to characterise silicon nitride films?", *Proceedings of the 43rd IEEE Photovoltaics Specialist Conference, Oregon, USA* (2016).

[2]   **N. Nandakumar,** B. Hoex, B. Dielissen, D. Garcia-Alonso, Z. Liu, W. M. M. Kessels, R. Gortzen, F. Lin, A. G. Aberle, and T. Mueller, "Conductive gallium doped ZnO films deposited by ultrafast spatial atomic layer deposition for photovoltaic applications," *25th Asian PVSEC, Busan, South Korea*, 2015 (CSi-P-49)

[3]   **N. Nandakumar,** B. Dielissen, D. Garcia-Alonso, Z. Liu, W. M. M. Kessels, R. Gortzen, A. G. Aberle, and B. Hoex, "Spatial atomic layer deposition of intrinsic zinc oxide films for application in the photovoltaic industry," *Technical digest of the 6th World Conference on Photovoltaic Energy Conversion, Japan*, pp. 577-578, 2014 (4TuPo.7.17).

[4]   V. Shanmugam, J. Wong, **N. Nandakumar**, J. Cunnusamy, M. Zahn, A. Zhou, R. Yang, X. Chen, A. G. Aberle, and T. Mueller, "Investigation of fine line screen printed and stencil printedAg metal contacts for silicon wafer solar cells," *Technical digest of the 6th World Conference on Photovoltaic Energy Conversion, Japan*, pp. 573-574, 2014 (4TuPo.7.15).

[5]   M. Wilson, Z. Hameiri, **N. Nandakumar**, S. Duttagupta, "Application of non-contact corona-kelvin metrology for characterization of PV dielectrics on textured surfaces," *Proceedings of the 40th IEEE Photovoltaic Specialists Conference, Colorado, USA,* pp. 0680-0685, 2014, 2014.

[6]   **N. Nandakumar,** F. Lin, B. Dielissen, F. Souren, X. Gay, R. Gortzen, S. Duttagupta, A. G. Aberle, and B. Hoex, "Silicon surface passivation by Al_2O_3 films grown by spatial atomic layer deposition using low-cost precursors," *Proceedings of the 28th European Photovoltaic Solar Energy Conference, Paris, France*, 2013 (2BV-1-19).

[7]   B. Hoex, M. Bosman, **N. Nandakumar**, and W. M. M. Kessels, "C-Si surface passivation by aluminium oxide studied with electron energy loss spectroscopy," *Proceedings of the 39th IEEE Photovoltaic Specialists Conference, Florida, USA*, pp. 3333-3336, 2013.

[8]   F. Lin, **N. Nandakumar,** B. Dielissen, R. Gortzen, and B. Hoex, "Excellent surface passivation of silicon at low cost: Atomic layer deposited aluminium oxide from solar grade TMA," *Proceedings of the 39th IEEE Photovoltaic Specialists Conference, Florida, USA*, pp.1268-1271, 2013.

Oral presentations:

[1]   **N. Nandakumar,** Z. Liu, and A. G. Aberle, "Resistive intrinsic zinc oxide films deposited by ultrafast spatial ALD for photovoltaic applications", *PV Asia Scientific Conference, Asian Clean Energy Summit,* 2015.

[2]   **N. Nandakumar,** B. Hoex, B. Dielissen, D. Garcia-Alonso, Z. Liu, R. Gortzen, W. M. M. Kessels, A.G. Aberle and T. Mueller, "Progress with industrial-scale spatial atomic layer deposition Ga-doped ZnO films for application in photovoltaics," 26th *Asian PVSEC,* 2016.

[3]   **N. Nandakumar,** S. Duttagupta, F. Lin and A.G. Aberle, "Very low surface recombination velocities on low-resistivity *n*-type crystalline silicon using spatial atomic layer deposited Al_2O_3 films," 26th *Asian PVSEC,* 2016.

REFERENCES

[1] "Vital signs of the planet: global temperature," *National Oceanic and Atmospheric Administration (NOAA),* http://climate.nasa.gov/vital-signs/global-temperature/, Accessed on: 15th May 2016.

[2] R. A. Kerr, "Suns role in warming is discounted," *Science,* vol. 268, no. 5207, 1995.

[3] *NASA's Goddard Institute for Space Studies (NASA/GISS),* http://data.giss.nasa.gov/gistemp/graphs_v3/, Accessed on: 15th May 2016.

[4] "Vital signs of the planet: carbon dioxide," *National Oceanic and Atmospheric Administration (NOAA),* http://climate.nasa.gov/vital-signs/carbon-dioxide/, Accessed on: 15th May 2016.

[5] "Vital signs of the planer: sea level," *NASA Goddard Space Flight Center,* http://climate.nasa.gov/vital-signs/sea-level/, Accessed on: 15th May 2016.

[6] R. K. Pachauri, M. Allen, V. Barros, J. Broome, W. Cramer, R. Christ, J. Church, L. Clarke, Q. Dahe, and P. Dasgupta, "Climate Change 2014: Synthesis Report. Contribution of Working Groups I, II and III to the Fifth Assessment Report of the Intergovernmental Panel on Climate Change," 2014.

[7] "New Energy Outlook 2016," *Bloomberg New Energy Finance*, 2016.

[8] R. F. Service, "Is it time to shoot for the sun?," *Science (Washington, D. C.),* vol. 309, no. 5734, pp. 548-551, 2005.

[9] "Five seismic shifts to shake global electricity over the next 25 years," *Bloomberg New Energy Finance*, 2015.

[10] S. Bowden, and C. Honsberg, "Pvcdrom," *National Science Foundation, UNSW, Sydney, Canberra, Australia,* http://pveducation*. org/pvcdrom*, 2011.

[11] "Grid parity boost for solar leasing in Singapore," *ABC Carbon,* http://abccarbon.com/grid-parity-boost-for-solar-leasing-in-singapore/, Accessed on: 16th May 2015.

[12] M. Bieri, S. Tay, and T. Reindl, "Solar Economics Handbook of Singapore, March 2016 Update," *National Solar Repository of Singapore*, 2016.

[13] S. P. Services, "Historic Electricity Tariffs, April 2016," www.singaporepower.com.sg, Accessed on 15th May 2016.

[14] " International Technology Roadmap for Photovoltaic (ITRPV) 2015 Results," *Seventh Edition, March 2016.*

[15] R. M. Swanson, "A vision for crystalline silicon photovoltaics," *Progress in Photovoltaics: Research and Applications,* vol. 14, no. 5, pp. 443-453, 2006.

[16] E. S. Rubin, I. M. Azevedo, P. Jaramillo, and S. Yeh, "A review of learning rates for electricity supply technologies," *Energy Policy,* vol. 86, pp. 198-218, 2015.

[17] A. G. Aberle, "Surface passivation of crystalline silicon solar cells: a review," *Progress in Photovoltaics: Research and Applications,* vol. 8, no. 5, pp. 473-487, 2000.

[18] J. Schmidt, A. Merkle, B. Hoex, M. C. M. v. d. Sanden, W. M. M. Kessels, and R. Brendel, "Atomic-layer-deposited aluminum oxide for the surface passivation of high-efficiency silicon solar cells," *33rd IEEE Photovoltaics Specialists Conference*, 2008.

[19] D. E. Carlson, and C. R. Wronski, "Amorphous silicon solar cell," *Applied Physics Letters,* vol. 28, no. 11, pp. 671-673, 1976.

[20] K. Masuko, M. Shigematsu, T. Hashiguchi, D. Fujishima, M. Kai, N. Yoshimura, T. Yamaguchi, Y. Ichihashi, T. Mishima, and N. Matsubara, "Achievement of more than 25% conversion efficiency with crystalline silicon heterojunction solar cell," *Photovoltaics, IEEE Journal of,* vol. 4, no. 6, pp. 1433-1435, 2014.

[21]   U. Würfel, A. Cuevas, and P. Würfel, "Charge carrier separation in solar cells," *IEEE Journal of Photovoltaics,* vol. 5, no. 1, pp. 461-469, 2015.

[22]   W. Shockley, and H. J. Queisser, "Detailed balance limit of efficiency of p-n junction solar cells," *Journal of applied physics,* vol. 32, no. 3, pp. 510-519, 1961.

[23]   W. Shockley, "The Theory of p-n Junctions in Semiconductors and p-n Junction Transistors," *Bell System Technical Journal,* vol. 28, no. 3, pp. 435-489, 1949.

[24]   W. Shockley, and W. Read Jr, "Statistics of the recombinations of holes and electrons," *Physical review,* vol. 87, no. 5, pp. 835, 1952.

[25]   K. R. McIntosh, "Lumps, humps and bumps: Three detrimental effects in the current-voltage curve of silicon solar cells," *PhD Thesis, University of New South Wales*, 2001.

[26]   A. G. Aberle, *Crystalline silicon solar cells: advanced surface passivation and analysis*: Centre for Photovoltaic Engineering. University of New South Wales, 1999.

[27]   M. J. Kerr, and A. Cuevas, "General parameterization of Auger recombination in crystalline silicon," *Journal of Applied Physics,* vol. 91, no. 4, pp. 2473-2480, 2002.

[28]   P. Altermatt, F. Geelhaar, T. Trupke, X. Dai, A. Neisser, and E. Daub, "Injection dependence of spontaneous radiative recombination in crystalline silicon: Experimental verification and theoretical analysis," *Applied physics letters,* vol. 88, no. 26, pp. 261901, 2006.

[29]   R. N. Hall, "Electron-hole recombination in germanium," *Physical Review,* vol. 87, no. 2, pp. 387, 1952.

[30]   T. Trupke, M. A. Green, P. Würfel, P. Altermatt, A. Wang, J. Zhao, and R. Corkish, "Temperature dependence of the radiative recombination coefficient of intrinsic crystalline silicon," *Journal of Applied Physics,* vol. 94, no. 8, pp. 4930-4937, 2003.

[31]   A. Richter, S. W. Glunz, F. Werner, J. Schmidt, and A. Cuevas, "Improved quantitative description of Auger recombination in crystalline silicon," *Physical Review B,* vol. 86, no. 16, pp. 165202, 2012.

[32]   A. G. Aberle, S. Glunz, and W. Warta, "Impact of illumination level and oxide parameters on Shockley–Read–Hall recombination at the Si-SiO$_2$ interface," *Journal of Applied Physics,* vol. 71, no. 9, pp. 4422-4431, 1992.

[33]   A. G. Aberle, S. Glunz, and W. Warta, "Field effect passivation of high efficiency silicon solar cells," *Solar Energy Materials and Solar Cells,* vol. 29, pp. 175-182, 1993.

[34]   Y. Kim, C. Drowley, and C. Hu, "A new method of measuring diffusion length and surface recombination velocity," *14th Photovoltaic Specialists Conference,* vol. 1, pp. 596-600, 1980.

[35]   P. De Visschere, "Comment on GJ Rees "surface recombination velocity—a useful concept?"," *Solid-state electronics,* vol. 29, no. 11, pp. 1161-1165, 1986.

[36]   R. A. Sinton, and A. Cuevas, "Contactless determination of current–voltage characteristics and minority-carrier lifetimes in semiconductors from quasi-steady-state photoconductance data," *Applied Physics Letters,* vol. 69, no. 17, pp. 2510-2512, 1996.

[37]   A. Sproul, M. Green, and A. Stephens, "Accurate determination of minority carrier-and lattice scattering-mobility in silicon from photoconductance decay," *Journal of Applied Physics,* vol. 72, no. 9, pp. 4161-4171, 1992.

[38]   A. Cuevas, R. A. Sinton, and M. Stuckings, "Determination of recombination parameters in semiconductors from photoconductance measurements,"

References

Conference on Optoelectronic and Microelectronic Materials And Devices Proceedings, pp. 16-19, 1996.

[39]   J. Schmidt, and A. G. Aberle, "Accurate method for the determination of bulk minority-carrier lifetimes of mono-and multicrystalline silicon wafers," *Journal of Applied Physics,* vol. 81, no. 9, pp. 6186-6199, 1997.

[40]   B. Hoex, J. Schmidt, P. Pohl, M. C. M. van de Sanden, and W. M. M. Kessels, "Silicon surface passivation by atomic layer deposited Al_2O_3," *Journal of Applied Physics,* vol. 104, no. 4, pp. 044903, 2008.

[41]   S. Duttagupta, F. Lin, M. Wilson, M. B. Boreland, B. Hoex, and A. G. Aberle, "Extremely low surface recombination velocities on low-resistivity n-type and p-type crystalline silicon using dynamically deposited remote plasma silicon nitride films," *Progress in Photovoltaics: Research and Applications,* vol. 22, no. 6, pp. 641-647, 2014.

[42]   S. Dauwe, J. Schmidt, and R. Hezel, "Very low surface recombination velocities on p-and n-type silicon wafers passivated with hydrogenated amorphous silicon films," *Photovoltaic Specialists Conference, 2002. Conference Record of the Twenty-Ninth IEEE*, pp. 1246-1249, 2002.

[43]   H. Jin, K. Weber, N. Dang, and W. Jellett, "Defect generation at the Si–SiO_2 interface following corona charging," *Applied physics letters,* vol. 90, no. 26, pp. 262109, 2007.

[44]   E. Yablonovitch, D. Allara, C. Chang, T. Gmitter, and T. Bright, "Unusually low surface-recombination velocity on silicon and germanium surfaces," *Physical review letters,* vol. 57, no. 2, pp. 249, 1986.

[45]   S. Jain, and R. Muralidharan, "Effect of emitter recombinations on the open circuit voltage decay of a junction diode," *Solid-State Electronics,* vol. 24, no. 12, pp. 1147-1154, 1981.

[46]   D. Kane, and R. Swanson, "Measurement of the emitter saturation current by a contactless photoconductivity decay method," *18th IEEE photovoltaic specialists conference*, pp. 578-583, 1985.

[47]   A. Aberle, S. Wenham, and M. Green, "A new method for accurate measurements of the lumped series resistance of solar cells," *Conference Record of the Twenty Third IEEE Photovoltaic Specialists Conference* pp. 133-139, 1993.

[48]   K. R. McIntosh, and S. C. Baker-Finch, "Equivalent Circuit Calculator," www.pvlighthouse.com.au, Accessed on 20th June 2016, 2010.

[49]   T. Mueller, "Heterojunction solar cells (a-Si/c-Si): investigations on PECV deposited hydrogenated silicon alloys for use as high-quality surface passivation and emitter/BSF," *PhD Thesis, University of Hagen, Germany*, 2009.

[50]   W. D. Eades, and R. M. Swanson, "Calculation of surface generation and recombination velocities at the Si-SiO_2 interface," *Journal of applied Physics,* vol. 58, no. 11, pp. 4267-4276, 1985.

[51]   M. J. Kerr, and A. Cuevas, "Very low bulk and surface recombination in oxidized silicon wafers," *Semiconductor science and technology,* vol. 17, no. 1, pp. 35, 2001.

[52]   B. Hoex, "Functional thin films for high-efficiency solar cells," *PhD thesis, Technische Universiteit Eindhoven*, 2008.

[53]   J. Schmidt, M. Kerr, and A. Cuevas, "Surface passivation of silicon solar cells using plasma-enhanced chemical-vapour-deposited SiN films and thin thermal SiO_2/plasma SiN_x stacks," *Semiconductor Science and Technology,* vol. 16, no. 3, pp. 164, 2001.

[54]   S. Duttagupta, Z. Hameiri, T. Grosse, D. Landgraf, B. Hoex, and A. G. Aberle, "Dielectric Charge Tailoring in PECVD SiO/SiN Stacks and Application at

the Rear of Al Local Back Surface Field Si Wafer Solar Cells," *IEEE Journal of Photovoltaics,* vol. 5, no. 4, pp. 1014-1019, 2015.

[55]   S. Duttagupta, F. Lin, M. Wilson, M. B. Boreland, B. Hoex, and A. G. Aberle, "Extremely low surface recombination velocities on low-resistivity n-type and p-type crystalline silicon using dynamically deposited remote plasma silicon nitride films," 2012.

[56]   S. Duttagupta, "Advanced surface passivation of crystalline silicon for solar cell applications," *PhD thesis, National University of Singapore*, 2014.

[57]   M. A. Green, K. Emery, Y. Hishikawa, W. Warta, and E. D. Dunlop, "Solar cell efficiency tables (version 48)," *Progress in Photovoltaics: Research and Applications,* vol. 24, no. 7, pp. 905-913, 2016.

[58]   K. Masuko, M. Shigematsu, T. Hashiguchi, D. Fujishima, M. Kai, N. Yoshimura, T. Yamaguchi, Y. Ichihashi, T. Mishima, and N. Matsubara, "Achievement of more than 25% conversion efficiency with crystalline silicon heterojunction solar cell," *IEEE Journal of Photovoltaics,* vol. 4, no. 6, pp. 1433-1435, 2014.

[59]   S. Gatz, H. Plagwitz, P. P. Altermatt, B. Terheiden, and R. Brendel, "Thermally stable surface passivation by a-Si: H/SiN double layers for crystalline silicon solar cells," *Proceedings 23rd European Photovoltaic Solar Energy Conference and Exhibition*, pp. 1033-1035, 2008.

[60]   B. Liao, B. Hoex, A. G. Aberle, D. Chi, and C. S. Bhatia, "Excellent c-Si surface passivation by low-temperature atomic layer deposited titanium oxide," *Applied Physics Letters,* vol. 104, no. 25, pp. 253903, 2014.

[61]   B. Liao, B. Hoex, K. D. Shetty, P. K. Basu, and C. S. Bhatia, "Passivation of boron-doped industrial silicon emitters by thermal atomic layer deposited titanium oxide," *IEEE Journal of Photovoltaics,* vol. 5, no. 4, pp. 1062-1066, 2015.

[62]   S. Avasthi, W. E. McClain, G. Man, A. Kahn, J. Schwartz, and J. C. Sturm, "Hole-blocking titanium-oxide/silicon heterojunction and its application to photovoltaics," *Applied Physics Letters,* vol. 102, no. 20, pp. 203901, 2013.

[63]   X. Yang, P. Zheng, Q. Bi, and K. Weber, "Silicon heterojunction solar cells with electron selective TiO_x contact," *Solar Energy Materials and Solar Cells,* vol. 150, pp. 32-38, 2016.

[64]   X. Yang, Q. Bi, H. Ali, K. Davis, W. V. Schoenfeld, and K. Weber, "High-Performance TiO_2-Based Electron-Selective Contacts for Crystalline Silicon Solar Cells," *Advanced Materials*, 2016.

[65]   R. Hezel, "Low-Temperature Surface Passivation of Silicon for Solar Cells," *Journal of The Electrochemical Society,* vol. 136, no. 2, pp. 518, 1989.

[66]   B. Hoex, S. B. S. Heil, E. Langereis, M. C. M. van de Sanden, and W. M. M. Kessels, "Ultralow surface recombination of c-Si substrates passivated by plasma-assisted atomic layer deposited Al_2O_3," *Applied Physics Letters,* vol. 89, no. 4, pp. 042112, 2006.

[67]   G. Agostinelli, A. Delabie, P. Vitanov, Z. Alexieva, H. F. W. Dekkers, S. De Wolf, and G. Beaucarne, "Very low surface recombination velocities on p-type silicon wafers passivated with a dielectric with fixed negative charge," *Solar Energy Materials and Solar Cells,* vol. 90, no. 18-19, pp. 3438-3443, 2006.

[68]   B. Hoex, J. Schmidt, R. Bock, P. P. Altermatt, M. C. M. van de Sanden, and W. M. M. Kessels, "Excellent passivation of highly doped p-type Si surfaces by the negative-charge-dielectric Al_2O_3," *Applied Physics Letters,* vol. 91, no. 11, pp. 112107, 2007.

[69]   S. Duttagupta, F. Lin, K. D. Shetty, A. G. Aberle, and B. Hoex, "Excellent boron emitter passivation for high-efficiency Si wafer solar cells using

AlOx/SiNx dielectric stacks deposited in an industrial inline plasma reactor," *Progress in Photovoltaics: Research and Applications*, 2012.

[70]   J. Benick, B. Hoex, M. C. M. van de Sanden, W. M. M. Kessels, O. Schultz, and S. W. Glunz, "High efficiency *n*-type Si solar cells on Al$_2$O$_3$-passivated boron emitters," *Applied Physics Letters,* vol. 92, no. 25, pp. 253504, 2008.

[71]   S. Dauwe, L. Mittelstädt, A. Metz, and R. Hezel, "Experimental evidence of parasitic shunting in silicon nitride rear surface passivated solar cells," *Progress in Photovoltaics: Research and Applications,* vol. 10, no. 4, pp. 271-278, 2002.

[72]   J. Schmidt, F. Werner, B. Veith, D. Zielke, S. Steingrube, P. P. Altermatt, S. Gatz, T. Dullweber, and R. Brendel, "Advances in the Surface Passivation of Silicon Solar Cells," *Energy Procedia,* vol. 15, pp. 30-39, 2012.

[73]   J. Schmidt, F. Werner, B. Veith, D. Zielke, R. Bock, V. Tiba, P. Poodt, F. Roozeboom, A. Li, A. Cuevas, and R. Brendel, "Industrially Relevant Al$_2$O$_3$ Deposition Techniques for the Surface Passivation of Si Solar Cells," *25th European Photovoltaic Solar Energy Conference, Valencia, Spain*, pp. 1130-1113, 2009.

[74]   G. Dingemans, P. Engelhart, R. Seguin, M. Mandoc, M. van de Sanden, and W. Kessels, "Comparison between aluminum oxide surface passivation films deposited with thermal ALD, plasma ALD and PECVD," *Photovoltaic Specialists Conference (PVSC), 2010 35th IEEE*, pp. 003118-003121, 2010.

[75]   D. Zielke, J. H. Petermann, F. Werner, B. Veith, R. Brendel, and J. Schmidt, "Contact passivation in silicon solar cells using atomic-layer-deposited aluminum oxide layers," *physica status solidi (RRL) - Rapid Research Letters,* vol. 5, no. 8, pp. 298-300, 2011.

[76]   C. Battaglia, A. Cuevas, and S. De Wolf, "High-efficiency crystalline silicon solar cells: status and perspectives," *Energy & Environmental Science,* vol. 9, no. 5, pp. 1552-1576, 2016.

[77]   S. Glunz, F. Feldmann, A. Richter, M. Bivour, C. Reichel, H. Steinkemper, J. Benick, and M. Hermle, "The irresistible charm of a simple current flow pattern—25% with a solar cell featuring a full-area back contact," *Proceedings of the 31st European Photovoltaic Solar Energy Conference and Exhibition*, pp. 259-263, 2015.

[78]   A. Cuevas, T. Allen, J. Bullock, Y. Wan, and X. Zhang, "Skin care for healthy silicon solar cells," *42nd IEEE Photovoltaic Specialist Conference (PVSC)*, pp. 1-6, 2015.

[79]   B. Macco, B. Van de Loo, and W. M. M. Kessels, "Atomic Layer Deposition for High Efficiency Crystalline Silicon Solar Cells," *Atomic Layer Deposition in Energy Conversion Applications*, J. Bachmann, ed.: Wiley, 2016.

[80]   M. Grundmann, A. Rahm, and H. von Wenckstern, "Transparent Conductive Oxides," *Phys. Status Solidi A,* vol. 212, no. 7, pp. 1408, 2015.

[81]   D. S. Ginley, and C. Bright, "Transparent conducting oxides," *Mrs Bulletin,* vol. 25, no. 08, pp. 15-18, 2000.

[82]   F. Ruske, "Deposition and properties of TCOs," *Physics and technology of amorphous-crystalline heterostructure silicon solar cells*, pp. 301-330: Springer, 2012.

[83]   E. Fortunato, D. Ginley, H. Hosono, and D. C. Paine, "Transparent Conducting Oxides for Photovoltaics," *MRS Bulletin,* vol. 32, no. 03, pp. 242-247, 2007.

[84]   H. Mei, "Investigation of transparent conductive electrodes for application in heterojunction silicon wafer solar cells," *Ph.D Thesis, National University of Singapore*, 2016.

[85]   K. Ellmer, A. Klein, and B. Rech, *Transparent Conductive Zinc Oxide: Basics and Applications in Thin Film Solar Cells*: Springer Series in Materials Science, 2007.

References

[86]   B. Nijboer, "On the theory of electronic semiconductors," *Proceedings of the Physical Society,* vol. 51, no. 4, pp. 575, 1939.

[87]   E. Bunting, "Phase equilibria in the system SiO_2–ZnO," *Journal of the American Ceramic Society,* vol. 13, no. 1, pp. 5-10, 1930.

[88]   V. Coleman, and C. Jagadish, "Basic properties and applications of ZnO," *Zinc Oxide Bulk, Thin Films and Nanostructures: Processing, Properties, and Applications*, pp. 1-20, 2006.

[89]   H. Hartnagel, A. Dawar, A. Jain, and C. Jagadish, *Semiconducting transparent thin films*: Institute of Physics Bristol, 1995.

[90]   K. Ellmer, and R. Mientus, "Carrier transport in polycrystalline transparent conductive oxides: A comparative study of zinc oxide and indium oxide," *Thin solid films,* vol. 516, no. 14, pp. 4620-4627, 2008.

[91]   T. Minami, "New n-type transparent conducting oxides," *Mrs Bulletin,* vol. 25, no. 08, pp. 38-44, 2000.

[92]   B. Macco, Y. Wu, D. Vanhemel, and W. Kessels, "High mobility In_2O_3: H transparent conductive oxides prepared by atomic layer deposition and solid phase crystallization," *physica status solidi (RRL)-Rapid Research Letters,* vol. 8, no. 12, pp. 987-990, 2014.

[93]   A. Illiberi, F. Roozeboom, and P. Poodt, "Spatial Atomic Layer Deposition of Zinc Oxide Thin Films," *ACS Applied Materials & Interfaces,* vol. 4, no. 1, pp. 268-272, 2011.

[94]   A. Illiberi, R. Scherpenborg, Y. Wu, F. Roozeboom, and P. Poodt, "Spatial Atmospheric Atomic Layer Deposition of $Al_xZn_{1-x}O$," *ACS Applied Materials & Interfaces,* vol. 5, no. 24, pp. 13124-13128, 2013.

[95]   D. Garcia-Alonso, S. E. Potts, C. A. van Helvoirt, M. A. Verheijen, and W. M. Kessels, "Atomic layer deposition of B-doped ZnO using triisopropyl borate as the boron precursor and comparison with Al-doped ZnO," *Journal of Materials Chemistry C*, 2015.

[96]   Z. Szabó, Z. Baji, P. Basa, Z. Czigány, I. Bársony, H.-Y. Wang, and J. Volk, "Homogeneous Transparent Conductive ZnO: Ga by ALD for Large LED Wafers," *Applied Surface Science,* vol. 379, pp. 304-308, 2016.

[97]   A. Illiberi, R. Scherpenborg, F. Roozeboom, and P. Poodt, "Atmospheric Spatial Atomic Layer Deposition of In-Doped ZnO," *ECS Journal of Solid State Science and Technology,* vol. 3, no. 5, pp. P111-P114, 2014.

[98]   A. G. Aberle, and R. Hezel, "Progress in Low-temperature Surface Passivation of Silicon Solar Cells using Remote-plasma Silicon Nitride," *Progress in photovoltaics: research and applications,* vol. 5, no. 1, pp. 29-50, 1997.

[99]   R. K. Waits, "Planar magnetron sputtering," *Journal of Vacuum Science & Technology,* vol. 15, no. 2, pp. 179-187, 1978.

[100]   R. Pessoa, M. Fraga, L. Santos, N. Galvão, H. Maciel, and M. Massi, "Plasma-assisted techniques for growing hard nanostructured coatings," pp. 455-479, 2015.

[101]   H. Knoops, S. Potts, A. Bol, and W. Kessels, "Springer Handbook of Crystal Growth," Elsevier BV, 2010.

[102]   G. Agostinelli, P. Vitanov, Z. Alexieva, A. Harizanova, H. Dekkers, S. De Wolf, and G. Beaucarne, "Surface passivation of silicon by means of negative charge dielectrics," *Proceedings of the 19th European Photovoltaic Solar Energy Conference, Paris, France,* vol. 1, pp. 132-134, 2004.

[103]   ASM, http://www.asm.com/, Accessed on 15th July 2016.

[104]   Beneq, http://beneq.com/, Accessed on 15th July 2016.

[105]   P. Poodt, A. Lankhorst, F. Roozeboom, K. Spee, D. Maas, and A. Vermeer, "High-speed spatial atomic-layer deposition of aluminum oxide layers for solar cell passivation," *Adv Mater,* vol. 22, no. 32, pp. 3564-7, 2010.

[106] P. Poodt, D. C. Cameron, E. Dickey, S. M. George, V. Kuznetsov, G. N. Parsons, F. Roozeboom, G. Sundaram, and A. Vermeer, "Spatial Atomic Layer Deposition: A Route Towards Further Industrialization of Atomic Layer Deposition," *Journal of Vacuum Science & Technology A: Vacuum, Surfaces, and Films,* vol. 30, no. 1, pp. 010802, 2012.

[107] SoLayTec. http://www.solaytec.com/, Accessed on 15th July 2016.

[108] Levitech. http://www.levitech.nl/, Accessed on 15th July 2016.

[109] M. A. Green, "The passivated emitter and rear cell (PERC): from conception to mass production," *Solar Energy Materials and Solar Cells,* vol. 143, pp. 190-197, 2015.

[110] S. W. Glunz, J. Benick, D. Biro, M. Bivour, M. Hermle, D. Psych, M. Rauer, C. Reichel, A. Richter, M. Rudiger, C. Schmiga, D. Suwito, A. Wolf, and R. Preu, "n-type silicon - Enabling efficiencies >20% in industrial production," *Proceedings of the 35th IEEE Photovoltaic Specialists Conference, Honolulu, Hawai*, 2010.

[111] J. Schmidt, F. Werner, B. Veith, D. Zielke, R. Bock, R. Brendel, V. Tiba, P. Poodt, F. Roozeboom, and A. Li, "Surface passivation of silicon solar cells using industrially relevant Al_2O_3 deposition techniques," *Photovoltaics International,* vol. 10, pp. 52-57, 2010.

[112] A. Illiberi, P. Poodt, P. J. Bolt, and F. Roozeboom, "Recent Advances in Atmospheric Vapor-Phase Deposition of Transparent and Conductive Zinc Oxide," *Chemical Vapor Deposition,* vol. 20, no. 7-8-9, pp. 234-242, 2014.

[113] B. Macco, D. Deligiannis, S. Smit, R. van Swaaij, M. Zeman, and W. Kessels, "Influence of Transparent Conductive Oxides on Passivation of a-Si: H/C-Si Heterojunctions as Studied by Atomic Layer Deposited Al-Doped ZnO," *Semiconductor Science and Technology,* vol. 29, no. 12, pp. 122001, 2014.

[114] T. Tynell, and M. Karppinen, "Atomic Layer Deposition of ZnO: A Review," *Semiconductor Science and Technology,* vol. 29, no. 4, pp. 043001, 2014.

[115] G. Dingemans, and W. Kessels, "Status and prospects of Al2O3-based surface passivation schemes for silicon solar cells," *Journal of Vacuum Science & Technology A,* vol. 30, no. 4, pp. 040802, 2012.

[116] B. Hoex, M. Van de Sanden, J. Schmidt, R. Brendel, and W. Kessels, "Surface passivation of phosphorus-diffused n+-type emitters by plasma-assisted atomic-layer deposited Al2O3," *physica status solidi (RRL)-Rapid Research Letters,* vol. 6, no. 1, pp. 4-6, 2012.

[117] A. Richter, J. Benick, A. Kimmerle, M. Hermle, and S. W. Glunz, "Passivation of phosphorus diffused silicon surfaces with Al_2O_3: Influence of surface doping concentration and thermal activation treatments," *Journal of Applied Physics,* vol. 116, no. 24, pp. 243501, 2014.

[118] S. Duttagupta, F.-J. Ma, S. F. Lin, T. Mueller, A. G. Aberle, and B. Hoex, "Progress in Surface Passivation of Heavily Doped n-Type and p-Type Silicon by Plasma-Deposited AlO/SiN Dielectric Stacks," *IEEE Journal of Photovoltaics,* vol. 3, no. 4, pp. 1163-1169, 2013.

[119] G. Agostinelli, A. Delabie, P. Vitanov, Z. Alexieva, H. Dekkers, S. De Wolf, and G. Beaucarne, "Very low surface recombination velocities on p-type silicon wafers passivated with a dielectric with fixed negative charge," *Solar Energy Materials and Solar Cells,* vol. 90, no. 18, pp. 3438-3443, 2006.

[120] B. Hoex, J. J. H. Gielis, M. C. M. van de Sanden, and W. M. M. Kessels, "On the c-Si surface passivation mechanism by the negative-charge-dielectric Al_2O_3," *Journal of Applied Physics,* vol. 104, no. 11, pp. 113703, 2008.

[121] J. Schmidt, A. Merkle, R. Brendel, B. Hoex, M. C. M. v. de Sanden, and W. M. M. Kessels, "Surface passivation of high-efficiency silicon solar cells by atomic-layer-deposited Al_2O_3," *Progress in Photovoltaics: Research and Applications,* vol. 16, no. 6, pp. 461-466, 2008.

[122] J. Schmidt, A. Merkle, R. Brendel, B. Hoex, M. Van de Sanden, and W. Kessels, "Surface passivation of high-efficiency silicon solar cells by atomic-layer-deposited Al2O3," *Progress in photovoltaics: research and applications,* vol. 16, no. 6, pp. 461-466, 2008.

[123] P. Saint-Cast, J. Benick, D. Kania, LucasWeiss, M. Hofmann, J. Rentsch, R. Preu, and S. W. Glunz, "High-Efficiency c-Si Solar Cells PassivatedWith ALD and PECVD Aluminum Oxide," *IEEE Electron Device Letters,* vol. 31, no. 7, pp. 695-697, 2010.

[124] S. Glunz, J. Benick, D. Biro, M. Bivour, M. Hermle, D. Pysch, M. Rauer, C. Reichel, A. Richter, and M. Rüdiger, "*n*-type silicon-enabling efficiencies >20% in industrial production," *35th IEEE Photovoltaic Specialists Conference (PVSC)*, pp. 50-56, 2010.

[125] M. Hermle, F. Feldmann, J. Eisenlohr, J. Benick, H. Steinkemper, A. Richter, B. Lee, P. Stradins, A. Rohatgi, and S. W. Glunz, "Approaching efficiencies above 25% with both sides-contacted silicon solar cells," *42nd IEEE Photovoltaic Specialist Conference (PVSC)*, pp. 1-3, 2015.

[126] "Trina Solar Announces New Efficiency Record of 22.13% for Mono-crystalline Silicon Solar Cell," Trina Solar, http://ir.trinasolar.com/phoenix.zhtml?c=206405&p=irol-newsArticle&ID=2122938, Accessed on 5th August 2016, 2015.

[127] J. Schmidt, F. Werner, B. Veith, D. Zielke, R. Bock, V. Tiba, P. Poodt, F. Roozeboom, A. Li, and A. Cuevas, "Industrially relevant Al_2O_3 deposition techniques for the surface passivation of Si solar cells," *Proceedings of the 25th European Photovoltaic Solar Energy Conference, Valencia, Spain*, pp. 1130-1133, 2010.

[128] E. Granneman, P. Fischer, D. Pierreux, H. Terhorst, and P. Zagwijn, "Batch ALD: Characteristics, comparison with single wafer ALD, and examples," *Surface and Coatings Technology,* vol. 201, no. 22, pp. 8899-8907, 2007.

[129] B. Vermang, A. Rothschild, A. Racz, J. John, J. Poortmans, R. Mertens, P. Poodt, V. Tiba, and F. Roozeboom, "Spatially separated atomic layer deposition of Al2O3, a new option for high-throughput Si solar cell passivation," *Progress in Photovoltaics: Research and Applications,* vol. 19, no. 6, pp. 733-739, 2011.

[130] *SEMI C66-0308, Guidelines for Trimethylaluminium, 99.5% Quality*.

[131] G. Dingemans, and W. Kessels, "Recent progress in the development and understanding of silicon surface passivation by aluminum oxide for photovoltaics," *Proceedings of the 25th European Photovoltaic Solar Energy Conference, Valencia, Spain*, 2010.

[132] M. Wilson, J. D'Amico, A. Savtchouk, P. Edelman, A. Findlay, L. Jastrzebski, J. Lagowski, K. Kis-Szabo, F. Korsos, and A. Toth, "Multifunction metrology platform for photovoltaics," *37th IEEE Photovoltaic Specialists Conference (PVSC)*, pp. 001748-001753, 2011.

[133] M. Wilson, J. Lagowski, L. Jastrzebski, A. Savtchouk, and V. Faifer, "COCOS (corona oxide characterization of semiconductor) non-contact metrology for gate dielectrics." pp. 220-225.

[134] M. Wilson, J. Lagowski, A. Savtchouk, L. Jastrzebski, and J. D'Amico, "COCOS (corona oxide characterization of semiconductor) metrology: Physical principles and applications," *Gate Dielectric Integrity: Material, Process, and Tool Qualification*: ASTM International, 2000.

[135] M. Wilson, D. Marinskiy, A. Byelyayev, J. D'Amico, A. Findlay, L. Jastrzebski, and J. Lagowski, "The present status and recent advancements in corona-Kelvin non-contact electrical metrology of dielectrics for IC-manufacturing," *ECS Transactions,* vol. 3, no. 3, pp. 3-24, 2006.

[136] M. Wilson, J. Lagowski, L. Jastrzebski, A. Savtchouk, and V. Faifer, "COCOS (corona oxide characterization of semiconductor) non-contact metrology for gate dielectrics," *Characterization and metrology for ULSI technology,* vol. 550, no. 1, pp. 220-225, 2001.

[137] M. S. Wagner, S. L. McArthur, M. Shen, T. A. Horbett, and D. G. Castner, "Limits of detection for time of flight secondary ion mass spectrometry (ToF-SIMS) and X-ray photoelectron spectroscopy (XPS): detection of low amounts of adsorbed protein," *Journal of Biomaterials Science, Polymer Edition,* vol. 13, no. 4, pp. 407-428, 2002.

[138] D. W. Mogk, Montana State University, http://serc.carleton.edu/, Accessed on 27th July 2016.

[139] R. A. Sinton, and A. Cuevas, "Contactless determination of current-voltage characteristics and minority-carrier lifetimes in semiconductors from quasi-steady-state photoconductance data," *Applied Physics Letters,* vol. 69, no. 17, pp. 2510, OCT 21, 1996.

[140] F. Werner, B. Veith, D. Zielke, L. Kühnemund, C. Tegenkamp, M. Seibt, R. Brendel, and J. Schmidt, "Electronic and chemical properties of the c-Si/Al2O3 interface," *Journal of Applied Physics,* vol. 109, no. 11, pp. 113701, 2011.

[141] C. Jagadish, and S. J. Pearton, *Zinc oxide bulk, thin films and nanostructures: processing, properties, and applications*: Elsevier, 2011.

[142] H. Nanto, T. Minami, and S. Takata, "Zinc-oxide thin-film ammonia gas sensors with high sensitivity and excellent selectivity," *Journal of Applied Physics,* vol. 60, no. 2, pp. 482-484, 1986.

[143] I. Repins, M. A. Contreras, B. Egaas, C. DeHart, J. Scharf, C. L. Perkins, B. To, and R. Noufi, "19·9%-efficient ZnO/CdS/CuInGaSe$_2$ solar cell with 81·2% fill factor," *Progress in Photovoltaics: Research and applications,* vol. 16, no. 3, pp. 235-239, 2008.

[144] P. Jackson, D. Hariskos, E. Lotter, S. Paetel, R. Wuerz, R. Menner, W. Wischmann, and M. Powalla, "New world record efficiency for Cu (In, Ga) Se$_2$ thin-film solar cells beyond 20%," *Progress in Photovoltaics: Research and Applications,* vol. 19, no. 7, pp. 894-897, 2011.

[145] S. De Wolf, A. Descoeudres, Z. C. Holman, and C. Ballif, "High-efficiency silicon heterojunction solar cells: A review," *Green,* vol. 2, no. 1, pp. 7-24, 2012.

[146] S. Ishizuka, K. Sakurai, A. Yamada, K. Matsubara, P. Fons, K. Iwata, S. Nakamura, Y. Kimura, T. Baba, and H. Nakanishi, "Fabrication of wide-gap Cu (In$_{1-x}$Ga$_x$)Se$_2$ thin film solar cells: a study on the correlation of cell performance with highly resistive i-ZnO layer thickness," *Solar energy materials and solar cells,* vol. 87, no. 1, pp. 541-548, 2005.

[147] U. Rau, and M. Schmidt, "Electronic properties of ZnO/CdS/Cu (In, Ga) Se$_2$ solar cells—aspects of heterojunction formation," *Thin Solid Films,* vol. 387, no. 1, pp. 141-146, 2001.

[148] P. Grabitz, U. Rau, and J. Werner, "Modeling of spatially inhomogeneous solar cells by a multi-diode approach," *physica status solidi (a),* vol. 202, no. 15, pp. 2920-2927, 2005.

[149] P. Grabitz, U. Rau, and J. Werner, "Electronic inhomogeneities and the role of the intrinsic ZnO layer in Cu (In, Ga) Se$_2$ thin film solar cells," *20th European Photovoltaic Solar Energy Conference*, pp. 1771-1774, 2005.

[150] S. Niki, M. Contreras, I. Repins, M. Powalla, K. Kushiya, S. Ishizuka, and K. Matsubara, "CIGS absorbers and processes," *Progress in Photovoltaics: Research and Applications,* vol. 18, no. 6, pp. 453-466, 2010.

[151]   U. Rau, and H.-W. Schock, "Electronic properties of Cu(In,Ga)Se$_2$ heterojunction solar cells–recent achievements, current understanding, and future challenges," *Applied Physics A,* vol. 69, no. 2, pp. 131-147, 1999.

[152]   T. Nakada, and M. Mizutani, "18% efficiency Cd-free Cu (In, Ga) Se$_2$ thin-film solar cells fabricated using chemical bath deposition (CBD)-ZnS buffer layers," *Japanese Journal of Applied Physics,* vol. 41, no. 2B, pp. L165, 2002.

[153]   E. Guziewicz, I. Kowalik, M. Godlewski, K. Kopalko, V. Osinniy, A. Wójcik, S. Yatsunenko, E. Łusakowska, W. Paszkowicz, and M. Guziewicz, "Extremely low temperature growth of ZnO by atomic layer deposition," *Journal of Applied Physics,* vol. 103, no. 3, pp. 033515, 2008.

[154]   W. Kern, "Cleaning Solutions Based on Hydrogen Peroxide for Use in Silicon Semiconductor Technology," *RCA review,* vol. 31, pp. 187-206, 1970.

[155]   B. D. Johs, J. A. Woollam, C. M. Herzinger, J. N. Hilfiker, R. A. Synowicki, and C. L. Bungay, "Overview of Variable-Angle Spectroscopic Ellipsometry (VASE): II. Advanced Applications," *Society of Photo-Optical Instrumentation Engineers (SPIE) Conference Series,* vol. 1, pp. 29-58, 1999.

[156]   J. M. Siqueiros, R. Machorro, and L. E. Regalado, "Determination of the optical constants of MgF$_2$ and ZnS from spectrophotometric measurements and the classical oscillator method," *Applied Optics,* vol. 27, no. 12, pp. 2549-2553, 1988.

[157]   L. Ward, "Cadmium Sulphide (CdS)," *Handbook of Optical Constants of Solids*, E. D. Palik, ed., pp. 579-595, Boston: Academic Press, 1998.

[158]   P. D. Paulson, R. W. Birkmire, and W. N. Shafarman, "Optical characterization of CuIn$_{1-x}$Ga$_x$Se$_2$ alloy thin films by spectroscopic ellipsometry," *Journal of Applied Physics,* vol. 94, no. 2, pp. 879-888, 2003.

[159]   D. Garcia-Alonso, S. E. Potts, C. A. van Helvoirt, M. A. Verheijen, and W. M. Kessels, "Atomic layer Deposition of B-Doped ZnO using Triisopropyl Borate as the Boron Precursor and Comparison with Al-Doped ZnO," *Journal of Materials Chemistry C,* vol. 3, no. 13, pp. 3095-3107, 2015.

[160]   J. Ferguson, A. Weimer, and S. George, "Surface chemistry and infrared absorbance changes during ZnO atomic layer deposition on ZrO$_2$ and BaTiO$_3$ particles," *Journal of Vacuum Science & Technology A: Vacuum, Surfaces, and Films,* vol. 23, no. 1, pp. 118-125, 2005.

[161]   E. B. Yousfi, J. Fouache, and D. Lincot, "Study of atomic layer epitaxy of zinc oxide by in-situ quartz crystal microgravimetry," *Applied surface science,* vol. 153, no. 4, pp. 223-234, 2000.

[162]   S. Lim, S. Kwon, and H. Kim, "ZnO thin films prepared by atomic layer deposition and rf sputtering as an active layer for thin film transistor," *Thin Solid Films,* vol. 516, no. 7, pp. 1523-1528, 2008.

[163]   D. Kim, H. Kang, J.-M. Kim, and H. Kim, "The Properties of Plasma-Enhanced Atomic Layer Deposition (ALD) Zno Thin Films and Comparison with Thermal ALD," *Applied Surface Science,* vol. 257, no. 8, pp. 3776-3779, 2011.

[164]   S. F. Nelson, D. H. Levy, L. W. Tutt, and M. Burberry, "Cycle Time Effects on Growth and Transistor Characteristics of Spatial Atomic Layer Deposition of Zinc Oxide," *Journal of Vacuum Science & Technology A,* vol. 30, no. 1, pp. 01A154, 2012.

[165]   K. E. Elers, T. Blomberg, M. Peussa, B. Aitchison, S. Haukka, and S. Marcus, "Film uniformity in atomic layer deposition," *Chemical Vapor Deposition,* vol. 12, no. 1, pp. 13-24, 2006.

[166]   H. Fujiwara, and M. Kondo, "Effects of carrier concentration on the dielectric function of ZnO: Ga and In$_2$O$_3$: Sn studied by spectroscopic ellipsometry: analysis of free-carrier and band-edge absorption," *Physical Review B,* vol. 71, no. 7, pp. 075109, 2005.

[167] K. Postava, H. Sueki, M. Aoyama, T. Yamaguchi, C. Ino, Y. Igasaki, and M. Horie, "Spectroscopic ellipsometry of epitaxial ZnO layer on sapphire substrate," *Journal of Applied Physics,* vol. 87, no. 11, pp. 7820-7824, 2000.

[168] J. Muth, R. Kolbas, A. Sharma, S. Oktyabrsky, and J. Narayan, "Excitonic structure and absorption coefficient measurements of ZnO single crystal epitaxial films deposited by pulsed laser deposition," *Journal of Applied Physics,* vol. 85, no. 11, pp. 7884-7887, 1999.

[169] G. Jellison, and L. Boatner, "Optical functions of uniaxial ZnO determined by generalized ellipsometry," *Physical Review B,* vol. 58, no. 7, pp. 3586, 1998.

[170] A. Pimentel, E. Fortunato, A. Gonçalves, A. Marques, H. Aguas, L. Pereira, I. Ferreira, and R. Martins, "Polycrystalline intrinsic zinc oxide to be used in transparent electronic devices," *Thin Solid Films,* vol. 487, no. 1, pp. 212-215, 2005.

[171] W. Jeong, S. Kim, and G. Park, "Preparation and characteristic of ZnO thin film with high and low resistivity for an application of solar cell," *Thin Solid Films,* vol. 506, pp. 180-183, 2006.

[172] Y. Wu, P. Hermkens, B. Van de Loo, H. Knoops, S. Potts, M. Verheijen, F. Roozeboom, and W. Kessels, "Electrical Transport and Al Doping Efficiency In Nanoscale ZnO Films Prepared by Atomic Layer Deposition," *Journal of Applied Physics,* vol. 114, no. 2, pp. 024308, 2013.

[173] W. Maeng, and J.-S. Park, "Growth Characteristics and Film Properties of Gallium Doped Zinc Oxide Prepared by Atomic Layer Deposition," *Journal of Electroceramics,* vol. 31, no. 3-4, pp. 338-344, 2013.

[174] D. H. Levy, S. F. Nelson, and D. Freeman, "Oxide Electronics by Spatial Atomic Layer Deposition," *Journal of Display Technology,* vol. 5, no. 12, pp. 484-494, 2009.

[175] H. Chiang, J. Wager, R. Hoffman, J. Jeong, and D. A. Keszler, "High Mobility Transparent Thin-Film Transistors with Amorphous Zinc Tin Oxide Channel Layer," *Applied Physics Letters,* vol. 86, no. 1, pp. 013503, 2005.

[176] H. Kim, J. Horwitz, W. Kim, A. Mäkinen, Z. Kafafi, and D. Chrisey, "Doped ZnO Thin Films as Anode Materials for Organic Light-Emitting Diodes," *Thin Solid Films,* vol. 420, pp. 539-543, 2002.

[177] P. Görrn, M. Sander, J. Meyer, M. Kröger, E. Becker, H. H. Johannes, W. Kowalsky, and T. Riedl, "Towards See-Through Displays: Fully Transparent Thin-Film Transistors Driving Transparent Organic Light-Emitting Diodes," *Advanced Materials,* vol. 18, no. 6, pp. 738-741, 2006.

[178] B. Demaurex, S. De Wolf, A. Descoeudres, Z. C. Holman, and C. Ballif, "Damage at Hydrogenated Amorphous/Crystalline Silicon Interfaces by Indium Tin Oxide Overlayer Sputtering," *Applied Physics Letters,* vol. 101, no. 17, pp. 171604, 2012.

[179] A. Illiberi, M. Creatore, W. Kessels, and M. van de Sanden, "Hydrogenated Amorphous Silicon Based Surface Passivation of c-Si at High Deposition Temperature and Rate," *Physica Status Solidi (RRL)-Rapid Research Letters,* vol. 4, no. 8-9, pp. 206-208, 2010.

[180] J. Van Delft, D. Garcia-Alonso, and W. Kessels, "Atomic layer deposition for photovoltaics: applications and prospects for solar cell manufacturing," *Semiconductor Science and Technology,* vol. 27, no. 7, pp. 074002, 2012.

[181] P. Poodt, D. C. Cameron, E. Dickey, S. M. George, V. Kuznetsov, G. N. Parsons, F. Roozeboom, G. Sundaram, and A. Vermeer, "Spatial atomic layer deposition: A route towards further industrialization of atomic layer deposition," *Journal of Vacuum Science & Technology A,* vol. 30, no. 1, pp. 010802, 2012.

[182] B. Hoex, "Developments in Ultrafast ALD for PV," *Solar Cells,* vol. 9, pp. 10.

[183] Y. Li, G. Tompa, S. Liang, C. Gorla, Y. Lu, and J. Doyle, "Transparent and Conductive Ga-Doped ZnO Films Grown by Low Pressure Metal Organic Chemical Vapor Deposition," *Journal of Vacuum Science & Technology A,* vol. 15, no. 3, pp. 1063-1068, 1997.

[184] A. Wang, T. Chen, S. Lu, Z. Wu, Y. Li, H. Chen, and Y. Wang, "Effects of Doping and Annealing on Properties of ZnO Films Grown by Atomic Layer Deposition," *Nanoscale Research Letters,* vol. 10, no. 1, pp. 1-10, 2015.

[185] H.-W. Park, K.-B. Chung, J.-S. Park, S. Ji, K. Song, H. Lim, and M.-H. Jang, "Electronic Structure of Conducting Al-Doped ZnO Films as a Function of Al Doping Concentration," *Ceramics International,* vol. 41, no. 1, pp. 1641-1645, 2015.

[186] J.-M. Huang, C.-S. Ku, C.-M. Lin, S.-Y. Chen, and H.-Y. Lee, "In Situ Al-Doped ZnO Films by Atomic Layer Deposition with an Interrupted Flow," *Materials Chemistry and Physics,* vol. 165, pp. 245-252, 2015.

[187] R. L. Hoye, D. Muñoz-Rojas, S. F. Nelson, A. Illiberi, P. Poodt, F. Roozeboom, and J. L. MacManus-Driscoll, "Research Update: Atmospheric Pressure Spatial Atomic Layer Deposition of ZnO Thin Films: Reactors, Doping, and Devices," *APL Materials,* vol. 3, no. 4, pp. 040701, 2015.

[188] N. Nandakumar, B. Dielissen, D. Garcia-Alonso, R. G. Zhe Liu, W. M. M. Kessels, A. G. Aberle, and B. Hoex, "Resistive Intrinsic ZnO Films Deposited by Ultrafast Spatial ALD for PV Applications," *IEEE Journal of Photovoltaics,* vol. 5, no. 5, pp. 1462 - 1469, 2015.

[189] D. J. Lee, H. M. Kim, J. Y. Kwon, H. Choi, S. H. Kim, and K. B. Kim, "Structural and Electrical Properties of Atomic Layer Deposited Al-Doped ZnO Films," *Advanced Functional Materials,* vol. 21, no. 3, pp. 448-455, 2011.

[190] P. Banerjee, W.-J. Lee, K.-R. Bae, S. B. Lee, and G. W. Rubloff, "Structural, electrical, and optical properties of atomic layer deposition Al-doped ZnO films," *Journal of Applied Physics,* vol. 108, no. 4, pp. 043504, 2010.

[191] X. Jiang, F. Wong, M. Fung, and S. Lee, "Aluminum-doped zinc oxide films as transparent conductive electrode for organic light-emitting devices," *Applied Physics Letters,* vol. 83, no. 9, pp. 1875-1877, 2003.

[192] A. Illiberi, B. Cobb, A. Sharma, T. Grehl, H. Brongersma, F. Roozeboom, G. H. Gelinck, and P. Poodt, "Spatial atmospheric atomic layer deposition of $In_xGa_yZn_zO$ for thin films transistors," *ACS applied materials & interfaces*, 2015.

[193] J. Elam, and S. George, "Growth of ZnO/Al2O3 alloy films using atomic layer deposition techniques," *Chemistry of Materials,* vol. 15, no. 4, pp. 1020-1028, 2003.

[194] J.-S. Na, G. Scarel, and G. N. Parsons, "In situ analysis of dopant incorporation, activation, and film growth during thin film ZnO and ZnO: Al atomic layer deposition," *The Journal of Physical Chemistry C,* vol. 114, no. 1, pp. 383-388, 2009.

[195] Y. Wu, S. E. Potts, P. M. Hermkens, H. C. Knoops, F. Roozeboom, and W. M. Kessels, "Enhanced doping efficiency of Al-doped ZnO by atomic layer deposition using dimethylaluminum isopropoxide as an alternative aluminum precursor," *Chemistry of Materials,* vol. 25, no. 22, pp. 4619-4622, 2013.

[196] A. Ott, and R. Chang, "Atomic layer-controlled growth of transparent conducting ZnO on plastic substrates," *Materials Chemistry and Physics,* vol. 58, no. 2, pp. 132-138, 1999.

[197] P. R. Chalker, P. A. Marshall, S. Romani, J. W. Roberts, S. J. Irvine, D. A. Lamb, A. J. Clayton, and P. A. Williams, "Atomic Layer Deposition of Ga-Doped ZnO Transparent Conducting Oxide Substrates for CdTe-Based

Photovoltaics," *Journal of Vacuum Science & Technology A,* vol. 31, no. 1, pp. 01A120, 2013.

[198] V. Bhosle, A. Tiwari, and J. Narayan, "Electrical properties of transparent and conducting Ga doped ZnO," *Journal of Applied Physics,* vol. 100, no. 3, pp. 033713, 2006.

[199] T. Nam, C. W. Lee, H. J. Kim, and H. Kim, "Growth Characteristics and Properties of Ga-Doped ZnO (GZO) Thin Films Grown by Thermal and Plasma-Enhanced Atomic Layer Deposition," *Applied Surface Science,* vol. 295, pp. 260-265, 2014.

[200] D. J. Comstock, and J. W. Elam, "Atomic Layer Deposition of Ga_2O_3 Films Using Trimethylgallium and Ozone," *Chemistry of Materials,* vol. 24, no. 21, pp. 4011-4018, 2012.

[201] A. Illiberi, B. Cobb, A. Sharma, T. Grehl, H. Brongersma, F. Roozeboom, G. Gelinck, and P. Poodt, "Spatial Atmospheric Atomic Layer Deposition of $In_xGa_yZn_zO$ for Thin Film Transistors," *ACS Applied Materials & Interfaces,* vol. 7, no. 6, pp. 3671-3675, 2015.

[202] F. Werner, W. Stals, R. Görtzen, B. Veith, R. Brendel, and J. Schmidt, "High-rate atomic layer deposition of Al2O3 for the surface passivation of Si solar cells," *Energy Procedia,* vol. 8, pp. 301-306, 2011.

[203] S. Journal of Vacuum Science & Technology A: Vacuum, and FilmsMcIntosh, Keith R, and S. C. Baker-Finch, "OPAL 2: Rapid Optical Simulation of Silicon Solar Cells," *38th Photovoltaic Specialists Conference (PVSC)*, pp. 000265-000271, 2012.

[204] B. Pawar, S. Jadkar, and M. Takwale, "Deposition and characterization of transparent and conductive sprayed ZnO: B thin films," *Journal of Physics and Chemistry of Solids,* vol. 66, no. 10, pp. 1779-1782, 2005.

[205] M. Chen, X. Wang, Y. Yu, Z. Pei, X. Bai, C. Sun, R. Huang, and L. Wen, "X-ray photoelectron spectroscopy and auger electron spectroscopy studies of Al-doped ZnO films," *Applied Surface Science,* vol. 158, no. 1, pp. 134-140, 2000.

[206] C. Zhu, J. Li, Y. Yang, P. Lan, J. Huang, Y. Lu, R. Tan, N. Dai, and W. Song, "Tailoring the Resonance Wavelength and Loss Of Highly Ga Doped ZnO Plasmonic Materials by Varied Doping Content and Substrate Temperature," *Thin Solid Films,* vol. 605, pp. 95-101, 2015.

[207] H. Mahdhi, Z. B. Ayadi, J. Gauffier, and K. Djessas, "Influence of Substrate Temperature on the Properties of Nanostructured ZnO Thin Films Grown by RF Magnetron Sputtering," *Journal of Electronic Materials,* vol. 45, no. 1, pp. 557-565, 2016.

[208] T. Pisarkiewicz, K. Zakrzewska, and E. Leja, "Scattering of charge carriers in transparent and conducting thin oxide films with a non-parabolic conduction band," *Thin Solid Films,* vol. 174, pp. 217-223, 1989.

[209] N. Nandakumar, B. Hoex, B. Dielissen, D. Garcia-Alonso, Z. Liu, R. Gortzen, W. M. M. Kessels, A. G. Aberle, and T. Mueller, "Atmospheric spatial atomic layer deposition of Ga-doped ZnO films," *Submitted*, 2016.

[210] F. Wooten, *Optical properties of solids*: Academic press, 2013.

[211] R. W. Collins, and K. Vedam, "Optical properties of solids," *Encyclopedia of Applied Physics,* vol. 12, pp. 285, 1995.

[212] E. Burstein, "Anomalous optical absorption limit in InSb," *Physical Review,* vol. 93, no. 3, pp. 632, 1954.

[213] J. Burrill, D. Smith, K. Stirrup, and W. King, "The application of implantation to thin silicon cells," *Proceedings of the 6th IEEE Photovoltaic Specialists Conference, Cacoa Beach*, pp. 81-97, 1967.

[214]   M. A. Green, A. W. Blakers, J. Zhao, A. M. Milne, A. Wang, and X. Dai, "Characterization of 23-percent efficient silicon solar cells," *IEEE Transactions on Electron Devices,* vol. 37, no. 2, pp. 331-336, 1990.

[215]   A. W. Blakers, A. Wang, A. M. Milne, J. Zhao, and M. A. Green, "22.8% efficient silicon solar cell," *Applied Physics Letters,* vol. 55, no. 13, pp. 1363-1365, 1989.

[216]   A. Aberle, "Investigations on surface passivation of high-efficiency silicon solar cells," *PhD Thesis, University of Freiburg, Germany*, 1991.

[217]   H. Kampwerth, T. Trupke, J. Weber, and Y. Augarten, "Advanced luminescence based effective series resistance imaging of silicon solar cells," *Applied Physics Letters,* vol. 93, no. 20, pp. 202102, 2008.

[218]   J. Wong, S. Duttagupta, R. Stangl, B. Hoex, and A. G. Aberle, "A systematic loss analysis method for rear-passivated silicon solar cells," *IEEE Journal of Photovoltaics,* vol. 5, no. 2, pp. 619-626, 2015.

[219]   T. Trupke, R. Bardos, M. Abbott, and J. Cotter, "Suns-photoluminescence: Contactless determination of current-voltage characteristics of silicon wafers," *Applied Physics Letters,* vol. 87, no. 9, pp. 93503-93503, 2005.

[220]   R. Sinton, and A. Cuevas, "A quasi-steady-state open-circuit voltage method for solar cell characterization," *Proceedings of the 16th European Photovoltaic Solar Energy Conference,* vol. 1152, 2000.

[221]   A. G. Aberle, W. Zhang, and B. Hoex, "Advanced loss analysis method for silicon wafer solar cells," *Energy Procedia,* vol. 8, pp. 244-249, 2011.

[222]   A. Khanna, T. Mueller, R. A. Stangl, B. Hoex, P. K. Basu, and A. G. Aberle, "A fill factor loss analysis method for silicon wafer solar cells," *IEEE Journal of Photovoltaics,* vol. 3, no. 4, pp. 1170-1177, 2013.

[223]   A. Aberle, S. Wenham, and M. Green, "A new method for accurate measurements of the lumped series resistance of solar cells," *Conference Record of the 23rd IEEE Photovoltaic Specialists Conference*, pp. 133-139, 1993.

[224]   J. Wong, "Griddler: Intelligent computer aided design of complex solar cell metallization patterns," *IEEE 39th Photovoltaic Specialists Conference (PVSC)*, pp. 0933-0938, 2013.

[225]   S. Gatz, T. Dullweber, and R. Brendel, "Evaluation of series resistance losses in screen-printed solar cells with local rear contacts," *IEEE Journal of Photovoltaics,* vol. 1, no. 1, pp. 37-42, 2011.

[226]   D. Macdonald, and L. Geerligs, "Recombination activity of interstitial iron and other transition metal point defects in *p*-and *n*-type crystalline silicon," *Applied Physics Letters,* vol. 85, no. 18, pp. 4061-4063, 2004.

[227]   S. Glunz, S. Rein, J. Lee, and W. Warta, "Minority carrier lifetime degradation in boron-doped Czochralski silicon," *Journal of Applied Physics,* vol. 90, no. 5, pp. 2397-2404, 2001.

[228]   S. De Wolf, and M. Kondo, "Nature of doped a-Si: H/c-Si interface recombination," *Journal of Applied Physics,* vol. 105, no. PV-LAB-ARTICLE-2010-007, pp. 103707, 2009.

[229]   A. Richter, M. Hermle, and S. W. Glunz, "Reassessment of the limiting efficiency for crystalline silicon solar cells," *IEEE journal of photovoltaics,* vol. 3, no. 4, pp. 1184-1191, 2013.

[230]   S. Reuter, and R. Das, "Transparent Conductive Films for Flexible Electronics 2010-2020," *Cambridge UK*, 2010.

[231]   P. Carroy, D. Munoz, F. Ozanne, A. Valla, P. Mur, and G. Rodriguez, "Analysis of different front and back TCO on heterojunction solar cells," *31st EUPVSEC,* vol. 2CO.1.2, pp. 359-364, 2015.

[232]   K.-U. Ritzau, M. Bivour, S. Schröer, H. Steinkemper, P. Reinecke, F. Wagner, and M. Hermle, "TCO work function related transport losses at the a-Si:

H/TCO-contact in SHJ solar cells," *Solar Energy Materials and Solar Cells,* vol. 131, pp. 9-13, 2014.

[233] R. Rößler, C. Leendertz, L. Korte, N. Mingirulli, and B. Rech, "Impact of the transparent conductive oxide work function on injection-dependent a-Si: H/c-Si band bending and solar cell parameters," *Journal of Applied Physics,* vol. 113, no. 14, pp. 144513, 2013.

[234] M. Bivour, S. Schröer, and M. Hermle, "Numerical analysis of electrical TCO/a-Si: H (p) contact properties for silicon heterojunction solar cells," *Energy Procedia,* vol. 38, pp. 658-669, 2013.

[235] A. Klein, C. Körber, A. Wachau, F. Säuberlich, Y. Gassenbauer, S. P. Harvey, D. E. Proffit, and T. O. Mason, "Transparent conducting oxides for photovoltaics: manipulation of Fermi level, work function and energy band alignment," *Materials,* vol. 3, no. 11, pp. 4892-4914, 2010.

[236] Z. C. Holman, A. Descoeudres, L. Barraud, F. Z. Fernandez, J. P. Seif, S. De Wolf, and C. Ballif, "Current losses at the front of silicon heterojunction solar cells," *IEEE Journal of Photovoltaics,* vol. 2, no. 1, pp. 7-15, 2012.

[237] A. Moldovan, F. Feldmann, M. Zimmer, J. Rentsch, J. Benick, and M. Hermle, "Tunnel oxide passivated carrier-selective contacts based on ultra-thin SiO 2 layers," *Solar Energy Materials and Solar Cells,* vol. 142, pp. 123-127, 2015.

[238] J. Geissbühler, J. Werner, S. M. De Nicolas, L. Barraud, A. Hessler-Wyser, M. Despeisse, S. Nicolay, A. Tomasi, B. Niesen, and S. De Wolf, "22.5% efficient silicon heterojunction solar cell with molybdenum oxide hole collector," *Applied Physics Letters,* vol. 107, no. 8, pp. 081601, 2015.

[239] M. A. Thomas, J. C. Armstrong, and J. Cui, "New approach toward transparent and conductive ZnO by atomic layer deposition: Hydrogen plasma doping," *Journal of Vacuum Science & Technology A,* vol. 31, no. 1, pp. 01A130, 2013.

[240] H. Fujiwara, *Spectroscopic ellipsometry: principles and applications*: John Wiley & Sons, 2007.

[241] H. G. Tompkins, and W. A. McGahan, *Spectroscopic ellipsometry and reflectometry: a user's guide*: Wiley New York, 1999.

[242] C. Oatley, W. Nixon, and R. Pease, "Scanning electron microscopy," *Advances in Electronics and Electron Physics,* vol. 21, pp. 181-247, 1966.

[243] J. Goldstein, D. E. Newbury, P. Echlin, D. C. Joy, A. D. Romig Jr, C. E. Lyman, C. Fiori, and E. Lifshin, *Scanning electron microscopy and X-ray microanalysis: a text for biologists, materials scientists, and geologists*: Springer Science & Business Media, 2012.

[244] A. Cohen, and M. Hayat, "Principles and techniques of scanning electron microscopy," *Principles and Techniques of Scanning Electron Microscopy,* vol. 1, 1974.

[245] F. Smits, "Measurement of sheet resistivities with the four-point probe," *Bell System Technical Journal,* vol. 37, no. 3, pp. 711-718, 1958.

[246] J. F. Watts, "X-ray photoelectron spectroscopy," *Surface science techniques*, pp. 5-23, 1994.

[247] J. Chastain, R. C. King, and J. Moulder, *Handbook of X-ray photoelectron spectroscopy: a reference book of standard spectra for identification and interpretation of XPS data*: Physical Electronics Eden Prairie, MN, 1995.

[248] H. P. Klug, and L. E. Alexander, *X-ray diffraction procedures*: Wiley New York, 1954.

[249] B. E. Warren, *X-ray Diffraction*: Courier Corporation, 1969.

[250] T. Trupke, R. Bardos, M. Schubert, and W. Warta, "Photoluminescence imaging of silicon wafers," *Applied Physics Letters,* vol. 89, no. 4, pp. 044107, 2006.